Experimentation and Multiphysical Modeling of Bioanalytical Microdevices

Junyi Shang

Submitted in partial fulfillment of the
requirements for the degree of
Doctor of Philosophy
in the Graduate School of Arts and Sciences

COLUMBIA UNIVERSITY

2019

ABSTRACT

Experimentation and Multiphysical Modeling of Bioanalytical Microdevices

Junyi Shang

Bioanalytics involves quantitative measurements of complex biological samples that contain metabolites, DNA, RNA, and proteins. Efficient sample preparation for downstream analysis and sensitive detection of analytes can be achieved via bioanalytical microdevices. Fully realizing the potential of these devices requires tool characterization and bioprocess optimization, in addition to understanding device physics. Therefore, this thesis introduces multiphysical modeling and experimentation of microdevices, with applications to diabetes care and single-cell analysis.

To understand the physics of viscometric glucose microsensors, this thesis presents a model of the sensor, which couples the fluid flow with vibrating diaphragms. The model is used to predict the sensor response to glucose via theory of squeeze-film damping and vibrations of pre-stressed plate. A first-principle-based model resulting from the theory can be evaluated from the device's geometric and material properties, and quantitatively determines the device response to vibrational excitations at varying glucose concentrations.

Next, this thesis introduces a theoretical model for viscometric glucose microsensors that employ harmonic microcantilever oscillation in the sensing liquid. The presented model associates the unsteady Stokes equation with the motion of a bounded viscous liquid to understand the hydrodynamic impact on the cantilever. With a proper consideration of the viscosity and bounded geometry of liquid media, the model relaxes the thin-film assumption required for the diaphragm-based model, enabling an accurate representation of fluid-structure interactions based on

fundamental structural vibration and fluid flow equations.

Next, this thesis presents an experimental exploration of a hydrogel-based affinity microsensor for glucose monitoring via dielectric measurements. The microsensor incorporates a synthetic hydrogel that is attached to the device surface via in situ polymerization, which eliminates mechanical moving parts required in the viscometric glucose sensors. Changes in the dielectric properties of the hydrogel when binding reversibly with glucose molecules have been measured using a MEMS capacitive transducer to determine the glucose concentration. Experimental results demonstrate that in a glucose concentration range of 0–500 mg/dL and with a resolution of 0.35 mg/dL or better, the microsensor exhibits a repeatable and reversible response, and can potentially be useful for continuous glucose monitoring in diabetes care.

Additionally, this thesis presents a microfluidic preprocessing method that integrates single-cell picking, lysing, reverse transcription and digital polymerase chain reaction to enable the isolation, tracking and gene expression analysis at single-cell level for individual cells. The approach utilizes a photocleavable bead-based microfluidic device to synthesize and deliver stable complementary DNA for downstream gene expression analysis, thereby allowing chip-based integration of multiple reactions and facilitating the minimization of sample loss or contamination.

Finally, this thesis ends with concluding remarks and directions of future work towards continuous glucose monitoring and high-throughput single-cell genetic analysis.

Table of Contents

List of Figures

List of Abbreviations

AAPBA	N-3-acrylamidophenylboronic acid
AAPH	2,2’-Azobis (2-methylpropionamidine) dihydrochloride
AC	alternating current
AFM	atomic force microscope
ALE	arbitrary Lagrangian-Eulerian
CDC	Centers for Disease Control and Prevention
cDNA	complementary deoxyribonucleic acid
CDKN1A	cyclin-dependent kinase inhibitor 1A
CGM	continuous glucose monitoring
DM	diabetes mellitus
DNA	deoxyribonucleic acid
dPCR	digital polymerase chain reaction
FACS	fluorescence-activated cell sorting
GDF15	growth differentiation factor 15
HEAA	acryl N-Hydroxyethyl acrylamide
MACS	magnetic-activated cell sorting
MEMS	micro-electromechanical system
mRNA	messenger ribonucleic acid
NFκB	nuclear factor kappa-light-chain-enhancer of activated B cells

NMSE	normalized mean square error
PAA-ran-PAAPBA	acrylamideran-3-acrylamidophenylboronic acid
Parylene	poly(p-xylyene) polymers
PCR	polymerase chain reaction
PDMS	polydimethylsiloxane
PreGEM	preprocessing for gene-expression measurement
PTGS2	prostaglandin-endoperoxide synthase 2
qPCR	quantitative polymerase chain reaction
RNA	ribonucleic acid
RT	reverse transcription
RT-PCR	reverse transcription polymerase chain reaction
RT-qPCR	reverse transcription real-time polymerase chain reaction
TEGDA	tetraethyleneglycol diacrylate
xenoRNA	xeno ribonucleic acid

Acknowledgements

Completion of this dissertation has been an exciting and challenging journey. I am truly grateful to a lot of people who offered help and support throughout all these years, reminding me that I am never alone on this journey.

First, I would like to express my gratitude to my PhD advisor Professor Qiao Lin. Professor Lin provided me the opportunity to join his BioMEMS lab at Columbia University, introducing me to cross-disciplinary research projects and collaborations. Through my graduate research, his dedicated mentoring and patience have provided me tremendous support and kept me a positive outlook personally and professionally.

Besides, I would like to thank Prof. Sally A. Amundson, Dr. Brian Ponnaiya, Dr. David Welch, Dr. Manuela Buonanno, Prof. Qian Wang and Dr. Jing Yan for their great support, ingenious insight and advice on my dissertation research. Thanks to their knowledge and efforts, I have always been enlightened and inspired when carrying on cross-disciplinary research projects. I am also grateful for support and suggestions from Prof. Karen E. Kasza and Prof. Kristin Myers toward completion of this dissertation.

In addition, I want to thank my lab mates, fellow students and classmates for their advice, help and friendship. This includes a list of names that is long and might be incomplete: Jing Zhu, Bin Wang, Yuan Jia, Jaeyoung Yang, Bing Song, Hao Sun, Tim Olsen, Yibo Zhu, Cheng Wang, Zhuang Hao, Xuejun Wang, Yaofei Chen, Yijun Li, Chao Su, Dongyang Wang, Yuqian Zhang, Di Wang, Jeff Mayo, Guojun Chen, Ye Qian, Gan Song, Hang Xiao, Jonathan Kyle, Dakai Bian,

Shengxi Yuan, Changjian Zhang, Xiaoqiang Ji, Jianzhong Zhu, Te Li, Zhixing Zhang, Shifeng Yu, Ziran Wang, Xing Meng, Kechun Wen, Xue Bai, Mo Yu, Keye Su, Liangwei Li, Enlin Wang, Hao Huang and Yuan Liu.

Finally, I would like to say thank you to my parents Aiqun Shang and Rao Nie for their love, understanding, and support.

Dedicated to my parents and grandparents

Chapter 1. Introduction

1.1 Microfluidics and MEMS for Bioanalytics

Bioanalytics are analytical methods for determination and analysis of biological targets, such as proteins, DNA, RNA, and small molecules [1]. These methods have been applied to understand fundamental physicochemical mechanisms and processes associated with molecular and cellular biophysical phenomena [2]. Bioanalytical techniques and tools that implement such methods are widely used for bio-sample preparation and detection, such as chromatography [3], electrophoresis [4], mass spectrometry [5] and biosensing [6].

Micro-Electro-Mechanical Systems (MEMS) are miniaturized devices that integrate both mechanical and electrical components, such as actuators and sensors, which are manufactured by microfabrication. Over the past two decades, MEMS techniques have been extensively used to miniaturize bioanalytical devices. Such miniaturized devices decrease reagent consumption, enhance transport and mixing of samples under controlled flow conditions, offer improved efficiency and quality of reaction, and utilize the same platform for preparing and detecting samples. Derived from integrated circuit (IC) technology, MEMS involves manufacturing processes of photolithographing, etching, and deposition, to make desired configurations of features. When MEMS-based devices are combined with biological recognition elements, these devices can monitor and analyze biochemical reactions with miniaturized sample consumption and the capability to respond on short time scales, providing insights for fundamental physiochemical

mechanism. For example, MEMS technology has been integrated in microdevices for clinical diagnostics [7], therapeutics [8] and rehabilitation assessment [9]. MEMS techniques have also been used to fabricate microfluidic systems, which use low volumes of fluids to achieve multiplexing, automation and high-throughput screening, enabling less reagents consumption, rapid preparation combined with detection, enhancement of sensitivity and reduction in cross-contamination [10]. These merits of MEMS and microfluidic technologies allow the design and fabrication of efficient micro-platforms for analysis of biological molecules, which possesses great potential for genome, proteome and metabolome studies.

1.2 Applications of Bioanalytical Microdevices

Bioanalytical microdevices, i.e., MEMS and microfluidic-based miniaturized systems or devices suitable for bioanalysis, have been widely used in many applications, such as diabetes care and single-cell analysis.

Diabetes mellitus (DM) is a metabolic disease reflected as abnormal blood sugar levels that can cause many complications. There are three major types of diabetes mellitus: Type 1 Diabetes is resulted from the pancreas' failure to produce enough insulin; Type 2 Diabetes is caused by the resistance of cells responding to insulin; the third type is gestational diabetes occurs when pregnant women develop high blood sugar levels. According to CDC report, by 2015 (Figure 1-1), more than 100 million people in the U.S. have diabetes or prediabetes. Among all signs and symptoms of diabetes, low blood sugar level is common for both type 1 and type 2 Diabetes, which is acute

because it may lead to brain damage or death. Therefore, real-time glucose monitoring is in need to continuously track the blood sugar levels of diabetes patients and alarm abnormal low blood sugar levels in a timely manner.

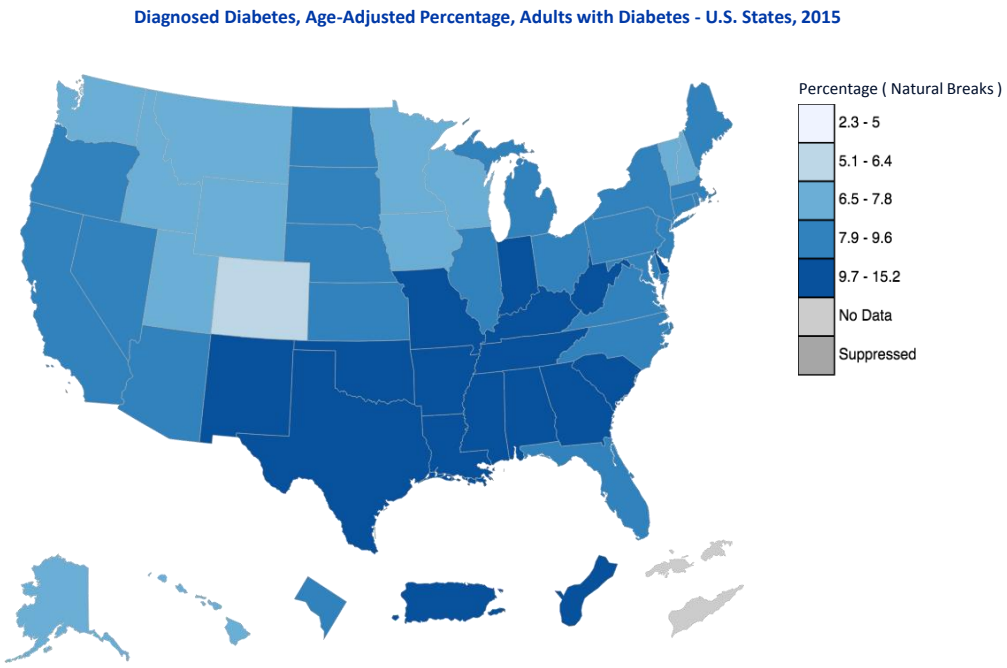

Figure 1–1: Age-averaged percentage of adults with diagnosed Diabetes within U.S. by 2015 [11].

As an important bioanalytical technique, continuous glucose monitoring (CGM) measures blood glucose levels throughout the day and night, which helps patients manage their diabetes in real time. The different mechanism of glucose detection can categorize various CGM devices, such as electrochemical, optical and affinity-based. Commercially available CGM devices rely on electrochemical detection of enzymatic reactions. Some of the devices have been approved by Food and Drug Administration (FDA), such as Dexcom G6 [12], Abbott FreeStyle Libre [13] and

Medtronic Guardian [14]. From the perspective of clinical use, the real-time CGM devices have proven to be meaningful in reducing the events of hypoglycemia [15]. Furthermore, the use of CGM devices improves the quality of life by being cost-effective in long-term projections and reducing the fear in hypoglycemia [16]. However, the CGM devices still need to be improved in terms of sensor lifetime, accuracy, size, user accessibility and software managements. Another important issue with the CGM is the requirement of frequent calibration, which is usually twice a day in most of the commercial devices. Reducing the frequency in calibration while maintaining the accuracy will be a research focus.

MEMS and microfluidic technologies offer miniaturization and rapid time responses, and are well suited to develop glucose monitoring devices. To date, MEMS has been used extensively in developing glucose microsensors based on electrochemical detection and microdialysis. For example, electrochemical MEMS glucose sensors [17][18][19] employ microelectrodes functionalized with glucose oxidase, i.e., an enzyme to catalyze the oxidation of glucose, while MEMS-based microdialysis serves as a minimally-invasive sampling tool, which has been widely used to collect glucose in interstitial fluids [20][21][22].

A MEMS affinity glucose sensor is based on reversible affinity interaction of glucose with specific receptor, which can potentially address large drift and insufficient accuracy of using electrochemical detection with irreversible and consumptive nature. MEMS affinity glucose sensors measure the glucose-induced changes in physical properties of sensing elements, such as fluorescence intensity, viscosity or volume [23][24][25]. For example, MEMS sensors have

adopted polymers as glucose receptors, detecting the change in viscosity or permittivity of the polymer solution as the polymer binds to glucose [26][27][28][29].

Single-cell analysis provides the approaches to detect, isolate, and analyze individual cells as well as rare cells such as circulating tumor cells and cancer stem cells [30][31]. The main focus on developing the single-cell tool is improvement of sensitivity and high throughput. The collection and isolation of single cells must be effective and efficient to ensure the single-cell samples of high quality. Besides, the cell state changes as well as cell survival rate within the tools have been considered for the effects upon downstream analysis. Emerging techniques have provided approaches to study the biological systems at single-cell resolution and reveal the complex response of an organism to various physiological stimuli.

Single-cell approaches include fluorescent-activated cell sorting (FACS), magnetic-activated cell sorting (MACS), laser capture microdissection, patch clamp, and optical tweezer [32]. Microfluidics can be combined with these cell manipulation techniques in networks of microchannels, providing solutions to isolation, manipulation and isolation of single cells. The miniaturization and large surface-to-volume ratio enable higher sensitivity levels for selecting cells as well as multiplexing capabilities for high-throughput processing. A variety of cellular biomarkers, such as physical properties and immunoassay, have been used for isolating and sorting single cells [33]. For example, cells in a microfluidic channel can be sorted based on physical properties (e.g., size, light absorption and refractive index) that affect their optical trapping force [34]. Besides, antibody-coated microposts have been used to separate target cells with surface

markers that bind with the antibody in a specific manner [35]. Additionally, inertial lift forces, pressure-field gradient, laminar microvortices, and pressure by aspiration have separated or focused cells using hydrodynamic methods with a high-throughput capability [36][37].

Single-cell manipulation enables analyses of single-cell gene expression. Gene expression analysis is a critical downstream application of cell manipulation. The gene expression regulation refers to the mechanisms that induce or repress the expression of a gene. These include physical and chemical changes to the genetic material, binding of proteins to specific DNA elements to regulate transcription, or mechanisms that modulate translation of mRNA. Gene expression analysis can be performed on one of the various levels at which gene expression is regulated, such as transcriptional, post-transcriptional, translational, and post-translational protein modification. While technologies such as quantitative real time polymerase chain reaction (PCR) assay, DNA microarray, flow cytometry-based detection and immunofluorescence have been invented to quantitatively probe the gene expression at the different levels, these technologies often require a variety amount of starting materials (DNA, RNA or protein) as well as complex procedures that is separated from cell isolation and genetic material purification. Microfluidic device is capable of combining cell preparation with environmental control for biochemical reaction, which paves a way for devices to analyze gene expression based on sorted single cells. For example, microfluidic PCR has integrated cell trapper, pneumatic valves and heaters that allows the automation of PCR thermal cycling on a microfluidic chip [38]. Microfluidic devices not only reduce sample consumption but also enhance the possibility of parallelization by miniaturization, which helps to

address the drawbacks of existing technologies for gene expression analysis. For example, the analysis of single cells via reverse-transcription PCR is capable of performing qPCR measurements of gene expression from hundreds of single cells per run [39]. Single-cell gene expression profiling, a method to assay the gene patterns in individual cells, is capable of alleviating the complexity of genetic variability caused by heterogeneity and has the potential to reveal intracellular molecular mechanisms and pathways.

1.3 Coupled Multiphysical Phenomena in Bioanalytical Microdevices

Bioanalytical microdevices involve multiple physics (e.g., fluids, structural mechanics, heat transfer, electromagnetics, and optics) and their interactions for actuating, sensing, transporting reagents and environmental control. For example, MEMS-based devices may require electrostatic or magnetic actuation of mechanical moving parts, which can induce elastic deformation of the device's structure. Microfluidic systems use fluid flow to transport biochemical reagents and target analytes for reaction, in which heat transfer may determine the reaction quality and efficiency [40, 41].

To investigate and understand underlying mechanisms of these events, various coupling models have been built and adopted in the parametric studies and simulations of bioanalytical microdevices, such as fluid-structure coupling and electric field-structure coupling.

Fluid-structure coupling describes the interaction between a movable or deformable structure with an internal or surrounding fluid flow. The fluid flow around the solid structure would have

an impact on the deformation or motion of the structure while the structure in turn will influence the fluid flow on the pressure field via dynamic boundaries. Inclusion of the coupling of fluid flow and structural motion is found to be challenging due to the difficulties of capturing the dynamic nature of fluid-structure coupling. Physical properties of the structure such as volume, shape, and deformability need to be taken into consideration. This also requires that the fluid-structure interface be tracked and the effect of the structure on the fluid be represented, which is being enabled by advances in computational treatments of fluid-structure coupling [42, 43]. In addition, harmonic response analyses, which determine the steady-state response of a dynamic system, are also available for solving dynamic problems of fluid-structure interaction, assuming applied loads on the components of the system vary harmonically with time.

Modeling of electric field-structure coupling is commonly applied to analyze static deformation of microstructures subjected to electrostatic loads, dynamic response and optimization of electrostatic loads on microstructures, and fluid damping effect in electrostatic-driven systems [44]. When an electric potential difference is applied between a suspended microstructure and the substrate of a device, the electric force will attract the structure toward the substrate while the elastic restoring force of the structure will act in an opposite direction. In statics, the elastic restoring force and the electrostatic force are kept in an equilibrium state. However, the deformation of the structure will alter the charge distribution on its surface, which will cause the redistribution of the electric field until the system achieves a new equilibrium state. In addition to addressing the coupling between the electric field and structure, the stability of the coupled system

needs to be taken into consideration. While the elastic force is proportional to the deformation of the structure, the electric force increases nonlinearly with the structural deformation. This will induce instability of the system after the electric force applied on the structure exceeds a critical value. Therefore, the nonlinearity of the structural deformation and electrostatic force as well as instability problems have raised the challenges for modeling the electric field-structure coupling.

1.4 Contributions and Significance of This Thesis

Focusing on glucose monitoring and single-cell analysis of individual cells, two of the most important applications of bioanalytics, this thesis has explored experimentation and multiphysical modeling of bioanalytical microdevices to address existing challenges for continuous glucose monitoring and single-cell analysis, demonstrating the utility and potential of the microdevices.

Diaphragm-based viscometric glucose sensors and microcantilever-based viscometric glucose sensors have been previously developed [27, 29, 45, 46]. However, there has been no fundamental study yet that provides understanding the complex fluid-structure interactions in these microdevices. Therefore, in this thesis, a fluid-structure-interaction model has been developed to efficient and accurate quantitative determination of dynamic characteristics of the diaphragm-based viscometric glucose sensor. This model considers both the dissipative effects in the fluid and the effect of confinement on the flow. The model also considers in-plane forces on constrained thin film structure and is therefore capable of predicting the dynamic behavior of vibrational microstructure in viscous bounded fluids.

We also develop a model of the microcantilever-based viscometric glucose sensor enabling the prediction of the dynamic behavior of the sensor, providing detailed insight into the sensor characteristics based on the geometric and material properties. This work differentiates from the diaphragm model by relaxing the thin-film assumption and applying the model of unsteady stokes flow to analyze a harmonic flow field. By considering the surface stress, this model can be generalized to cases where the microcantilever-based sensors are used for biochemical sensing via surface binding. Additionally, the dynamic response of the cantilever under thermal excitation was investigated, which allows the extension of the model to assess the effect of thermal noise at various excitation frequencies and flow conditions.

In addition to vibrational glucose sensors that measure the glucose-induced changes in viscosity via diaphragm or cantilever, we conduct exploratory study on a hydrogel-based glucose sensor. The glucose sensor measures glucose concentrations via the dielectric response of a synthetic hydrogel embedded in a capacitive transducer. The hydrogel is directly immobilized onto the surface of the transducer via in situ polymerization and will be stable over time, allowing the device to eliminate the use of a semipermeable membrane that are otherwise required to hold the glucose-sensitive material, and potentially offer improved tolerance to biofouling during implanted operation.

In the second part of this thesis, we investigate gene expression of single cells with a microfluidic-integrated preprocessing platform. Previous work and existing systems would not allow tracking the identity of an individual cell as well as not allow a timely handling of the cells

after irradiation. Therefore, to address these limitations, thereby enabling the study of microbeam-irradiated single cells and bystander effects, our approach has incorporated a single-cell capillary picker to introduce single cells into a microfluidic gene-expression preprocessing chip. The chip enables synthesizing and delivering stable cDNA for downstream gene expression analysis.

1.5 Organization of the Thesis

In this thesis, we focus on the development of key technologies for experimentation and multiphysical modeling of bioanalytical microdevices. Following this introduction, Chapter 2 of this thesis presents an accurate and efficient approach to simulations in confined geometry for the diaphragm-based viscometric glucose sensor. Chapter 3 presents a model of the microcantilever-based viscometric glucose sensor. The model uses unsteady stokes flow to analyze a harmonic flow field, which relaxes the thin-film assumption in the model of Chapter 2. As a complementary alternative to vibrational glucose sensor and an exploratory study on dielectric glucose detection, Chapter 4 presents a dielectric glucose sensor, which uses a synthetic hydrogel to recognize glucose molecules via affinity binding. In Chapter 5, we introduce another application in bioanalytics, which is single-cell analysis for individual cells. This chapter explores a microfluidic integrated approach for characterizing variability in gene expressions of single cells. This thesis will conclude with a summary and a discussion of future work in Chapter 6.

Chapter 2. Understanding Viscometric Glucose Sensing: Diaphragms Vibrating in Fluids

Viscometric glucose microsensors have been developed previously in our laboratory, which measure glucose-dependent viscosities of sensing fluids via the frequency response of vibrating diaphragms [45] or vibrating microcantilevers [27, 46]. While the viscometric microsensors have demonstrated the potential for continuous glucose monitoring, there is a pressing need of theoretical studies to understand the dynamics of the sensors involving coupled structural vibration and fluid flow. This chapter presents a model for accurate and efficient simulations of the diaphragm-based viscometric glucose sensor. In the model, the fluid-structure coupling between the diaphragm and the sensing fluid in the glucose sensor is presented via the theory of squeeze-film damping and vibrations of pre-stressed diaphragms. The resulting first-principle-based model can be evaluated from the device's geometric and material properties, and quantitatively determine the device response to vibrational excitations at varying glucose concentrations.

2.1 Introduction

Coupling dynamics of viscous flow and structural vibration is a signature of many micro- and nanoscale devices such as microelectromechanical systems (MEMS) and the atomic force microscopy (AFM) instruments. Fluid dynamics strongly influences the motion of microscopic components immersed in a fluid. Conversely, the motion of solid components can generate oscillating viscous flow that impacts the fluid dynamics. These fluid-structure interaction (FSI)

phenomena fundamentally determine the behavior, of micro- and nanoscale devices in applications such as sensing, actuating and energy harvesting [47, 48] [49]. To explain this physics, various numerical and theoretical models have been developed that account for the effect of confined fluid flow surrounding vibrational microstructure; models exist for flexural, torsional and extensional vibrational beams and plates as those used in the AFM, microfluidics and MEMS [50-52].

One commonly applied numerical scheme for simulating fluid flow with moving solid is the Arbitrary Lagrangian-Eulerian (ALE) method. The ALE approach uses a body-fitted computational mesh structure that conforms to boundaries at all times that is limited by frequent remeshing in order to prevent the distortion of mesh and ensure accuracy [53]. Such remeshing procedure is computationally expensive making ALE unsuitable for complex three-dimensional problems [54]. In contrast, analytical models allow obtaining the physical insight in a computational efficient manner. The analytical model using hydrodynamic function has been applied to analyze the frequent response of the vibrational rectangular beam [55]. This model calculates the hydrodynamic load on the infinitely long rigid beam of identical cross section via a complex-valued function called the hydrodynamic function, which is found by solving the Fourier-transformed Stokes equation. However, the hydrodynamic function approach is often limited to studying simple structures with infinite length as well as the fluid unbounded in space. While a number of theoretical studies have been carried out on the fluid structure interaction in unbounded flows, an analytical model capable of predicting the structural dynamic response in highly confined viscous flows that is essential to micro and nano scale applications has hitherto remained elusive.

Recently, we note that a theoretical study of vibrational cantilever beam in a bounded fluid domain has appeared on the literature [56]. However, the model presented in the literature considers an inviscid flow in a bounded geometry, and therefore cannot be used to give predictions of hydrodynamic dissipation effects required for applications involving viscous liquid.

In this chapter, we present a model that accounts for both the dissipative effects in the fluid and the effect of confinement on the flow. The model also considers in-plane forces on constrained thin film structure as intrinsic stress often develops in films during deposition or growth in micro/nano fabrication and is therefore capable of predicting the dynamic behavior of vibrational microstructure in viscous bounded fluids. Using the present model, the dynamic response of the viscometric sensor is determined in a priori manner from the material and geometric properties of the sensor as well as the properties of fluids. Finally, we present a comparison and assessment of the present model with detailed experimental results, finding that the model reveals the general trend in the experimentally observed glucose sensor characteristics with nominal material properties. Thus, the model enables efficient and accurate quantitative determination of dynamic characteristics of viscometric affinity glucose sensor and can be extended to other MEMS and microscopic devices involving complex fluid structure interaction.

2.2 Fluid-Structure Interaction Model

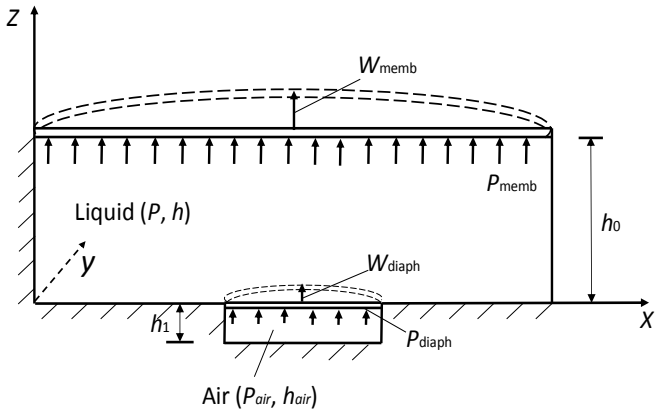

Figure 2–1: Schematic of a diaphragm-based viscometric glucose sensor.

The model represents a MEMS viscometric affinity glucose sensor that has been demonstrated experimentally to be capable of continuous glucose monitoring, based on the dependence of the viscosity of a boronic acid-derivatized polymer solution on the concentration of glucose present in the solution [45]. In the model (Figure 2-1), the liquid (i.e., the polymer solution) is contained in a rectangular microchamber. The chamber's upper wall is a compliant, semi-permeable membrane, and its lower wall consists of a rigid, rectangular ring-shaped surface enclosing a compliant diaphragm. The diaphragm, free freestanding over an air-containing gap, is integrated with permalloy thin-film strips and vibrates under magnetic actuation. The deflection of the diaphragm is measured via a capacitive sensor formed between an electrode embedded in the diaphragm and a second electrode at the bottom of the air gap. Glucose molecules permeate into and out of the microchamber through the semipermeable membrane, thereby changing the viscosity of the liquid and hence the damping on the diaphragm vibration.

During operation of the device, the diaphragm vibrates under the driving force applied by an

external magnetic field on the permalloy strips. The diaphragm induces flow of the liquid, and this fluid flow will in turn change the hydrodynamic force on the diaphragm and influencing the vibration. Additionally, the fluid flow also causes the semi-permeable membrane, which is compliant, to vibrate, and the membrane vibration impacts the flow as well. We describe a representation and solution of the problem for the glucose sensor model in Figure 2-1, while noting that the general approach can be validly extended to other devices involving coupled structural motion and confined-geometry fluid flow.

Diaphragm and Semi-Permeable Membrane Vibrations

The diaphragm and semipermeable membrane are each modeled as a thin plate with uniform thickness. The plate is assumed to be made of a homogeneous, isotropic and linearly elastic material. The deflection of the plate is assumed to be small compared to the plate thickness. The pre-existing in-plane stress is assumed to be uniformly tensile and does not vary with either orientation or position.

The deflection, denoted w, of the plate at a point (x, y) at time t under a distributed lateral load p is governed by:

$$\rho \frac{\partial^2 w}{\partial t^2} + Lw = p, \quad \text{with} \quad w\big|_{\Gamma} = 0 \text{ and } \left.\frac{\partial w}{\partial n}\right|_{\Gamma} = 0 \tag{1}$$

where the linear operator L is defined by

$$Lw = \frac{\partial^2}{\partial x^2}\left(D\frac{\partial^2 w}{\partial x^2}\right) + \frac{\partial^2}{\partial y^2}\left(D\frac{\partial^2 w}{\partial y^2}\right) + 2\frac{\partial^2}{\partial x \partial y}\left(D\frac{\partial^2 w}{\partial x \partial y}\right) + \frac{\partial^2}{\partial x^2}\left(\nu D\frac{\partial^2 w}{\partial y^2}\right) + \frac{\partial^2}{\partial y^2}\left(\nu D\frac{\partial^2 w}{\partial x^2}\right) - 2\frac{\partial^2}{\partial x \partial y}\left(\nu D\frac{\partial^2 w}{\partial x \partial y}\right) - N\left(\frac{\partial^2 w}{\partial x^2} + \frac{\partial^2 w}{\partial y^2}\right) \quad (2)$$

with $D = Eh^3/[12(1-\nu)]$ the flexural modulus of the plate. In these equations, ρ, E and ν are respectively the density, Young's modulus and Poisson's ratio of the plate. In addition, N is the tensile force per unit length of the plate, while n is the outward pointing normal to the boundary (denoted Γ), respectively.

To solve Eq. (1) for the forced plate vibration, consider the homogenous problem of unforced vibration of the plate: $\rho\frac{\partial^2 w}{\partial t^2} + Lw = 0$, subject to the same boundary conditions. Assuming a harmonic solution of the form $w = \Phi(x,y)e^{i\omega t}$ yields the following characteristic equation:

$$L\Phi - \rho\omega^2\Phi = 0, \quad \text{with} \quad \Phi\big|_\Gamma = 0 \text{ and } \left.\frac{\partial\Phi}{\partial n}\right|_\Gamma = 0 \quad (3)$$

Solving for nontrivial solutions of this equation yields the natural frequencies, ω_i and the associated modal functions, $\Phi_i(x, y)$, where i = 1, 2, 3, … The solution to the forced vibration problem, Eq. (1), can then be written as:

$$w = \sum_{j=1}^{\infty} \Phi_j(x,y) q_j(t) \quad (4)$$

where q_i is the magnitude of the i^{th} vibration mode. Substituting this expression into Eq. (1), multiplying both sides of the resulting equation by the modal function Φ_i (i = 1, 2, 3, …), and integrating over the plate region (A) yields $\sum_{j=1}^{\infty}\left(\int_A \rho\Phi_i\Phi_j dA\right)\ddot{q}_j + \left(\int_A \Phi_i L\Phi_j dA\right)q_j = \int_A p\Phi_i dA$

It can be shown that the modal functions are orthogonal:

$$\int_A \rho\Phi_i\Phi_j dA = m_i\delta_{ij}, \quad \text{and} \quad \int_A \Phi_i L\Phi_j dA = m_i\omega_i^2\delta_{ij} \quad (5)$$

where $m_i = \int_A \rho\Phi_i^2 dA$. Using appropriate scaling to normalize each of the modal functions, we can

further obtain $m_i = m = \int_A \rho dA$ where m is the mass of the plate. Thus, the plate vibration can be formulated in terms of the modal magnitudes, q_n:

$$m\ddot{q}_i + m\omega_i^2 q_i = \int_A p\Phi_i dA \tag{6}$$

The formulation given by Eqs. (1)-(6) is used to describe the vibrations of both the diaphragm (with deflection w^{D}) and the semipermeable membrane (with deflection w^{M}). We will also denote all other quantities associated with the diaphragm deflection by the superscript 'D', and those associated with the semipermeable membrane deflection by the superscript 'M'. Thus, by formally adding the superscript 'D' or "M" as appropriate, Eqs. (1)-(6) provide a complete formulation for determining the vibrations of the diaphragm and semipermeable membrane, respectively.

Flow of Liquid

We first introduce a number of characteristic parameters that are constants providing the orders of magnitude of the relevant physical parameters in the glucose microsensor model. First, the characteristic frequency, ω_{c}, and the characteristic deflection, δ_{c}, are constants giving the orders of magnitude of the vibration frequency and diaphragm or membrane deflection, respectively. This allows the characteristic flow velocities to be determined to be $u_{zc} = \omega_{\mathrm{c}}\,\delta_{\mathrm{c}}$ in the z-direction, and $u_{xc} = u_{yc} = u_{zc}\,(L/h_0)$ in the x- and y-directions, where L is the lateral characteristic dimension of the device chamber. Additionally, the characteristic pressure is given by $p_{\mathrm{c}} = \mu\omega_{\mathrm{c}}\delta_{\mathrm{c}}L^2 / h_0^{\,3}$.

Next, the order of magnitude of the force on the diaphragm from air flow and liquid flow is estimated. The shear stress from the liquid and the air on the diaphragm each has the order of

magnitude $\sim \mu u_{xc}/h$, so that we compare the order of magnitude of the pressure with that of the shear stress on the diaphragm from the liquid and the air: $p/\tau \sim L/h_0 >> 1$. Thus, the shear stress can be neglected and pressure is dominant in the forces on the diaphragm from the liquid flow and the air flow. The pressure in the liquid film ($\sim \mu\omega_c\delta_c L^2/h_0^3$) is one order of magnitude greater than that of the air film ($\sim \mu_a\omega_c\delta_c L_a^2/h_1^3$). Therefore, force from air flow on the diaphragm can be neglected in this study.

The characteristic flow rate through the semipermeable membrane is defined as $Q_c = P_c/(rA_m)$, where P_c is the characteristic actuation pressure, r is the flow resistance per unit area of membrane and A_m is the area of membrane, which allows the determination of the characteristic flow velocity through the membrane: $u_c = Q_c/\varepsilon A$, where A is the area of the semipermeable membrane and ε is the porosity of the membrane. It is assumed that $u_c << \omega_c \delta_c$, so that bulk flow through semi-permeable membrane is negligible.

Next, we assume the stress relaxation time of the polymer solution (defined as the time required for the stress applied on the polymer to decay to $1/e$ =36.8% of its initial value [57]) $\tau \rightarrow 0$, thus neglecting the viscoelasticity of the polymer solution and considering the solution as a Newtonian fluid.

The liquid confined between the semipermeable membrane and the diaphragm is modeled by the lubrication theory. Since $|w^M - w^D| << h_0$ and $|w^D| << h_1$, the pressure in the liquid chamber $P|_{z=h}$ can be linearized. The pressure variation across the liquid chamber and across the air containing gap is considered to be negligibly small. Next, define an out-of-plane Reynolds number R_z =

$\rho_0 u_{zc} h_0/\mu_0$ (~0.01) and an in-plane Reynolds number $R_x = (\rho_0 u_{xc} h_0/\mu_0)(h_0/L) = R_z$. these Reynolds numbers are of order h_0/L (~0.1) or smaller, inertial effects in the flow can be ignored when compared with viscous and pressure effects. Subject to these conditions, the classical Reynolds equation of lubrication theory [58] adequately describes the hydrodynamics of the fluid film in the liquid chamber:

$$\nabla \cdot (h^3 \nabla p) = 12\mu \dot{h}, \quad \text{with} \quad \left.\frac{\partial p}{\partial n}\right|_{\Gamma} = 0 \tag{7}$$

Define a characteristic fluid film thickness h_c, where $h_c = h_0$ for the liquid film

$$\frac{h_c^3}{12\mu} \nabla^2 p = \dot{h}, \text{ with } \left.\frac{\partial p}{\partial n}\right|_{\Gamma} = 0 \tag{8}$$

The fluid film pressure p can also be normalized using $\bar{p} = p / p_c$, where p_c is the characteristic pressure given in the beginning of this subsection. Thus, equation (8) becomes:

$$\frac{h_c^3 p_c}{12\mu} \nabla^2 \bar{p} = \dot{h}, \text{ with } \left.\frac{\partial p}{\partial n}\right|_{\Gamma} = 0 \tag{9}$$

For the fluid film in the liquid chamber, $h=h_0 + (w^M - w^D)$. Therefore, the time rate of fluid film thickness change is $\dot{h} = \sum_{i=1}^{\infty} \Phi_i^M(x,y)\dot{q}_i^M(t) - \sum_{j=1}^{\infty} \Phi_j^D(x,y)\dot{q}_j^D(t)$ for the liquid film.

Substituting $\dot{h}$ into Eq. (9) and by the principle of superposition, pressure in the liquid film p can be expressed as:

$$p = \sum \left(\frac{p_c}{\delta_c}\right) \xi_k^M(x,y)\dot{q}_k^M(t) - \sum \left(\frac{p_c}{\delta_c}\right) \xi_j^D(x,y)\dot{q}_j^D(t) \tag{10}$$

where the dimensionless functions ξ^D and ξ^M are determined from the modal shapes of the vibrating diaphragm and semi-permeable membrane by: $\frac{h_0^3 p_c}{12\mu\delta_c} \nabla^2 \xi_j^D = \Phi_j^D$ and $\frac{h_0^3 p_c}{12\mu\delta_c} \nabla^2 \xi_k^M = \Phi_k^M$, respectively.

Forces on the Membrane and Diaphragm

Associated with the pressure distributed in the liquid chamber, the hydrodynamic pressure on the semipermeable membrane can be expressed as

$$p^{\mathrm{M}} = p = \sum\left(\frac{p_{\mathrm{c}}}{\delta_{\mathrm{c}}}\right)\xi_{k}^{\mathrm{M}}(x,y)\dot{q}_{k}^{\mathrm{M}}(t) - \sum\left(\frac{p_{\mathrm{c}}}{\delta_{\mathrm{c}}}\right)\xi_{j}^{\mathrm{D}}(x,y)\dot{q}_{j}^{\mathrm{D}}(t)\,.$$

Forces on the semipermeable membrane can thus be evaluated as:

$$F^{\mathrm{M}} = \int p^{\mathrm{M}}\Phi_{i}^{\mathrm{M}}dA = \int\left(\frac{p_{\mathrm{c}}}{\delta_{\mathrm{c}}}\right)(\sum\xi_{k}^{\mathrm{M}}\dot{q}_{k}^{\mathrm{M}}\Phi_{i}^{\mathrm{M}} - \sum\xi_{j}^{\mathrm{D}}\dot{q}_{j}^{\mathrm{D}}\Phi_{i}^{\mathrm{M}})dA = \left(\frac{p_{\mathrm{c}}}{\delta_{\mathrm{c}}}\right)\sum\dot{q}_{k}^{\mathrm{M}}\int\xi_{k}^{\mathrm{M}}\Phi_{i}^{\mathrm{M}}dA - \left(\frac{p_{\mathrm{c}}}{\delta_{\mathrm{c}}}\right)\sum\dot{q}_{j}^{\mathrm{D}}\int\xi_{j}^{\mathrm{D}}\Phi_{i}^{\mathrm{M}}dA\,.$$

Let $\alpha_{ij} = \int\Phi_{i}^{\mathrm{M}}\xi_{j}^{\mathrm{D}}dA^{\mathrm{M}}$, $\beta_{ik} = \int\Phi_{i}^{\mathrm{M}}\xi_{k}^{\mathrm{M}}dA$, equation (6) that accounts for the vibration of the semi-permeable membrane becomes

$$m_{\mathrm{M}i}(\ddot{q}_{i}^{\mathrm{M}} + \omega_{\mathrm{M}i}^{2}q_{i}^{\mathrm{M}}) - \frac{p_{\mathrm{c}}}{\delta_{\mathrm{c}}}\sum\beta_{ik}\dot{q}_{k}^{\mathrm{M}} + \frac{p_{\mathrm{c}}}{\delta_{\mathrm{c}}}\sum\alpha_{ij}\dot{q}_{j}^{\mathrm{D}} = 0 \tag{11}$$

The pressure on the diaphragm is given by $p^{\mathrm{D}} = p_{\mathrm{ext}} - p = p_{\mathrm{ext}} - \frac{p_{\mathrm{c}}}{\delta_{\mathrm{c}}}(\sum\dot{q}_{j}^{\mathrm{D}}\xi_{j}^{\mathrm{D}} - \sum\dot{q}_{k}^{\mathrm{M}}\xi_{k}^{\mathrm{M}})$.

Consequently, the force on the actuated diaphragm is

$$\int_{A^{\mathrm{D}}} p^{\mathrm{D}}\Phi_{i}^{\mathrm{D}}dA = \int_{A^{\mathrm{D}}} p_{\mathrm{ext}}\Phi_{i}^{\mathrm{D}}dA + \frac{p_{\mathrm{c}}}{\delta_{\mathrm{c}}}\sum\dot{q}_{j}^{\mathrm{D}}\int_{A^{\mathrm{D}}}\Phi_{i}^{\mathrm{D}}\xi_{j}^{\mathrm{D}}dA - \frac{p_{\mathrm{c}}}{\delta_{\mathrm{c}}}\sum\dot{q}_{k}^{\mathrm{M}}\int_{A^{\mathrm{D}}}\Phi_{i}^{\mathrm{D}}\xi_{k}^{\mathrm{M}}dA$$

Let $\sigma_{ij}^{\mathrm{D}} = \int_{A^{\mathrm{D}}}\Phi_{i}^{\mathrm{D}}\xi_{j}^{\mathrm{D}}dA$ and $\tau_{ik} = \int_{A^{D}}\Phi_{i}^{\mathrm{D}}\xi_{k}^{\mathrm{M}}dA$. Substituting the expression of the force on diaphragm into equation (6) yields

$$m_{i}(\ddot{q}_{i}^{\mathrm{D}} + \omega_{i}^{2}q_{i}^{\mathrm{D}}) - \frac{p_{\mathrm{c}}}{\delta_{\mathrm{c}}}\sum\sigma_{ij}\dot{q}_{j}^{\mathrm{D}} + \frac{p_{\mathrm{c}}}{\delta_{\mathrm{c}}}\sum\tau_{ik}\dot{q}_{k}^{\mathrm{M}} = \int_{A^{D}} p_{\mathrm{ext}}\Phi_{i}^{\mathrm{D}}dA \tag{12}$$

Steady-State Vibrations

The governing equations for the vibrating systems are a system of differential equations that can be expressed in a matrix form of Eqs. (11) and (12). The component of the electromagnetic

force normal to the diaphragm is $F = F_0 e^{j\omega t} = B^2 A/(2\mu_0)\, e^{j\omega t}$, where B is the amplitude of the magnetic field normal to the diaphragm exerted by a solenoid, A is the solenoid's cross-sectional area and μ_0 is the permeability of space. This Under the harmonic excitation $F = F_0 e^{j\omega t}$, the steady state response of the system is $u=|U|e^{-j\varphi}e^{j\omega t}$, where $|U|e^{-j\varphi}$ is the complex amplitude with the amplitude ($|U|$) and phase shift (φ) of the dynamic system. It follows that we can calculate $U=|U|e^{-j\varphi} = (K-\omega^2 M-j\omega C)^{-1}F_0$ by defining

$$u = \begin{bmatrix} q_1^{\mathrm{D}} \\ \vdots \\ q_n^{\mathrm{D}} \\ q_1^{\mathrm{M}} \\ \vdots \\ q_n^{\mathrm{M}} \end{bmatrix},$$

$$K = \begin{bmatrix} m_1\omega_1^2 & & & & & & \\ & \ddots & & & & & \\ & & m_n\omega_n^2 & & & & \\ & & & m_{\mathrm{M}1}\omega_{\mathrm{M}1}^2 & & & \\ & & & & \ddots & & \\ & & & & & m_{\mathrm{M}m}\omega_{\mathrm{M}m}^2 \end{bmatrix},$$

$$M = \begin{bmatrix} m_1 & & & & & \\ & \ddots & & & & \\ & & m_n & & & \\ & & & m_{\mathrm{M}1} & & \\ & & & & \ddots & \\ & & & & & m_{\mathrm{M}m} \end{bmatrix},$$

$$C\dot{u} = \begin{bmatrix} \vdots \\ -\frac{P_{\mathrm{c}}}{\delta_{\mathrm{c}}}\sum \sigma_{ij}\dot{q}_j^{\mathrm{D}} + \frac{P_{\mathrm{c}}}{\delta_{\mathrm{c}}}\sum \tau_{ik}\dot{q}_k^{\mathrm{M}} \\ \vdots \\ -\frac{P_{\mathrm{c}}}{\delta_{\mathrm{c}}}\sum \beta_{ik}\dot{q}_k^{\mathrm{M}} + \frac{P_{\mathrm{c}}}{\delta_{\mathrm{c}}}\sum \alpha_{ij}\dot{q}_j^{\mathrm{D}} \end{bmatrix},$$

$$F = \begin{bmatrix} \vdots \\ F_0 \\ \vdots \\ 0 \end{bmatrix} e^{j\omega t}$$

2.3 Results and Discussion

In this section, the model is validated with experimental data obtained from an affinity glucose sensor [45]. The affinity glucose sensor measured the glucose concentration in a physiologically relevant range (30- 360 mg/dL). When the sensor was under the excitation of a harmonically time-varying magnetic field, the steady-state amplitude and phase of the diaphragm vibration as a function of the excitation frequency was obtained in terms of the output voltage of a measurement circuit. The sensor had an actuated diaphragm with dimensions of 400 × 200 × 6 μm^3, and the semi-permeable membrane has dimensions of 5 mm × 5 mm × 20 μm^3. Moreover, the Young's modulus, Poisson's ratio and density for the semi-permeable membrane (cellulose acetate) are E = 4 GPa, v = 0.39 and ρ = 1300 kg/m^3, and for the vibrational diaphragm (Parylene) are E = 4 MPa, v = 0.4 and ρ = 1289 kg/m^3, respectively. We start by solving the characteristic Eq. (3), the modal shape of actuated diaphragm Φ^D and the modal shape of the semi-permeable membrane Φ^M were obtained in term of in-plane force N. Substituting Φ^D and Φ^M, Poisson's equations were solved with finite difference method using MATLAB for ζ and η in terms of h_0, which are normalized pressure in the squeezed fluid film associated with the moving diaphragm and the semi-permeable membrane. Subsequently, calculating the coefficients α_{ij}, β_{ij}, σ_{ij} and τ_{ij} using the modal shapes and the normalized pressure yields components of the damping coefficients.

In the experiments, it was difficult to precisely determine the values of the in-plane forces N, the magnetic flux intensity B and the height of the liquid chamber h_0. Hence, these parameters are allowed to vary such that the theoretical solutions are the best fit for the experimental data. Here, recall that the steady state response of the actuated diaphragm $U = Ae^{i\varphi} = (K-\omega^2 M-j\omega C)^{-1}F_0$, we can obtain the deflection of the diaphragm $\hat{y}_i = \sum_{k=1}^{n} \Phi_k(x_0, y_0)[(K - \omega_i^2 M - j\omega_i C)^{-1} F_0]_k$, where $\Phi_k(x_0, y_0)$ is the modal shape at the midpoint (x_0, y_0) of the diaphragm. Fitting the model to the experimental data for the 30 mg/dL glucose concentration yielded B = 0.01 T, which is consistent with practical values (0.01 – 0.5 T) generated by a similar solenoid (400 turns of a 250-μm-diameter copper wire on a plastic core), h_0 = 543 μm, which is less than a 10% deviation from the nominal design value and N = 270 N/m, which corresponds to a 45-MPa in-plane stress that is in the range of 21- 50 MPa reported for Parylene [59]. The model can also be fitted to the experimental data obtained at other glucose concentrations. The value of B is consistently estimated to be almost constant at 0.01 T, with variations less than 1.2%. In addition, as the glucose concentration varies from 30 to 210 mg/dL, the estimated in-plane force N changes only by 0.7% while variations of the height of the liquid chamber are within 5%. Figure 2-2 shows least square fits of the model to the experimental data at 30, 90 and 210 mg/dL. As can be seen from the figure, the model agrees with the experimental data well, considering the model must fit two sets of experimental data (Asinφ and Acosφ) with a single set of parameter estimates.

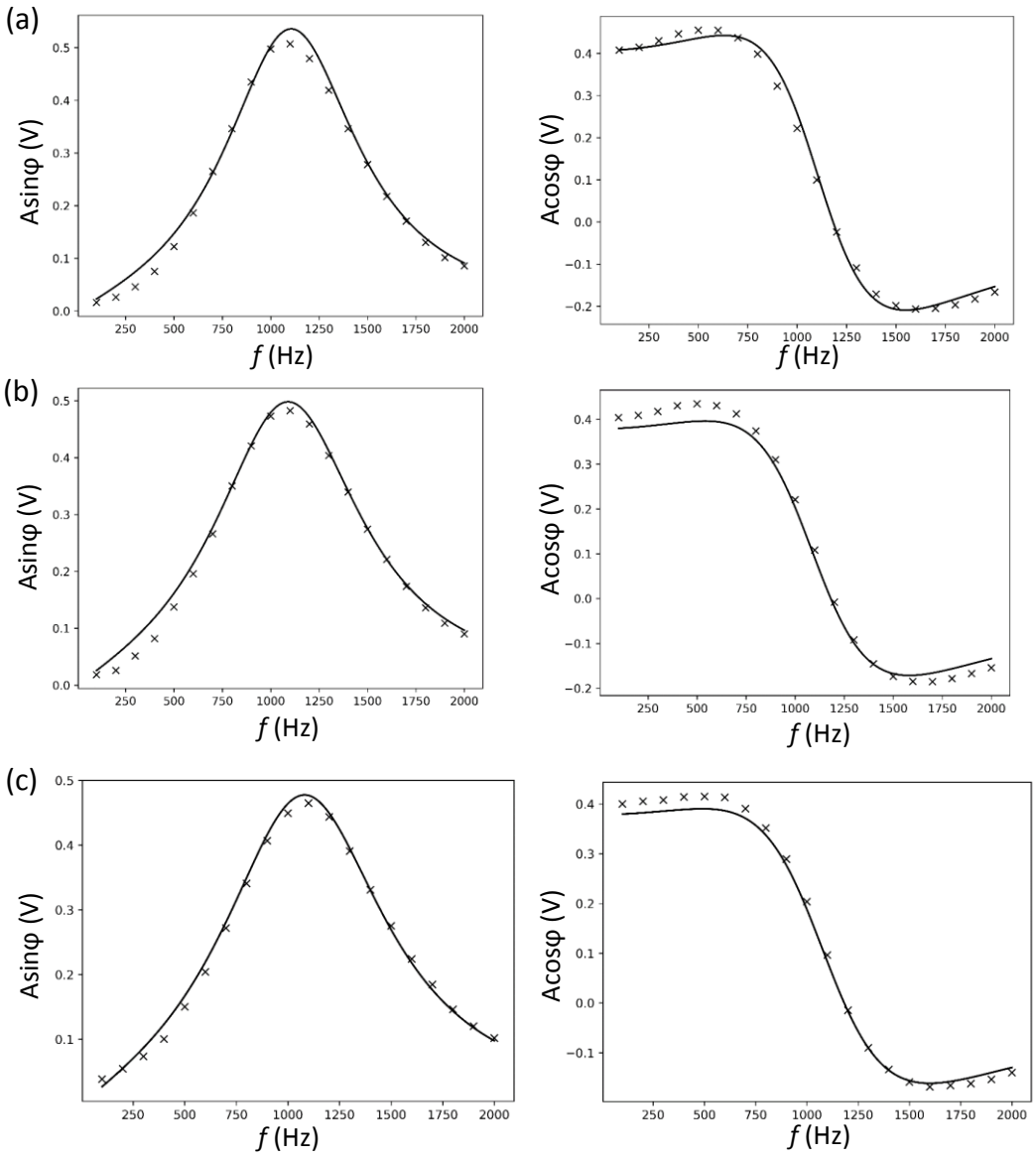

Figure 2–2: The model (solid lines) compared to experimentally determined (cross symbol) complex amplitude {Asinφ, Acosφ} of the viscometric sensor output at a glucose concentration of (a) 30 mg/dL, (b) 90 mg/dL and (c) 210 mg/dL.

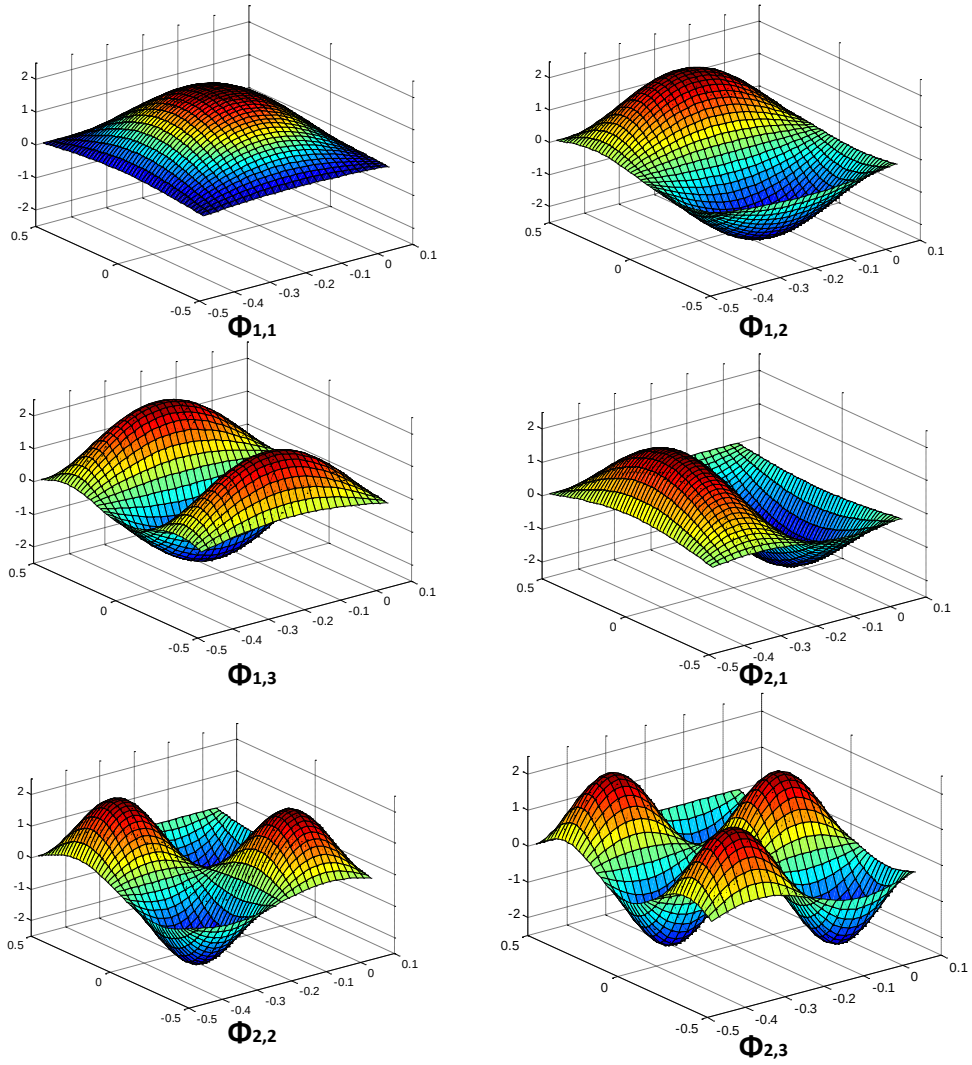

Figure 2–3: The first six modal shapes of the diaphragm.

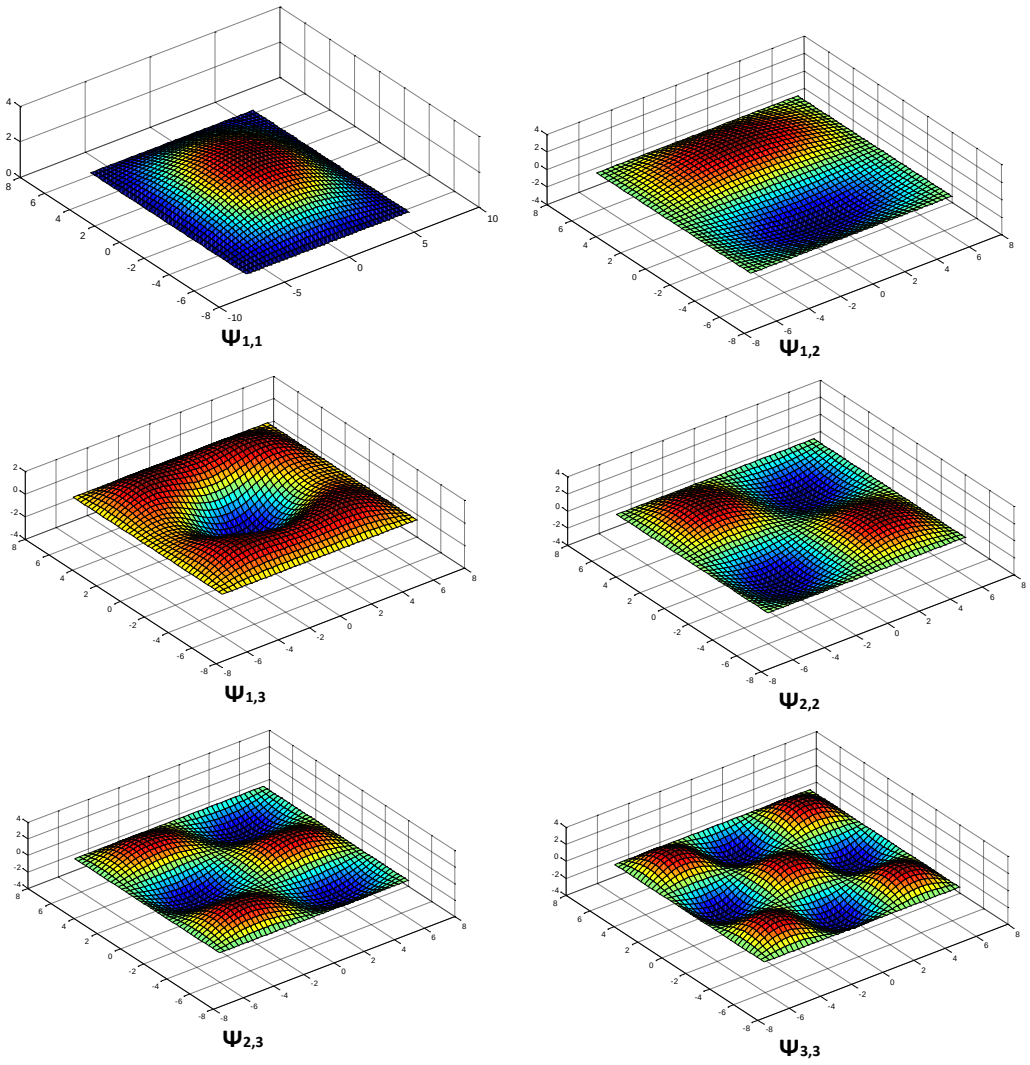

Figure 2–4: The first six modal shapes of the semi-permeable membrane.

Using the above-determined values of B, N and h_0, the modal shapes of the diaphragm and the semi-permeable membrane are respectively obtained (Figures 2-3 and 2-4). Zero displacements at all boundaries are observed in the modal shapes for both the diaphragm and the membrane, which implies clamped boundaries of plates. It is also noted that there is an increase in the number of peaks in the modal shapes as the order of vibration mode increases.

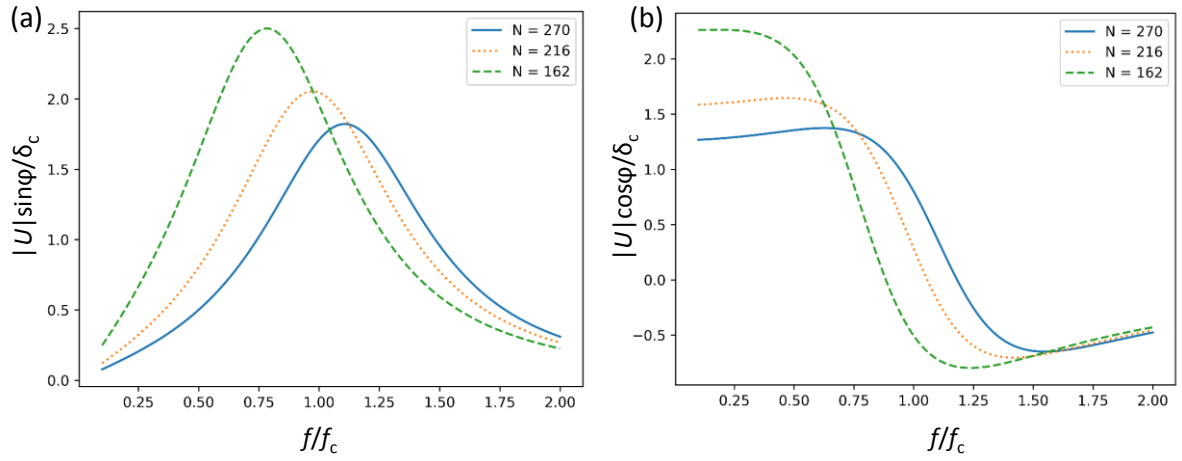

Figure 2–5: Vibrational amplitude of the actuated diaphragm with various pretensions (N = 270, 216 and 162 N/m) in 30 mg/dL glucose solution.

Varying the in-plane stress of the actuated diaphragm may be proved to change the glucose sensor's dynamic response. At a glucose concentration of 30 mg/dL, a series of curves for the frequency response of the sensor are shown in Figure 2-5, given material properties used in validating the experimental data. The pretension of the diaphragm is varied between 270 N/m and 162 N/m, which corresponds to an in-plane stress between 45 MPa and 27 MPa that is within the range of values reported for Parylene [59]. It is evident that reducing the in-plane stress of the diaphragm from 270 N/m to 162 N/m would cause a left shift of the excitation frequency, at which the deflection of the diaphragm reaches its peak value. This imply the resonance of the diaphragm with smaller pretension requires a lower frequency or energy to excite. In contrast, increased pretension would increase the resonant frequency.

It is also interesting to learn the impact of tuning device's geometric properties on the frequency-dependent dynamics of the actuated diaphragm. Following study focuses on the

deflection (normalized by the characteristic deflection δ_c) of the actuated diaphragm as a function of actuation frequency, varying the height of the liquid chamber h_0. The results in Figure 2-6 (a) show that, the deflection of the diaphragm increases as the height of the liquid chamber h_0 increases from 500 to 600 μm, as a hike in the thickness of the fluid film decreases effect of hydrodynamic damping. Meanwhile, it is also interesting to note that the curves representing deflection $|U|\cos\varphi/\delta_c$ in Figure 2-6 (b) intersect at an excitation frequency $f/f_c = 1.18$, at which the phase angle φ is close to 90̊, which suggests the natural frequency of the diaphragm is around 1180 Hz.

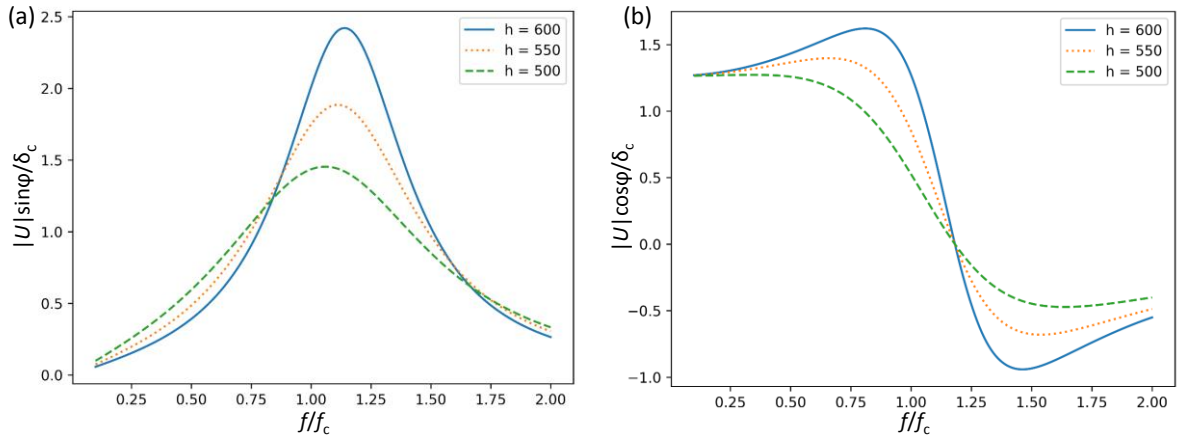

Figure 2–6: Frequency dependence of the diaphragm deflection on the height h of the liquid chamber (diaphragm pretension N = 270 N/m).

As viscometric glucose sensing is based on variations in viscous damping of different polymer-glucose solutions on the vibration of the actuated diaphragm, the damping ratio is estimated to measure of how the dynamic response of sensor decays along with the varying viscosity. As the damping matrix C of the coupled system is non-diagonal, it becomes difficult to estimate the damping ratio for the actuated diaphragm. Here, Rayleigh damping is assumed that the viscous

damping is proportional to a linear combination of stiffness and mass, i.e., $C = a_0M+a_1K$. By equating the diagonal entries of a_0M+a_1K to the eigenvalue of C, the coefficients a_0 and a_1 can be determined and are used for calculating the damping ratio represented by $\frac{1}{2}(\frac{a_0}{\omega_i}+a_1\omega_i)$, where ω_i is the *i*-th natural frequency of the actuated diaphragm. The damping ratio in 5% PAA-ran-PAAPBA polymer solution evaluated by the model increases from 0.34 (without glucose) to 0.46 as the glucose concentration varies from 0 to 210 mg/dL (Figure 2-7). This is consistent with the increased viscosity of the polymer-glucose solution at elevated glucose concentrations.

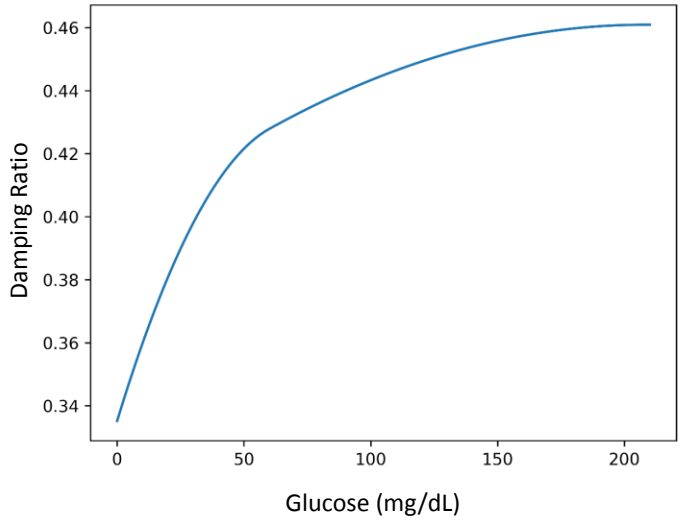

Figure 2–7: Damping ratio obtained by fitting the model to experimental data at varying glucose concentrations.

2.4 Conclusions

This chapter presents a simulation study of the interactions between structural vibrations and highly confined flow in a MEMS diaphragm-based viscometric affinity glucose sensor. Vibrations of the diaphragm and the semi-permeable membrane in the device are described by those of

prestressed plates, and the fluid flow in the confined geometry of the device chamber is described using lubrication theory. Coupling between the vibrations and fluid flow is accounted by calculating forces from structural vibrations on the fluid flow as well as those from fluid flow on the vibrations. The resulting model can be evaluated directly by solving differential equations with the device's geometric and materials properties. We have used the model to conduct a parametric study of the impact of the geometry of the device on its dynamic characteristics. Results show that the deflection of the Parylene diaphragm at the resonance frequency decreases with the height of liquid chamber due to increased squeeze-film damping effects. Results from simulation have been found to correctly reveal the trend in the experimentally observed device response. Thus, this simulation approach enables efficient and accurate quantitative determination of the viscometric affinity glucose sensor, and can be extended to other MEMS devices involving fluid-structure interactions.

Chapter 3. Understanding Viscometric Glucose Sensing: Cantilevers Vibrating in Fluids

This chapter presents a theoretical study of microcantilever-based viscometric glucose sensors [27] [46]. This work differentiates from the diaphragm model by relaxing the thin-film assumption and applying the model of unsteady stokes flow to analyze a harmonic flow field. The structural vibration of the cantilever is coupled with the flow via satisfying dynamic and kinematics boundary conditions at the cantilever beam-liquid interface. Subsequently, the model is exploited to parametrically study the device's dynamic characteristics from the geometric and material properties of the viscometric glucose sensor. Additionally, the impact of the surface stress on the cantilever dynamics is evaluated as well as the dynamic response of the cantilever under thermal excitation.

3.1 Introduction

Microcantilevers in dynamic mode have a wide range of applications in sensors and actuators. For example, they can be used for flow sensing [60], pH measurement [61], stress sensing [62], detection of target analytes [63], and scanning probe microscopy [64]. Challenges from characterization of a microcantilever immersed in a fluid. Many of these applications are conducted in aqueous environment, which involves coupled structural vibration and liquid flow. For example, we have previously reported a microcantilever-based affinity glucose sensor that detects the glucose molecules in a polymer solution. In this sensor, the dynamic response of the

microcantilever is strongly dependent on the viscosity of the polymer solution, which varies with the concentration of glucose [27]. In addition to the liquid surrounding the microcantilever, the presence of a solid boundary confining the liquid is another factor that can significantly affect the frequency response of the cantilever sensor. Realizing that the sensing system is relying upon the change in response of the cantilever due to the change in the aqueous environment, it is therefore important to conduct a fundamental analysis understanding the dynamics of a cantilever, or arrays of cantilevers, in a viscous bounded liquid.

Analysis of the dynamic response of a cantilever in the absence of fluid can be obtained using simple analytical techniques [65]. Calculation of cantilever in unbounded liquid. In contrast, calculation of the frequency response of a cantilever immersed in a fluid is of great challenge, which have been the subject of numerous theoretical and numerical investigations. For example, Sader presented a theoretical analysis of the frequency response of a cantilever immersed in an unbounded viscous fluid, in which a transfer function was formulated to calculate the hydrodynamic load from the deflection of the cantilever [55]. Sader's formulation has been subsequently used to study the torsional frequency response [66], influence of mode orders on the frequency response [67] as well as stochastic response [68], of a cantilever immersed in a viscous fluid. Calculation of cantilever in liquid with infinite boundary. As many of practical applications for microcantilevers require a geometry to confine the liquid, or at least with the presence of a solid wall, Green et al., presented a boundary integral formulation that considers the effect of a nearby surface on the dynamic response of a cantilever immersed in a viscous liquid. However,

Green's formulation, which is particularly useful for calculating the hydrodynamic loading on a cantilever beam near a solid surface, assumes that the surface near which the cantilever is oscillating is infinite [69]. Therefore, this model is not directly applicable to the case in which we are interested in, namely a microcantilever sensor confined with a viscous liquid.

To address fluid-structure interactions in a finite body of viscous liquid, we have previously reported a model of a thin plate vibrating in the confined fluid. Using the squeeze-film damping model, we assumed a thin film of fluid between a confined geometry and calculated the dynamic response of the vibrating plate. In this work, we present a viscous flow-microcantilever interaction model that is derived from the Navier-Stokes equation and Euler-Bernoulli beam theory. This model allows efficient simulations of harmonic vibrations of a microcantilever in a viscous flow that is not limited to a thin film flow. A two-way fluid-structure interaction has been realized that effectively captures impact of the fluid flow on the cantilever vibration and fluctuation of cantilever-induced liquid flow. The model also enables simulation of harmonic vibration of a microcantilever that is interacted with biomolecules in a liquid. Additionally, the model is applicable to simulations of a microcantilever's thermally driven motion, which can potentially be used in determining cantilever stiffness for Atomic Force Microscope measurements. Applying the model correctly reveals the trend in the experimentally observed microcantilever-based device responses, demonstrating the model's utility as an efficient tool for simulating viscous flow-microcantilever interaction. Examining the dynamic response of the cantilever under thermal excitation has found that the thermal noise does not change monotonically with Reynolds number

and the variation of the noise is strongly dependent on the intensity of viscous dissipation, which will be of significant practical value to precise measurements.

3.2 Model for Interactions between Cantilever Motion and Viscous Flow

A theoretical formalism to investigate the dynamic behavior of microcantilever under isotropic in-plane stress loads and hydrodynamic loads is schematically presented; see Figure 3-1. The microcantilever can be characterized by its material properties (Young's modulus E, Poisson's ratio υ and density ρ) and dimensions (length l, width b and thickness h). The distances from the cantilever to bottom and top walls (h_1 and h_2) are given for evaluation of the boundary effect on the microcantilever's dynamic behavior. Adopting a 2D domain, we assume that the deflection of the microcantilever is much smaller than any length scale in the beam geometry, and define the wall boundaries Γ_w, cantilever-fluid interface Γ_c as well as fluid-fluid interface $\Gamma_{F\text{-}F}$.

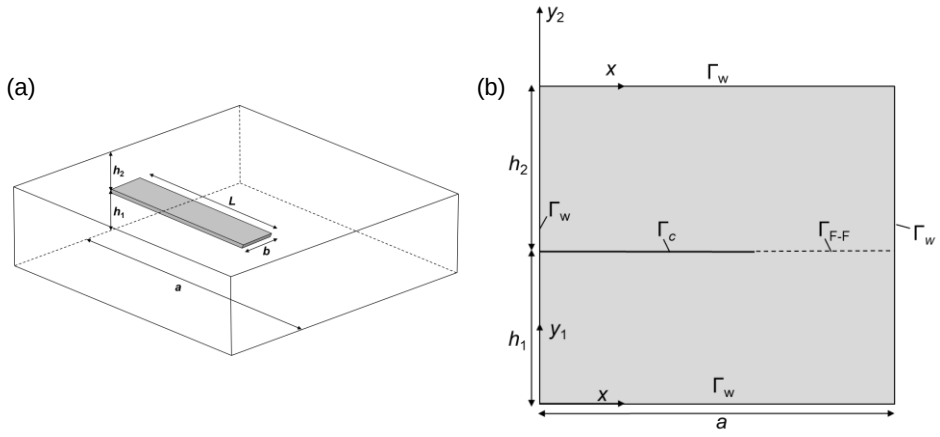

Figure 3–1: (a) Schematic illustration showing the dimension of a rectangular cantilever. (b) 2D domain indicating the boundary and interface of the model.

The Structural Vibration of the Cantilever Beam

We begin with the governing equation for the dynamic deflection function $w(x, t)$ of the microcantilever at the presence of hydrodynamic stress

$$m\frac{\partial^2 w}{\partial t^2}+EI\frac{\partial^4 w}{\partial x^4}-N\frac{\partial^2 w}{\partial x^2}=G+b\sigma_h \tag{1}$$

where E is Young's modulus, I is the moment of inertial of the beam, m is the mass per unit length of the beam, N is a concentrated axial load, G is the force of excitation per unit length, σ_h is the hydrodynamic stress, x is the spatial coordinate along the length of the beam and t is the time.

Next, considering solving the characteristic equation for the microcantilever, the clamped boundary conditions are applied to the left end of the beam. At the right end of the beam, a concentrated bending moment $Nt/2$ and the axial load N are applied to model the effect of the surface stress [70].

$$\begin{cases} EI\dfrac{d^4\xi_j}{dx^4}-N\dfrac{d^2\xi_j}{dx^2}-m{\omega_j}^2\xi_j=0 \\ \xi_j(0)=0,\ \dfrac{d\xi_j(0)}{dx}=0,\ \dfrac{d^2\xi_j(L)}{dx^2}=\dfrac{Nt}{2},\ \dfrac{d^3\xi_j(L)}{dx^3}-\dfrac{N}{EI}\dfrac{d\xi_j(L)}{dx}=0 \end{cases} \tag{2}$$

The j-th modal shapes can be expressed as

$$\xi_j(x)=A_j\cosh\left(s_{1j}x\right)+B_j\sinh\left(s_{1j}x\right)+C_j\cos\left(s_{2j}x\right)+D_j\sin\left(s_{2j}x\right) \tag{3}$$

where A_j, B_j, C_j, and D_j are coefficients determining the modal shape that can be obtained from the boundary conditions, and

$$s_{1j}=\left[\frac{N}{2EI}+\left(\frac{N^2}{4E^2I^2}+\frac{m{\omega_j}^2}{EI}\right)^{1/2}\right]^{1/2},\quad s_{2j}=\left[\left(\frac{N^2}{4E^2I^2}+\frac{m{\omega_j}^2}{EI}\right)^{1/2}-\frac{N}{2EI}\right]^{1/2} \tag{4}$$

Assume the deflection of the microcantilever beam can be represented by $w(x, t) = \sum \varsigma_j(t)\xi_j(x)$, where $\varsigma_j(t) = S_j e^{i\omega t}$ and $\xi_j(x)$ is the j^{th} modal shape solved in the characteristic equation.

Fluid Flow

We consider the Navier-Stokes equations that governs the flow

$$\begin{cases} \nabla \cdot u = 0 \\ \rho(\dfrac{\partial u}{\partial t} + u \cdot \nabla u) = -\nabla p + \mu \nabla^2 u \end{cases} \tag{5}$$

Define four dimensionless parameters by

$$\bar{u} = u/U,\ \bar{x} = x/L,\ \bar{t} = t/T,\ \bar{p} = p/(\mu U/L)$$

where U is the characteristic velocity of the fluid, L is the characteristic length of the domain, and T is the time scale. Define the Reynolds number $\mathrm{Re} = UL/\upsilon$ and the Strouhal number $\mathrm{St} = L/UT$, the Navier-Stokes equations become

$$\begin{cases} \bar{\nabla} \cdot \bar{u} = 0 \\ \mathrm{Re}\ \ \mathrm{St}\dfrac{\partial \bar{u}}{\partial t} + \mathrm{Re}\ \ \bar{u} \cdot \bar{\nabla}\bar{u} = -\bar{\nabla}\bar{p} + \bar{\nabla}^2 \bar{u} \end{cases} \tag{6}$$

Define a characteristic frequency ω and a characteristic deflection δ, the Reynolds number $\mathrm{Re} = UL/\upsilon = \omega\delta L/\upsilon = 2\pi\delta L/\upsilon T$. Assume the amplitude of the vibrating beam δ is much smaller than any other length scale of the beam. Also, as the velocity field in the fluid will vary slowly across the width of the beam, the width b of the beam is used as the characteristic length [55]. As $L >> \delta$, $\mathrm{Re}\cdot\mathrm{St} = L^2/\upsilon T >> \mathrm{Re} = 2\pi L\delta/\upsilon T$, which allows to neglect the inertial term of the equations (5). The resulting equation is given by

$$\begin{cases} \nabla \cdot u = 0 \\ \rho \dfrac{\partial u}{\partial t} = -\nabla p + \mu \nabla^2 u \end{cases} \tag{7}$$

Meanwhile, we assume the cantilever is under harmonic excitation with a frequency of ω. This gives $u = U(x,y)e^{i\omega t}$, $v = V(x,y)e^{i\omega t}$, $p = P(x,y)e^{i\omega t}$, where U, V, and P are unknown complex functions of space.

$$\begin{cases} \dfrac{\partial U}{\partial x} + \dfrac{\partial V}{\partial y} = 0 \\ \rho i\omega U = -\dfrac{\partial P}{\partial x} + \mu\left(\dfrac{\partial^2 U}{\partial x^2} + \dfrac{\partial^2 U}{\partial y^2}\right) \\ \rho i\omega V = -\dfrac{\partial P}{\partial y} + \mu\left(\dfrac{\partial^2 V}{\partial x^2} + \dfrac{\partial^2 V}{\partial y^2}\right) \end{cases} \tag{8}$$

Using Helmholtz decomposition, the vector **U** (*U*, *V*) representing the velocity field of the flow can be decomposed into a potential flow and a viscous flow. Let $\mathbf{U} = \nabla\phi + \nabla \times \varphi$, where $\nabla\phi$ is a curl-free component and $\nabla \times \varphi$ is a divergence-free component, thus the equations (8) become

$$\begin{cases} \nabla^2 \phi = 0 \\ i\omega\rho\phi + P = 0 \\ \nabla^2 \varphi + \alpha^2 \varphi = 0 \end{cases} \tag{9}$$

where $\alpha^2 = -i\omega\rho/\mu$. By no-slip and no-penetration boundary conditions, $U = \dfrac{\partial \phi}{\partial x} + \dfrac{\partial \varphi}{\partial y} = 0$ and $V = \dfrac{\partial \phi}{\partial y} - \dfrac{\partial \varphi}{\partial x} = 0$ on solid walls. Thus, $\dfrac{\partial \phi}{\partial x} + \dfrac{\partial \varphi}{\partial y} = \dfrac{\partial \phi}{\partial y} - \dfrac{\partial \varphi}{\partial x} = 0$ at the walls. At the liquid-cantilever interface, $\dfrac{\partial w}{\partial t} = V\Big|_{y_1 = h_1} + \dfrac{\partial V}{\partial z}\Big|_{y_1 = h_1}$ $w \approx V\Big|_{y_1 = h_1} = i\omega \sum S_j \xi_j$ in the direction that is normal to the interface assuming harmonic vibration. Thus, boundary conditions at the liquid-cantilever interface are described by $\dfrac{\partial \phi}{\partial x} + \dfrac{\partial \varphi}{\partial y} = 0$, $\dfrac{\partial \phi}{\partial y} - \dfrac{\partial \varphi}{\partial x} = i\omega\Delta$, where $\Delta = \sum S_i \xi_i$.

Next, the domain is divided into the upper and lower area (Figure 3-1b). Applying the wall boundary conditions to Eq. (9), which hence has the following solutions:

At $0<y_1<h_1$

$$\begin{aligned}\phi_1(x,\ y) &= \sum \cos(\lambda_j\ \mathrm{x})[A_{1j}\cosh(\lambda_j y) + B_{1j}\sinh(\lambda_j y)] \\ \varphi_1(x,\ y) &= \sum \sin(\lambda_j\ \mathrm{x})[B_{1j}\cosh(\beta_j y) + (\lambda_j/\beta_j)A_{1j}\sinh(\beta_j y)]\end{aligned} \tag{10}$$

At $-h_2 <y_2<0$

$$\begin{aligned}\phi_2(x, y) &= \sum \cos(\lambda_j\ \mathrm{x})[A_{2j}\cosh(\lambda_j y) + B_{2j}\sinh(\lambda_j y)] \\ \varphi_2(x, y) &= \sum \sin(\lambda_j\ \mathrm{x})[B_{2j}\cosh(\beta_j y) + (\lambda_j/\beta_j)A_{2j}\sinh(\beta_j y)]\end{aligned} \tag{11}$$

where $\lambda_j = \frac{j\pi}{2a},\ \beta_j = \sqrt{\lambda_j^2 - \alpha^2}$

Note that there are two different boundary conditions at the interface between the upper and lower domain

At the cantilever-liquid interface: $\frac{\partial\phi}{\partial x} + \frac{\partial\varphi}{\partial y} = 0,\ \frac{\partial\phi}{\partial y} - \frac{\partial\varphi}{\partial x} = i\omega\Delta$

At the liquid-liquid interface: $\frac{\partial\phi_1}{\partial x} + \frac{\partial\varphi_1}{\partial y} = \frac{\partial\phi_2}{\partial x} + \frac{\partial\varphi_2}{\partial y},\ \frac{\partial\phi_1}{\partial y} - \frac{\partial\varphi_1}{\partial y} = \frac{\partial\phi_2}{\partial y} - \frac{\partial\varphi_2}{\partial y}$

These boundary conditions can be written in terms of the location,

At $0<y_1<h_1$

$$\begin{aligned}\left(\frac{\partial\phi_1}{\partial x} + \frac{\partial\varphi_1}{\partial y_1}\right)\Big|_{y_1=h_1} &= \begin{cases} 0 & ,\quad 0 \le x \le L \\ \left(\frac{\partial\phi_2}{\partial x} + \frac{\partial\varphi_2}{\partial y_2}\right)\Big|_{y_2=-h_2} & ,\quad L \le x \le a \end{cases} \\ \left(\frac{\partial\phi_1}{\partial y_1} - \frac{\partial\varphi_1}{\partial x}\right)\Big|_{y_1=h_1} &= \begin{cases} i\omega\Delta & ,\quad 0 \le x \le L \\ \left(\frac{\partial\phi_2}{\partial y_2} - \frac{\partial\varphi_2}{\partial x}\right)\Big|_{y_2=-h_2} & ,\quad L \le x \le a \end{cases}\end{aligned} \tag{12}$$

At $-h_2 < y_2 < 0$

$$\left(\frac{\partial \phi_2}{\partial x}+\frac{\partial \varphi_2}{\partial y_2}\right)\Bigg|_{y_2=-h_2} = \begin{cases} 0 & , \quad 0 \le x \le L \\ \left(\frac{\partial \phi_1}{\partial x}+\frac{\partial \varphi_1}{\partial y_2}\right)\Big|_{y_1=h_1} & , \quad L \le x \le a \end{cases}$$
$$\left(\frac{\partial \phi_2}{\partial y_2}-\frac{\partial \varphi_2}{\partial x}\right)\Bigg|_{y_2=-h_2} = \begin{cases} i\omega\Delta & , \quad 0 \le x \le L \\ \left(\frac{\partial \phi_1}{\partial y_1}-\frac{\partial \varphi_1}{\partial x}\right)\Big|_{y_1=h_1} & , \quad L \le x \le a \end{cases} \tag{13}$$

Next, we substitute (10) and (11) into (12) and (13), multiplying the equations by sin ($\lambda_i x$) and integrating with respect to *x* along the length of the beam. The equations (12) and (13) become:

$$\begin{aligned} &\frac{a}{2}\beta_m[B_{1m}\sinh(\beta_m h_1)+(\lambda_m/\beta_m)A_{1m}\cosh(\beta_m h_1)]-\frac{a}{2}\lambda_m[A_{1m}\cosh(\lambda_m h_1)+B_{1m}\sinh(\lambda_m h_1)] \\ &=\sum\beta_n\alpha_{mn}[B_{2n}\sinh(-\beta_n h_2)+(\lambda_n/\beta_n)A_{2n}\cosh(-\beta_n h_2)]-\lambda_n\alpha_{mn}[A_{2n}\cosh(-\lambda_n h_2)+B_{2n}\sinh(\lambda_n h_2)] \end{aligned} \tag{14}$$

$$\begin{aligned} &\frac{a}{2}\beta_m[B_{2m}\sinh(-\beta_m h_2)+(\lambda_m/\beta_m)A_{2m}\cosh(-\beta_m h_2)]-\frac{a}{2}\lambda_m[A_{2m}\cosh(-\lambda_m h_2)+B_{2m}\sinh(\lambda_m h_2)] \\ &=\sum\beta_n\alpha_{mn}[B_{1n}\sinh(\beta_n h_1)+(\lambda_n/\beta_n)A_{1n}\cosh(\beta_n h_1)]-\lambda_n\alpha_{mn}[A_{1n}\cosh(\lambda_n h_1)+B_{1n}\sinh(\lambda_n h_1)] \end{aligned} \tag{15}$$

$$\begin{aligned} &\frac{a}{2}\lambda_m[A_{1m}\sinh(\lambda_m h_1)+B_{1m}\cosh(\lambda_m h_1)]-\frac{a}{2}\lambda_m[B_{1m}\cosh(\beta_m h_1)+(\lambda_m/\beta_m)A_{1m}\sinh(\beta_m h_1)] \\ &=\sum i\omega S_n\psi_{mn}+\sum\lambda_n\gamma_{mn}[A_{2n}\sinh(-\lambda_n h_2)+B_{2n}\cosh(-\lambda_n h_2)]-\lambda_n\gamma_{mn}[B_{2n}\cosh(-\beta_n h_2)+(\lambda_n/\beta_n)A_{2n}\sinh(-\beta_n h_2)] \end{aligned} \tag{16}$$

$$\begin{aligned} &\frac{a}{2}\lambda_m[A_{2m}\sinh(-\lambda_m h_2)+B_{2m}\cosh(-\lambda_m h_2)]-\frac{a}{2}\lambda_m[B_{2m}\cosh(-\beta_m h_2)+(\lambda_m/\beta_m)A_{2m}\sinh(-\beta_m h_2)] \\ &=\sum i\omega S_n\psi_{mn}+\sum\lambda_n\gamma_{mn}[A_{1n}\sinh(\lambda_n h_1)+B_{1n}\cosh(\lambda_n h_1)]-\lambda_n\gamma_{mn}[B_{1n}\cosh(\beta_n h_1)+(\lambda_n/\beta_n)A_{1n}\sinh(\beta_n h_1)] \end{aligned} \tag{17}$$

where $\alpha_{nm}=\int_L^a \sin(\lambda_n x)\sin(\lambda_m x)dx$, $\gamma_{nm}=\int_L^a \cos(\lambda_n x)\cos(\lambda_m x)dx$, $\psi_{nm}=\int_0^L \xi_n\cos(\lambda_m x)dx$. Recall that the governing equation for the vibration of a cantilever is given by Eq. (1). Coupling the viscous stress from liquid and the vibration of the microcantilever beam, the following equations was obtained:

$$
\begin{aligned}
&S_m[EI\int_0^L \xi_m(x)\frac{d^4\xi_m(x)}{dx^4}dx - m\omega^2\int_0^L {\xi_m}^2(x)dx - N\int_0^L \xi_m(x)\frac{d^2\xi_m(x)}{dx^2}dx] \\
&= b\sum\left\{(i\omega\rho + 2\mu\lambda_n^2)\psi_{mn}[A_{1n}\cosh(\lambda_n h_1) + B_{1n}\sinh(\lambda_n h_1)] - 2\mu\lambda_n\beta_n\psi_{mn}[B_{1n}\sinh(\beta_n h_1) + (\lambda_n/\beta_n)A_{1n}\cosh(\beta_n h_1)]\right\} \\
&- b\sum\left\{(i\omega\rho + 2\mu\lambda_n^2)\psi_{mn}[A_{2n}\cosh(-\lambda_n h_2) + B_{2n}\sinh(-\lambda_n h_2)] - 2\mu\lambda_n\beta_n\psi_{mn}[B_{2n}\sinh(-\beta_n h_2) + (\lambda_n/\beta_n)A_{2n}\cosh(-\beta_n h_2)]\right\} \\
&+ G_m\int_0^l \xi_m(x)dx
\end{aligned}
\tag{18}
$$

Given the modal shapes ξ_m obtained from Eq. (3), linear equations (14), (15), (16), (17) and (18) for S_m, A_{1m}, B_{1m}, A_{2m}, and B_{2m} form a linear system, which were subsequently solved to describe the dynamic behavior of the microcantilever immersed in the viscous liquid.

3.3 Results and Discussion

First, the model is validated with experimental data from a cantilever-based affinity glucose sensor and a microrheological sensor. Both sensors feature a microcantilever vibrating in confined aqueous environment but are operating at different order of excitation frequency.

The affinity glucose sensor uses a rectangular SU-8 microcantilever (E = 4 GPa, ρ = 1200 kg/m^3) immersed in glucose-diffused polymer solutions with varying viscosities [71]. The beam dimensions are $L \times b \times t$ = 600 × 500 × 20 μm. The viscosities range from 8.72 to 43.4 cP, and the solution has a comparable density to SU-8, which is 1200 kg/m^3.

As parameters of surface stress N and height h_1 and h_2 are difficult to precisely determined, these parameters are obtained by fitting the model to the experimental data of the affinity glucose sensor. Least square fits allowed estimates of these parameters to be N = 0.076 N/m, h_1 = 255 μm and h_2 = 110 μm. These estimates are consistent with practical values as the surface stress N of a

microcantilever is in the range of 0.001-0.1 N/m reported for a SU-8 polymeric cantilever with a similar geometry while h_1 and h_2 are within 10% deviation from their designed values. The experimental data at two concentrations (0 mM and 25 mM) were used for validation, which represent the range of glucose levels in mesurements. In experiments, the output voltage decreases from 0.36V to 0.21V for 25mM and from 0.34V to 0.15V for 0 mM as the frequency is varied from 0 to 1000 Hz. Figure 3-2 shows a least square fit of the model to experimental data, in which the output voltage estimated from the model has a normalized mean square error (NMSE) of 0.0031 for 0 mM concentration of glucose and a NMSE of 0.0016 for 25mM glucose concentration.

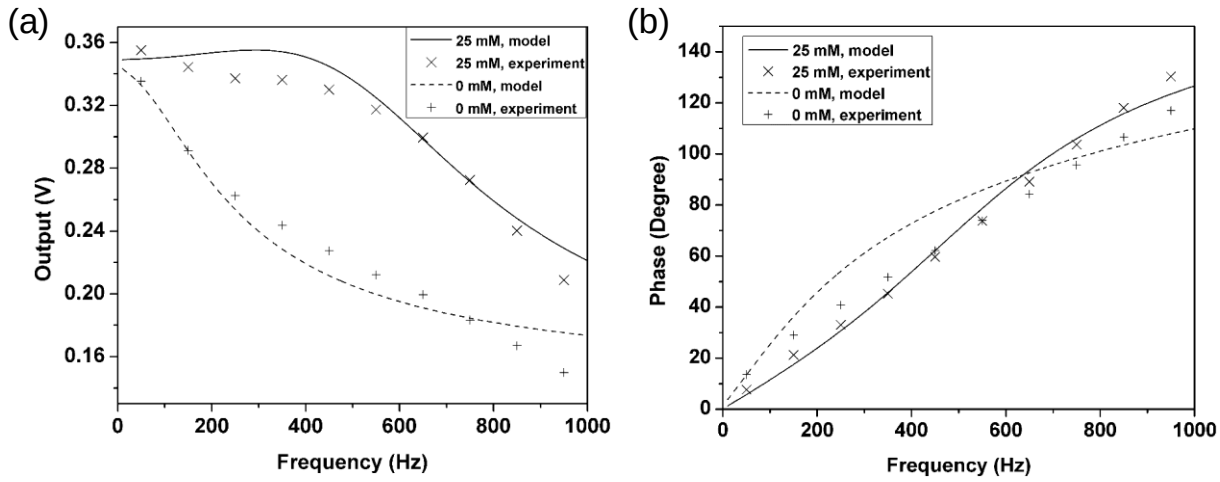

Figure 3–2: The model fitted to the output of an affinity glucosnewe sensor with a microcantilever immersed in 0 and 25 mM glucose solution.

In addition to the affinity glucose sensor, the model is applied to the prediction of resonant behavior of a microrheological sensor. The cantilever array was immersed in the water and different concentrations of glycerol considered as Newtonian fluids when the resonant frequency

of the cantilever was measured [72]. Each cantilever (E = 169 GPa, ρ = 2328 kg/m^3) has a thickness of 1 μm, a length of 500 μm and a width of 100 μm with a 5-μm separation from the top and from the bottom. The cantilevers are vibrating at a mode number of n = 10, in still water, 20%-, 30%- and 40%- glycerol, respectively. Here, define the dimensionless complex amplitude $\bar{A} = \Delta \cdot m\omega_{vac}^2/G$, where ω_{vac} is the resonant frequency of the beam in vacuum. This dimensionless parameter will reflect the complex response of the cantilever beam in a viscous liquid in comparison to its response in vacuum under the same excitation, which can be plotted as a function of ω/ω_{vac} (Figure 3-3). When comparing the resonant frequencies extracted from Figure 3-3 and experimental data [72], the errors are found to be <1.6% for various concentrations of glycerol (1-3.5 cP) and <0.9% for water. This is satisfactory as it is known that the material properties are commonly process dependent and may significantly deviate from their nominal values, and that geometric dimensions of the sensors may also deviate from the design values due to imperfections in fabrication. This confirms that our model provides a valid quantitative description of the microcantilever sensor vibrating in viscous liquids.

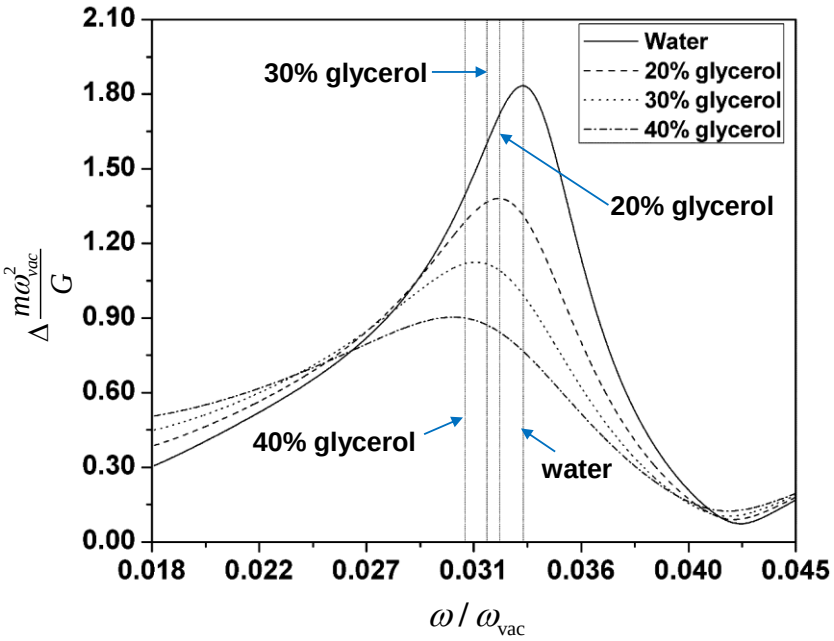

Figure 3–3: Comparison of model-predicted resonant frequency for a microrheological sensor at a high mode (n=10) to experimental measurements of resonant frequency for the microrheological sensor. The vertical lines indicate experimental measurements of the resonant frequencies of cantilever in different solutions. The curves are model-predicted frequency responses.

The parametrized model allows us to systematically study the effects of the parameters, including the depth (h_1 and h_2), the length (a and l) and the surface stress (N). We first define a normalized Reynolds number that is $\overline{\mathrm{Re}} = \rho_f \omega_n t b / \mu$, where ρ_f is the density of surrounding fluid, t is the thickness of the cantilever, and b is its width. Under a given $\overline{\mathrm{Re}}$, the dimensionless amplitude is subsequently evaluated by solving equations (14)-(17) and (18), with $h_1/(h_1+h_2)$ and a/l varied from 0.16 to 0.33 and from 1.95 to 2.1, respectively, which represents the affinity glucose sensor.

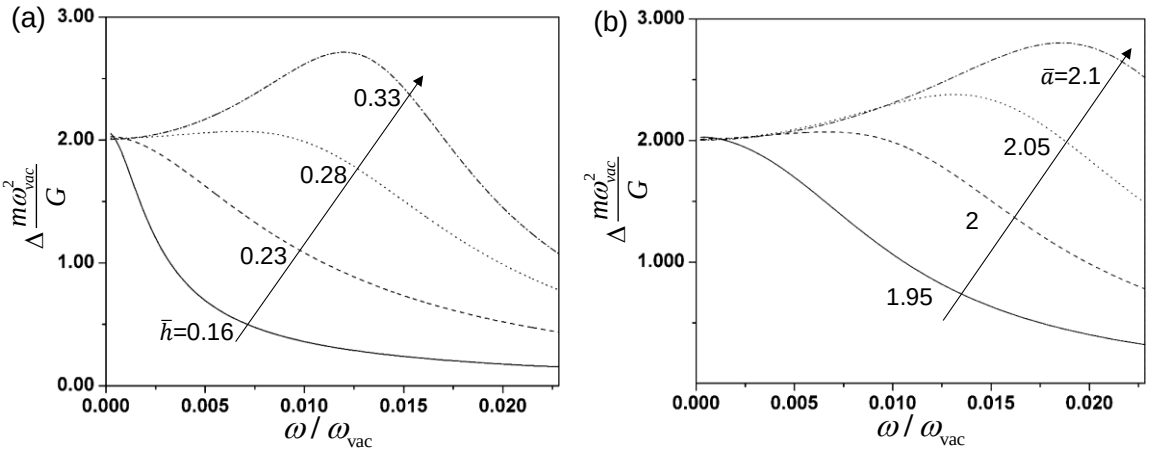

Figure 3–4: Geometric effect on the dynamic response of the cantilever. (a) Varying the dimensionless height $\bar{h}= h_1/(h_1+h_2)$. (b) Varying the dimensionless length ($\bar{a}$=a/l). $\overline{\mathrm{Re}}$=22.5.

Figure 3-4 depicts the dependence of the complex amplitude $\bar{A} = \Delta m\omega_{vac}^2/G$ on the excitation frequency ω/ω_{vac}. The excitation frequency at which $\bar{A}$ achieves its peak value steadily increase as $\bar{h}$ increases from 0.2 to 0.5. At a relatively small $\bar{h}$ value, the amplitude $\bar{A}$ monotonically decreases while the amplitude initially increases and then decreases with ω/ω_{vac} at higher $\bar{h}$ as a direct result of the increasing importance of viscous effects in the liquid. Furthermore, we note that the complex amplitude increases with the dimensionless length of the geometry at a higher frequency ω/ω_{vac} >= 0.01 when fixing $\bar{h}$ = 0.28. This is primarily due to the decrease in dissipative effects in the liquid as the cantilever move away from the surface. These results suggest that increasing the separation between the cantilever and the boundary of liquid chamber could potentially enlarge the Q-factor of the vibrating cantilever.

Another significant factor to affect the frequency characteristics will be the surface stress of the cantilever beam. The surface stress is often changed when biochemical reactions, e.g., affinity

binding, happen on the cantilever beam. The added mass of the binding layer can be neglected because the surface stress induced change dominates the shift of the cantilever resonant frequency [73]. Using the model, we study the response of the cantilever in a bounded liquid with various surface stress that is consistent with recent experimental results [74]. When the dimensionless tensile stress $\bar{N}$ increase from 0.0021 to 0.0063, we note that there is a left shift in the resonant frequency. This is consistent with previous reports [75] that the influence of the surface stress for a free cantilever that increasing tensile surface stress will decrease the microcantilever resonant frequencies. It is observed that the dynamical response varies monotonically with the surface stress at the excitation frequencies that are below the resonant frequencies. This implies that at lower frequencies the sensor performance could be optimized when measuring the surface stress.

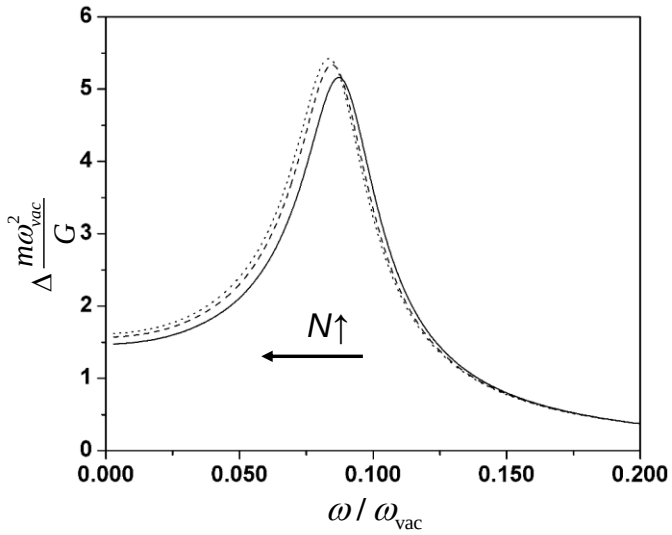

Figure 3–5: Shift in resonant frequency when varying the surface stress $\bar{N} = NL^3 / EI$ of the cantilever. $\overline{\text{Re}}$=22.5.

Next, the model was applied to study the thermal noise spectra of the microcantilever in a bounded viscous liquid. Assume the liquid that the microcantilever is immersed in is kept at temperature *T*. At thermal equilibrium, the fluid molecules interact with the microcantilever and excite it thermally. Such fluctuating force is stochastic in nature and maintains a mean-squared response according to the equipartition theorem [76]. As the equipartition theorem indicates, each vibration mode has a mean thermal energy of k_BT (1/2 k_BT for the potential energy and 1/2 k_BT for the kinetic energy). For the potential energy, let $\frac{1}{2}k_BT = \frac{1}{2}k\left\langle w(x,t)^2 \right\rangle$ and we will obtain the expected value of $w_n(x,t)^2$ that $\left\langle w_n(x,t)^2 \right\rangle = \frac{k_BT}{m\omega_n^2}$. This indicates that the thermal noise depends only on the temperature and the properties of the cantilever. We express the hydrodynamic force on the cantilever in the form of $F_h = m_f\omega^2\Gamma(\omega)w_n(x|\omega)$ [55] where $m_f = \rho_f b^2$ and $\Gamma(\omega) = \Gamma_r(\omega) + i\Gamma_i(\omega)$ is a complex hydrodynamic function that can be evaluated by the model. Following this, the equation of the vibration of the microcantilever at mode *n* in the frequency domain can be described as:

$$EI\frac{d^4w_n(x|\omega)}{dx^4} - N\frac{d^2w_n(x|\omega)}{dx^2} - m\omega^2w_n(x|\omega) + m_f\omega^2\Gamma(\omega)w_n(x|\omega) = F_{ext} \tag{19}$$

where F_{ext} is a stochastic external force induced by the Brownian motion of fluid molecules. Solving the equation above gives:

$$w_n(x|\omega) = \frac{F_{ext}}{m\omega_n^2 - m\omega^2 + m_f\Gamma_r(\omega)\omega^2 + im_f\Gamma_i(\omega)\omega^2} \tag{20}$$

where ω is the excitation frequency and ω_n is the natural frequency of mode *n*. Due to the orthogonality of the vibration modes

$$\left|w(x|\omega)\right|^2 = \sum \frac{{F_{ext}}^2}{[m{\omega_n}^2 - m\omega^2 + m_f\Gamma_r(\omega)\omega^2]^2 + [m_f\Gamma_i(\omega)\omega^2]^2} \tag{21}$$

Then, the power spectral density of the deflection can be expressed with $|w(x|\omega)|^2$, which is:

$$S_{ww}(\omega) = \lim_{t\to\infty}\frac{1}{t}\left|w(x|\omega)\right|^2 = \sum \lim_{t\to\infty}\frac{1}{t}\frac{{F_{ext}}^2}{[m{\omega_n}^2 - m\omega^2 + m_f\Gamma_r(\omega)\omega^2]^2 + [m_f\Gamma_i(\omega)\omega^2]^2} \tag{22}$$

Note that $\left\langle w(x,t)^2\right\rangle = \lim_{t\to\infty}\frac{1}{t}\int_{-t/2}^{t/2}\left|w(x,t)\right|^2 dt = \lim_{t\to\infty}\frac{1}{2\pi t}\int_{-\infty}^{\infty}\left|w(x|\omega)\right|^2 d\omega = \frac{1}{\pi}\int_0^{\infty} S_{ww}(\omega)d\omega$. Substitute Eq. (22) into the expression and let $\lim_{t\to\infty}\frac{{F_{ext}}^2}{t} = F_0$, this leads to:

$$\left\langle w(x,t)^2\right\rangle = \sum \frac{F_0}{\pi}\int_0^{\infty}\frac{1}{[m{\omega_n}^2 - m\omega^2 + m_f\Gamma_r(\omega)\omega^2]^2 + [m_f\Gamma_i(\omega)\omega^2]^2}d\omega \tag{23}$$

Equating $\left\langle w_n(x,t)^2\right\rangle$ with $\frac{k_BT}{m{\omega_n}^2}$, we obtain:

$$F_0 = \frac{\pi k_BT}{m{\omega_n}^2\int_0^{\infty}\frac{1}{[m{\omega_n}^2 - m\omega^2 + m_f\Gamma_r(\omega)\omega^2]^2 + [m_f\Gamma_i(\omega)\omega^2]^2}d\omega} \tag{24}$$

$$S_{ww}(\omega) = \sum \frac{\pi k_BT}{m{\omega_n}^2\{[m{\omega_n}^2 - m\omega^2 + m_f\Gamma_r(\omega)\omega^2]^2 + [m_f\Gamma_i(\omega)\omega^2]^2\}\int_0^{\infty}\frac{1}{[m{\omega_n}^2 - m\omega'^2 + m_f\Gamma_r(\omega')\omega'^2]^2 + [m_f\Gamma_i(\omega')\omega'^2]^2}d\omega'} \tag{25}$$

With Eq. (25), the dimensionless power spectral density $\bar{S}_{ww} = S_{ww}\frac{m{\omega_n}^2}{2\pi k_BT}$ can be evaluated. In Figure 3-6, we present the frequency dependence of the normalized thermal spectral density, which indicates the distribution of the mean power of the thermally excited vibration into the frequency domain. The normalized Reynolds number $\overline{\mathrm{Re}} = \rho_f\omega_n tb/\mu$ is set as a value between 10 and 40, corresponding to practical values for microcantilever beams immersed in fluid [77]. It is evident from Figure 3-6 that increasing $\bar{A}$ shifts the peak to higher frequencies for given value of geometric and material properties, which is primarily due to an increase in inertial forces from the

liquid medium. We also note that the peak energy for $\overline{\mathrm{Re}}$ = 10 is greater than the peak energy for $\overline{\mathrm{Re}}$ = 20, and the latter is smaller than the peak value for $\overline{\mathrm{Re}}$ = 30. We suspect the cause is that, when the viscous dissipation is small, the thermal energy is distributed over a larger frequency range while the energy is redistributed towards lower frequencies if dissipative effects in the liquid are significant.

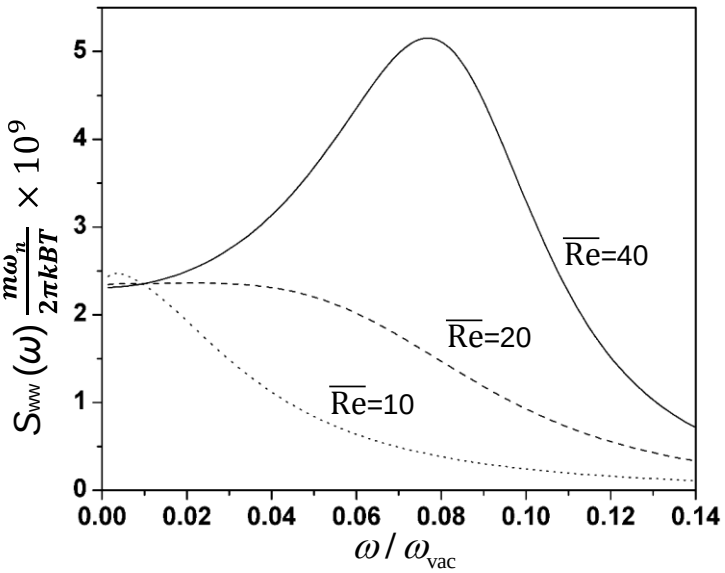

Figure 3–6: Frequency dependency of the spectral density of the cantilever deflection when varying the normalized Reynolds number.

3.4 Conclusions

This chapter presents a biomicrofluidic analysis for cantilever-based MEMS glucose sensors. The sensors are based on the harmonic vibration of cantilevers, involving disturbance from the motion of viscous fluid around the cantilevers. To simulate the response of cantilever-based sensors, we have solved time-dependent stokes equations with Euler-Bernoulli beam equation. The

fluid-structure coupling has been achieved via satisfying the kinematic and dynamic boundary condition at the liquid-cantilever interface. We have also compared simulation results to experimental results using nominal design parameters. Reasonable agreement between the experimental data and simulation results verified the presented methodology for predicting the dynamic response of the sensor has sufficient accuracy. Additionally, we present a thorough parametric study for the sensor to optimize the performance of the cantilever sensor, which calculates the dynamic response from the design parameters, such as the physical properties of the liquid medium, the dimensionless distance between cantilever and the boundary of liquid chamber, and the surface stress of the cantilever. By analytical and numerical analysis with our formulation, we have obtained the optimal design and operation parameters. Finally, we have evaluated the thermal response of the cantilever sensor in detail, considering the importance of recognizing thermal noise in the precise measurements for miniature devices. It is found that the thermal noise does not change monotonically with Reynolds number and its variation is strongly dependent on the intensity of viscous dissipation, which we believe will be of significant practical value to precise measurements.

Chapter 4. Exploring Dielectric Glucose Sensing: Surface-Immobilized Hydrogels

While vibrational glucose sensors require mechanical movable structures that would pose miniaturization challenges and give rise to reliability and robustness issues, measurements of glucose-dependent dielectric properties would be an attractive solution to address the issues found in vibrational devices and fully realize the affinity sensing [26] [28]. This chapter further explores a hydrogel-based glucose sensor with dielectric measurements, which uses a synthetic hydrogel immobilized on the device surface. The use of hydrogels with dielectric measurements eliminate mechanical moving parts in viscometric glucose microsensors, as well as mechanical barriers such as semipermeable membranes that are otherwise required to hold the glucose-sensitive material.

4.1 Introduction

Continuous glucose monitoring (CGM), which involves highly frequent and repetitive measurements of glucose, can detect abnormal glucose concentrations in diabetes patients in a timely manner. Existing CGM devices often rely on electrochemical detection of enzymatic reactions [17, 78, 79]. While commonly used for glucose sensing, these devices are typically hindered by large drift and insufficient accuracy because of the irreversible, consumptive nature of electrochemical reactions. Affinity sensors, which are based on non-reactive equilibrium binding of glucose with a specific receptor [80, 81], can potentially overcome these limitations. Affinity glucose sensing can be implemented in microsensors, which have used measurements of affinity binding-induced changes in physical properties such as volume[82, 83], viscosity[29, 46] , fluorescence[84, 85] and electric conductivity[86]. However, these efforts have required the use

of a semi-permeable membrane as a physical barrier or mechanically movable structures, which can increase the complexity and limit the reliability of the devices. In contrast, affinity dielectric sensors that detect the glucose-dependent dielectric properties can effectively address these limitations.

Affinity sensors that are based on dielectric measurements have been used in applications such as detecting or quantifying biochemical targets under excitations at various frequencies. Example of these applications include determination of protein concentration [87, 88], detection of DNA[89, 90], and monitoring of bacteria [91, 92]. Affinity glucose microsensors utilizing dielectric measurements have however not been widely explored. We have previously reported measurements of the permittivity of a polymer solution as the polymer binds to glucose microsensors [28, 93, 94]. While demonstrating the potential in sensitive and selective detection of the glucose through dielectric measurements both in vitro and in vivo, the polymer solution required sealing using a semi-permeable membrane that significantly increased the complexity, limited the level of miniaturization, and affected the reliability of the microsensor.

This paper presents an affinity microsensor that measures glucose concentrations via the dielectric response of a hydrogel embedded in a capacitive transducer. The microsensor is fabricated using microelectromechanical systems (MEMS) technology, and the hydrogel is synthetically prepared, non-toxic and polymerized in situ in the device. Reversible affinity binding of glucose with boronic acid groups in the hydrogel changes the dielectric properties of the hydrogel, which can be measured using a MEMS capacitive transducer to determine the glucose concentration. The design of the microsensor eliminates the use of mechanical moving parts found in other types of affinity microsensors that are not amenable to miniaturization [83, 95]. The hydrogel is directly immobilized onto the surface of the transducer and will be stable over time,

allowing the device to eliminate the use of a semipermeable membrane that are otherwise required to hold the glucose-sensitive material [28], and potentially offer improved tolerance to biofouling during implanted operation. Experimental results demonstrate that in a glucose concentration range of 0-500 mg/dL and with a resolution of 0.35 mg/dL or better, the hydrogel-based microsensor is capable of measuring glucose in a repeatable and reversible manner, and holds promise to enable CGM in a stable, accurate and rapid manner.

4.2 Principle and Design

The affinity glucose microsensor utilizes a synthetic glucose-sensitive hydrogel, which consists of N-3-acrylamidophenylboronic acid (AAPBA) as the glucose-sensing component, and acryl N-Hydroxyethyl acrylamide (HEAA) as the hydrophilic component. The hydrogel uses tetraethyleneglycol diacrylate (TEGDA) as the cross-linker and 2,2'-Azobis (2-methylpropionamidine) dihydrochloride (AAPH) as the polymerization initiator. When glucose binds reversibly to the phenylboronic acid moieties in the AAPBA segments to form strong cyclic boronate ester bonds, a change in the dielectric properties of the hydrogel occurs and can be measured to determine the glucose concentration.

The dielectric properties of the hydrogel can be represented by the complex permittivity: $\varepsilon^* = \varepsilon' - i\varepsilon''$, where the real permittivity ε' represents the ability of the hydrogel to store electric energy, while the imaginary permittivity ε'' is related to dissipation of energy. When the gap between the electrodes of a parallel-plate transducer is filled with the hydrogel (Figure 4-1), the transducer can be represented by a capacitor (effective capacitance: C_x) and resistor (effective resistance: R_x) connected in series. Correspondingly, the real and imaginary parts of the complex permittivity are related to these parameters by $\varepsilon' = C_x/C_0$ and $\varepsilon'' = 1/(\omega R_x C_0)$, where C_0 is the

capacitance when the electrode gap is in vacuum. The interactions of the hydrogel with glucose in general cause changes in its composition and conformation, and hence changes in its dielectric properties ε′ and ε″. Thus, the transducer's effective capacitance and resistance will hence change and can be measured to determine the glucose concentration.

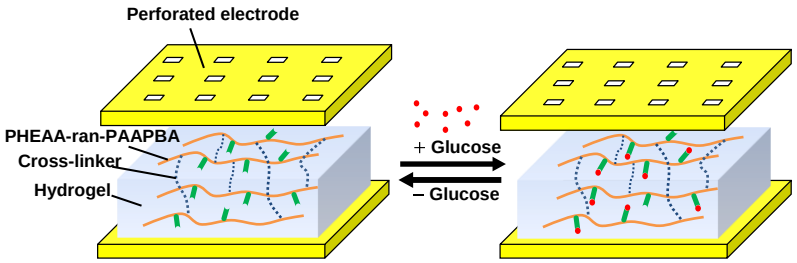

Figure 4–1: Principle of hydrogel-based microsensor.

The transducer is enabled by MEMS technology and uses a pair of parallel electrodes sandwiching the hydrogel (Figure 4-2). The upper electrode is perforated to allow passage of glucose molecules and is passivated within a perforated diaphragm to avoid direct contact with the hydrogel. The perforated electrode and diaphragm are supported by microposts so that they do not collapse onto the lower electrode on the substrate. Glucose molecules reversibly bind with the hydrogel, thereby changing the hydrogel's complex permittivity. While changes in the real and imaginary parts of the complex permittivity can be used to determine the glucose concentration, we in the present work focus on the real permittivity, which can be interrogated via measurement of the capacitance between the electrodes, to determine the glucose concentration.

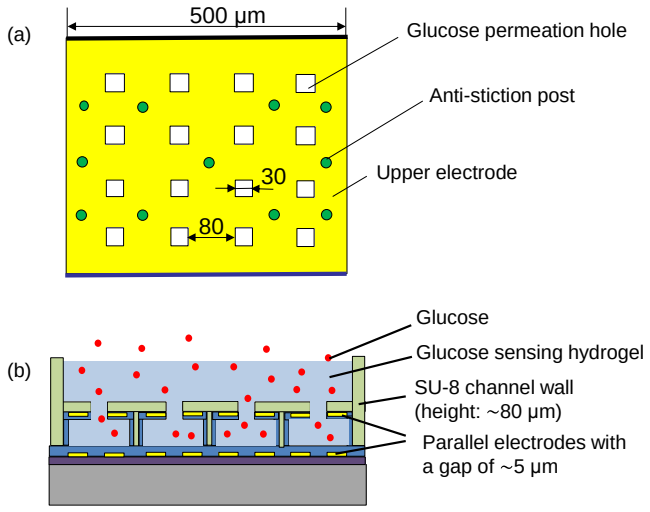

Figure 4–2: Schematics of the affinity microsensor: (a) top view and (b) side view.

Fabrication

To fabricate the MEMS capacitive transducer, a chrome (Cr)/gold (Au) film (5/100 nm) was deposited by thermal evaporation and patterned to form the lower electrode (500 µm×500 µm) on a SiO2–coated wafer. The patterned gold electrode was then passivated with Parylene (1 µm). This was, followed by deposition of an S1818 sacrificial layer (5 µm) and an additional Parylene layer (1.5 µm). Another Cr/Au (5/100 nm) film was patterned to form the upper electrode and passivated by another Parylene layer. An SU-8 layer was then patterned to form a channel and anti-collapse microposts between the electrodes. The Parylene diaphragm was patterned with reactive ion etching (RIE) to form perforation holes that allow glucose permeation. The sacrificial photoresist layer was removed with acetone to release the diaphragm. The device fabrication process is shown in Figure 4-3(a).

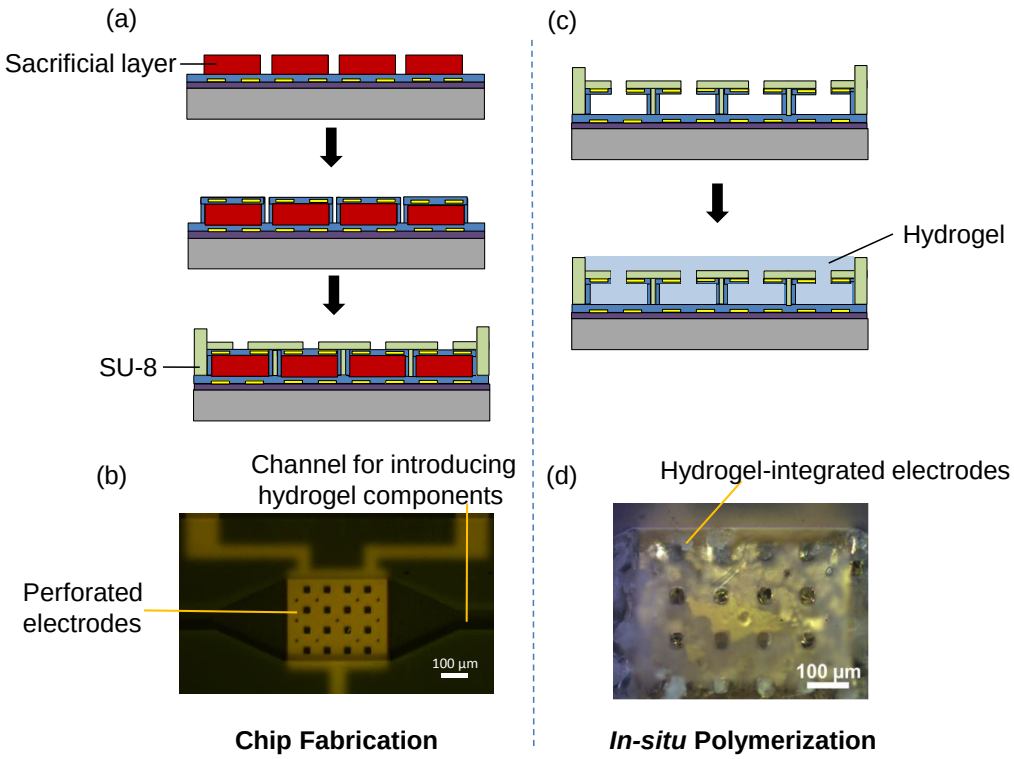

Figure 4–3: Chip fabrication: (a) standard fabrication procedures and (b) image of a fabricated capacitive transducer. In situ polymerization: (c) hydrogel integration in the transducer and (d) image of the hydrogel-integrated device.

The hydrogel was prepared in situ in the capacitive transducer. First, a mixture of the hydrogel components (AAPBA, HEAA, TEGDA, and AAPH) in solution was deoxygenated by nitrogen gas for 30 minutes, and was then injected into the device, filling the gap between the parallel electrodes. The device was placed in a nitrogen environment and heated for 4 hours at 70°C. The hydrogel was formed between the parallel electrodes, as shown in Figure 4-3(d). The hydrogel-integrated device was rinsed with water and ethanol to remove unreacted monomer and reagents.

Materials

The hydrogel was synthesized in house via free radical polymerization with AAPBA and

HEAA monomers. An HEAA to AAPBA molar ratio of 9 (or approximately 10% AAPBA in all the monomers) was adopted. Then a solution consisting of AAPBA (1.1% w/v), HEAA (5.5% v/v), TEGDA (0.08% v/v), and AAPH (0.16% w/v) in distilled water was prepared for polymerization. A stock solution (0.1 M) of glucose was prepared by dissolving D-(+)-glucose (0.9 g) in distilled water to 50 mL. Glucose solution at varying concentrations (40, 70, 90, 180, 300, and 500 mg/dL) was prepared by diluting the stock solution.

Experimental Setup

During testing, we placed the device in an acrylic test cell (2 mL in volume) filled with glucose solution (Figure 4-4). The device was connected to a capacitance/voltage transformation circuit driven by a sinusoidal input from a function generator (Agilent, 33220A), which imposes an AC electric field on the electrodes of the device to induce a glucose concentration-dependent change in the permittivity of the hydrogel. The resulting changes in the effective capacitance C_x of the capacitance/voltage transformation circuit are determined by measuring the output voltage (U_{out}) from a given input AC voltage (U_{in}). All experiments were conducted at frequencies in a range of 1 to 100 kHz as allowed by a lock-in amplifier (Stanford Research Systems, SR844) used in output voltage measurements.

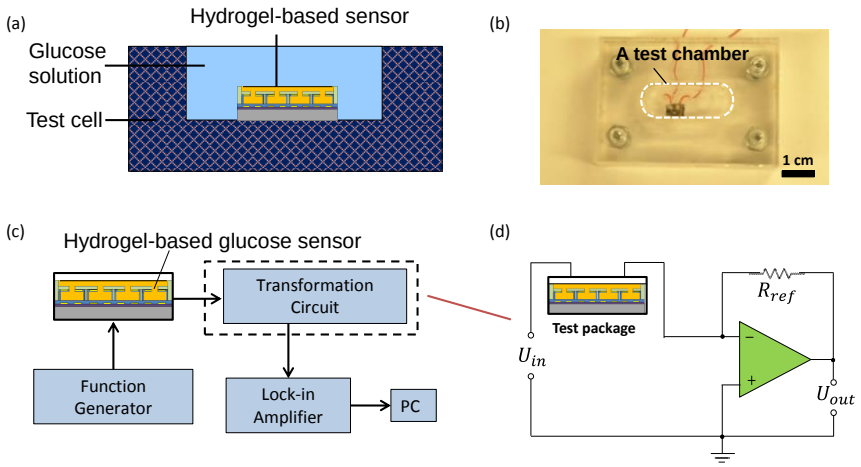

Figure 4–4**:** Experimental setup: (a) Schematics of a testing setup. (b) Image of the testing setup. (c) Experimental setup. (d) A capacitance/voltage transformation circuit.

4.3 Results and Discussion

We first investigated the microsensor response to different glucose concentrations under bias voltages of different frequencies (Figure 4-5). First, we observed that, at each of a series of physiologically relevant glucose concentrations (0-500 mg/dL), the effective capacitance of the device, and hence the permittivity of the hydrogel, decreased with increasing frequency over the entire frequency range tested (1-100 kHz) (Figure 4-5a). This is consistent with the dielectric relaxation of the hydrogel, in which the dielectric properties of the hydrogel have a momentary delay with respect to a changing electric field [96]. The dielectric properties of the hydrogel in an electric field are in general influenced by a number of mechanisms of polarization (i.e., shift of electric charges from their equilibrium positions under the influence of an electric field[97]), such as electronic polarization, ionic polarization, dipolar polarization, counterion polarization, and interfacial polarization. Electronic polarization and ionic polarization involve the distortion of electron clouds with nucleus and the stretching of atomic bonds, while counterion polarization and dipolar polarization reflect redistribution of ions and reorientation of electrical dipoles [98, 99].

At a given frequency, the effective capacitance of the hydrogel increased consistently with glucose concentration in the entire range tested (0-500 mg/dL). This is clear from the device's frequency response (Figure 4-5a), and can be more conveniently examined when the device's response is plotted versus the glucose concentration (Figure 4-5b). For example, at 30 kHz, the effective capacitance increased from 16.2 pF to 24.8 pF as the glucose concentration increased from 0 mg/dL to 500 mg/dL. This reflected that the binding between the hydrogel and glucose significantly influences the polarization of the hydrogel, which may include changes in the hydrogel's structural conformations, permanent dipole moments, elastic resistance to the dipole rearrangement in the electric field, and electric double layer characteristics. These effects, which are highly complex and require elucidation through further in-depth studies, combine to result in the glucose concentration dependence of the hydrogel's dielectric properties, explaining the observed variation of the device's effective capacitance with glucose concentration.

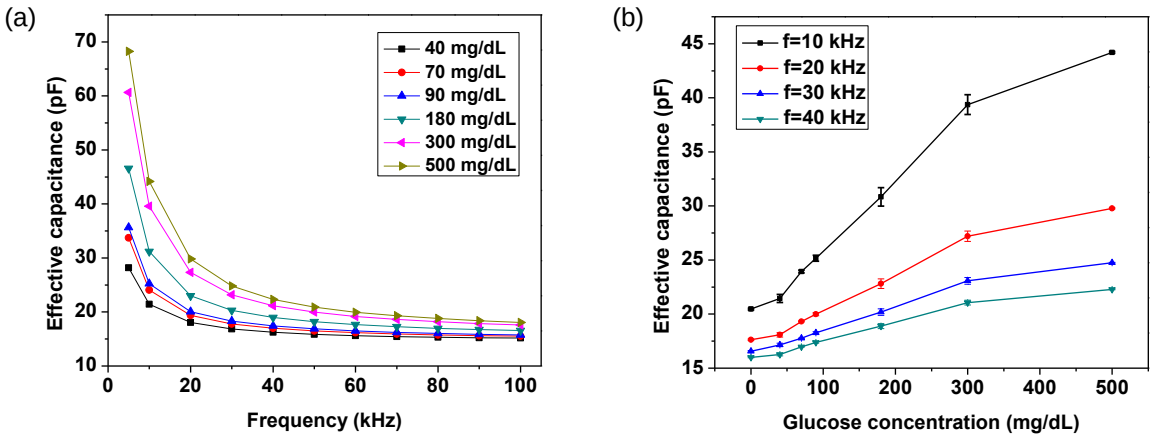

Figure 4–5: Measurement of glucose concentration using the microsensor: Dependence of the effective capacitance on (a) measurement frequency, and (b) glucose concentration. (Effective capacitance values are averages of triplicate measurements, and standard errors are shown as error in (b).)

It can be seen from Figure 4.5b that the dependence of the effective capacitance on glucose concentration is in general nonlinear over the full glucose concentration range tested (0-500 mg/dL). Thus, in practical applications, a calibration curve represented by a lookup chart or nonlinear equation[100] can be used to determine the glucose concentration from a measured effective capacitance value. In moderately smaller glucose concentration ranges, however, this relationship became more linear. For example, the effective capacitance was approximately linear with glucose concentration from 40-300 mg/dL (R^2=0.993), a range that is most relevant to continuous glucose monitoring needs. In this range, a calibrated linear equation may hence be adequate for the determination of glucose concentration from measurement results.

We conducted the above-mentioned experiments in triplicates to examine the ability of the microsensor to measure glucose concentrations in a repeatable manner and with adequate sensitivity (Figure 4-5b). At all glucose concentrations, the standard error in the effective capacitance was less than 0.91 pF (2.3%), indicating excellent repeatability. In addition, at all of the measurement frequencies used, the resolution and range of glucose measurement resolution were found to be appropriate for continuous glucose monitoring. Considering 30 kHz for example, the sensitivity of the microsensor was approximately 15 fF$(mg/dL)^{-1}$ in the glucose concentration range of 0-40 mg/dL. With a capacitance measurement resolution of 3 fF as allowed by our measurement setup, the device's resolution for glucose concentration measurement was correspondingly estimated to be 0.2 mg/dL. At a signal-to-noise ratio of 3, this yielded a detection limit of 0.6 mg/dL, well below the physiologically relevant glucose concentration range (typically greater than 40 mg/dL[101]). For glucose concentrations within 40-300 mg/dL, the sensitivity was approximately 23 fF$(mg/dL)^{-1}$, corresponding to an estimated resolution of 0.12 mg/dL. At higher glucose concentrations (300-500 mg/dL), the nonlinear sensor response experienced a gradual

declination in sensitivity and resolution (respectively to 8.4 fF(mg/dL)$^{-1}$ and 0.35 mg/dL at 500 mg/dL) as an increasingly small number of binding sites remained available in the hydrogel. These sensor characteristics, appropriate for practical applications, are comparable to those of commercially available electrochemical sensors (e.g., 1 mg/dL over a glucose concentration range from 0 to 400 mg/dL [102, 103] or 500 mg/dL [104]) as well as other research-stage boronic acid-based affinity sensors (e.g., 0.3 mg/dL[105] over a range from 0 to 300 mg/dL[23] or 540 mg/dL[106]) for continuous glucose monitoring.

We investigated the response of the hydrogel-based microsensor to glucose as compared to its response to potential interferents. Nonspecific molecules exist in interstitial fluid and can interact with boronic acid, which is the glucose sensitive component of our hydrogel. These molecules include fructose (~1.8 mg/dL), galactose (~1.8 mg/dL), lactate (~9 mg/dL), and ascorbic acid (~1.32 mg/dL). We tested the hydrogel-based microsensor on these molecules and found that the resulting response was substantially lower than that to glucose. For example, at the same concentration of 90 mg/dL, the effective capacitance change (measured at 30 kHz) due to fructose, galactose, lactate and ascorbic acid was found to be 17%, 38%, 32% and 28% of that due to glucose, respectively (Figure 4-6a). Here, the effective capacitance change is calculated according to $\Delta C = C\text{-}C_0$ where C is the effective capacitance at a given glucose (or interferent) concentration, and C_0 is the effective capacitance in the absence of glucose and interferents. Considering that the physiological concentrations of the potential interferents were about one order of magnitude lower than that of glucose, the microsensor was determined to be sufficiently selective for measurements of glucose in interstitial fluid for CGM applications.

While boronic acid binds to all diol-containing molecules, the selective response of the microsensor to glucose over the potential interferents could be attributed to the unique binding

behavior between boronic acid and glucose. At a 1:1 ratio, boronic acid in fact binds more strongly to fructose than glucose. However, with a high concentration of boronic acid units (which was the case for our hydrogel), boronic acid can bind with glucose at a 2:1 ratio [107-109]. We exploited this property in previous work and developed solution-phase, viscometrically based affinity microsensors[109, 110]. In this work, we postulate that the existence of 2:1 binding between glucose and boronic acid units played a major role in the microsensor response, by causing additional crosslinking of the hydrogel that could lead to the augmentation of elastic resistance to electric field-induced dipole reorientation. The rather insignificant device response to the potential interferents (fructose, galactose, ascorbic acid and lactate) could, on the other hand, be attributed to a lack of this 2:1 binding mode.

We also studied the role of boronic acid in glucose recognition to gain further insight into the principle and operation of the microsensor. Using hydrogels containing with and without AAPBA content, we obtain the dependence of the effective capacitance on glucose concentration (Figure 4-6b). It can be seen that when using an AAPBA-free hydrogel, the microsensor exhibited negligible changes in the effective capacitance in response to glucose concentration changes. This is in contrast to the strong glucose-induced response of the microsensor when it was equipped with the 10%-AAPBA hydrogel, indicating that boronic acid moieties in the hydrogel were critically responsible for the desired recognition of glucose by the microsensor.

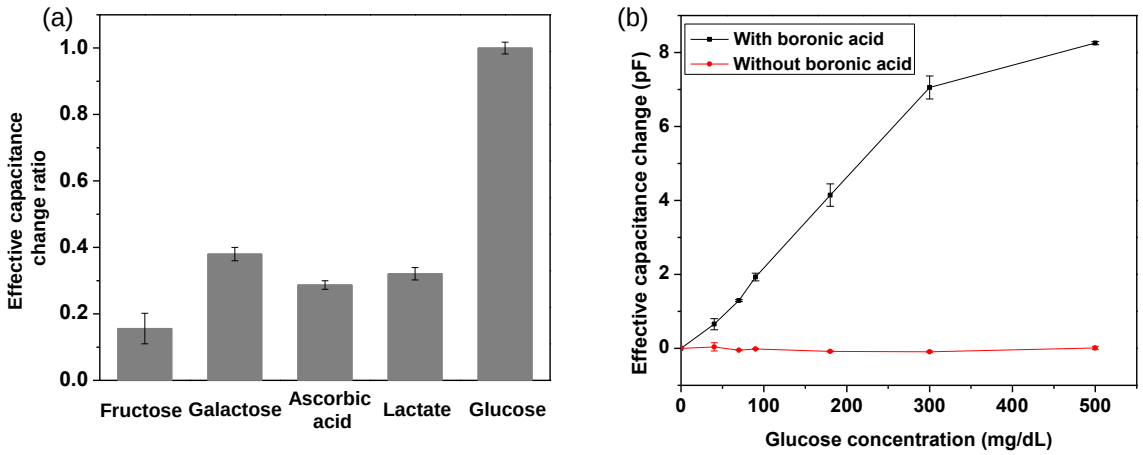

Figure 4–6: (a) Selectivity: ratio of the interferent-induced effective capacitance change to the glucose-induced effective capacitance change (concentration: 90 mg/dL for glucose and each of the interferents including fructose, galactose, ascorbic acid and lactate). The effective capacitance changes were computed with respect to the effective capacitance in the absence of glucose or interferents. (b) Role of boronic acid: microsensor response to glucose when boronic acid components were absent in the hydrogel. (Bias voltage frequency: 30 kHz.)

Finally, we tested the device with time-resolved glucose concentration measurements to assess its ability to track glucose concentration changes in a consistent and reversible manner. The measured microsensor output at 30 kHz varied from 16.5 pF at 0 mg/dL to 24.8 pF at 500 mg/dL (Figure 4-7). In particular, when the device was exposed to a glucose concentration after experiencing another sample that was either higher or lower in concentration, virtually the same effective capacitance value was consistently obtained. For example, the effective capacitance at 40 mg/dL over the two periods (from 20 to 38 minutes, and from 321 to 341 minutes) were respectively 16.87 pF and 16.73 pF, agreeing within 0.8%. Similarly, the reversibility was within 3.4% and 1.3% for the measurement data at glucose concentrations of 180 and 300 mg/dL, respectively. This indicates that because the binding between glucose and boronic acid moieties in the hydrogel, the microsensor possesses excellent reversibility in response to glucose

concentration changes. The time constant of the response (i.e., the time for the sensor to reach 63% of the steady state response) was approximately 16 min. This time constant was attributable to the relatively large thickness of the hydrogel in the proof-of-concept device (~200 μm), through which glucose molecules must diffuse to interact with the capacitive transducer. As the glucose diffusion time decreases with the square of the hydrogel thickness, it is expected that thinner hydrogels can be used to effectively obtain more rapid time responses.

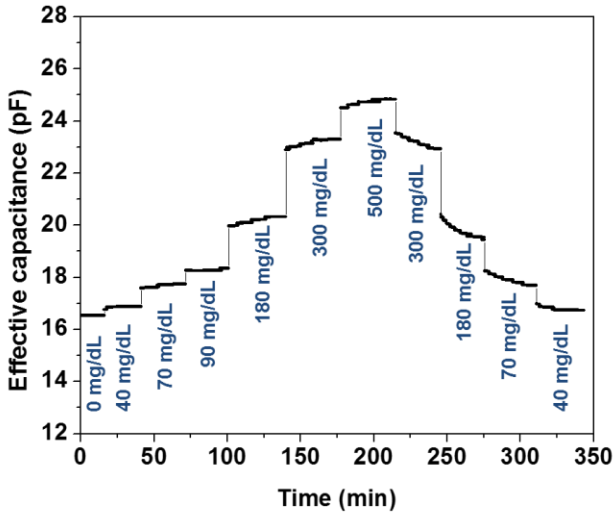

Figure 4–7: Time-resolved device response to time-varying glucose concentration. (Bias voltage frequency: 30 kHz.)

4.4 Conclusions

This chapter presents a hydrogel-based affinity glucose microsensor that measures glucose concentration through dielectric transduction. The device consists of a pair of thin-film parallel capacitive electrodes sandwiching a synthetic hydrogel. Glucose molecules permeate into the hydrogel through electrode perforations, and bind reversibly to boronic acid moieties of the

hydrogel. This induces changes the dielectric polarization behavior, and hence the complex permittivity, of the hydrogel. Thus, the effective capacitance between the electrodes, which is directly related to the real part of the complex permittivity, can be measured to determine the glucose concentration. The use of an in situ polymerized hydrogel simplifies the design of the microsensor, facilitates its miniaturization and robust operation, and can potentially improve the tolerance of the device, when implanted subcutaneously, to biofouling. Testing results showed that the effective capacitance of the device, in a measurement frequency range of 1-100 kHz, responded consistently to glucose concentration changes ranging from 0 to 500 mg/dL. At a given frequency, the effective capacitance increased consistently with glucose concentration, suggesting that the affinity binding between glucose and boronic acid moieties caused the real permittivity of the hydrogel to increase. At 30 kHz, the measurement resolution of the microsensor was estimated to be 0.2, 0.12 and 0.35 mg/dL in the glucose concentration ranges of 0-40, 40-300, and 300-500 mg/dL, respectively. When subjected to time varying glucose concentration changes in the full 0-500 mg/dL range, the microsensor response was consistent and reversible. The time constant of this response was approximately 16 min, which can be readily improved by using thinner hydrogels for reduced glucose diffusion distances. These results have demonstrated that the microsensor can potentially allow accurate and consistent measurement of glucose concentration in interstitial fluid for continuous glucose monitoring.

Chapter 5. Microfluidic Preprocessing for Investigating Single-Cell Gene Expression

This chapter will introduce a microfluidic-integrated preprocessing for single-cell gene expression analysis as a second example of bioanalytical microdevices. This approach incorporates a single-cell capillary picker to introduce single cells into a microfluidic gene-expression preprocessing chip, which allows the tracking of identity of individual cells as well as timely preparation of single cells for analysis post microbeam radiation. The approach was demonstrated with QuantStudio digital PCR by measuring expression levels of the radiation responsive genes in individual control, microbeam-irradiated or bystander IMR90 human lung fibroblasts cells.

5.1 Introduction

Single-cell analysis, which has been extensively used for examining cell heterogeneity, may serve as an important tool for detecting cell-to-cell variation or responses in individual cells. Cell heterogeneity, as manifested by different stages, genetic lesions, or expression programs, is associated with distinct outcomes or therapeutic responses. For example, cells from the same tumor may exhibit distinct phenotypic or epigenetic states, and such intratumoral heterogeneity can cause treatment failure and recurrence of disease [111]. Due to the increasing awareness of analyzing cellular response on a cell-by-cell basis [112-115], methods for single-cell gene expression profiling, which assay gene patterns in individual cells, have been developed to assist in the study of individual cell expression variability and enable characterization of intracellular molecular mechanisms and pathways [116].

Single-cell gene expression analysis has also proved useful for studying the cellular response to ionizing radiation [117]. Ionizing radiation is commonly used as a probe of cellular damage and repair mechanisms. Following ionizing radiation, cells activate biochemical pathways that consist of DNA damage cell-cycle checkpoint pathways and the DNA repair pathways, which promote cell survival while keeping DNA integrity [118]. Diverse cellular activities are engaged in the components of these pathways, such as apoptosis, cell cycle arrest, stress signaling and DNA repair [119]. These responses may be induced by alterations in protein modification or changes in subcellular localization as well as changes in gene expression profiles [120-122]. For their central role in elucidating the mechanisms underlying cellular radiation response, alterations in gene expression have been studied extensively in populations of cells post irradiation [123-125]. While few gene expression studies have covered the cellular response of individual cells to ionizing radiation, gene expression patterns in single irradiated cells have been explored via conventional quantitative RT-PCR [126]. A recent approach of using low-density Taqman real-time PCR has extended the ability of quantitative measurement from 3 genes to 48 genes in one single irradiated cell [117]. An interesting application of single-cell gene expression analysis in radiation studies is exploring the bystander effect, in which non-irradiated cells demonstrate several responses seen in nearby irradiated cells. While this appears to be mediated by signal transmission between irradiated and nearby non-irradiated cells via direct physical contact [127] or through the culture medium [128], the exact nature of the signal and the mechanisms of stress transmission remain to be determined. These bystander mechanisms have implications for the assessment of radiation

risk in situations from low-dose environmental exposures, to particle therapy for cancer, to manned Space missions [129]. The microbeam facility at the Center for Radiological Research is particularly well suited for more definitive study of the bystander effect [130]. While a low dose of particle radiation delivered to a cell population follows a Poisson distribution [126], allowing calculation of the percentage of cells not directly traversed by a particle, the microbeam can deliver a precise number of particles (including one) to a specified cell in the population. Therefore, the microbeam enables irradiation with a precise number of particles to each individual hit cell, while the non-hit single cells are not traversed by a particle.

Following the microbeam irradiation of single cells, microfluidic devices can be used to facilitate handling the preprocessing functions (e.g., cell lysis, RNA purification, etc.) for gene expression measurements. Microfluidic platforms featuring rapid and sensitive biochemical synthesis and analysis that also allow automation, integration and parallelization, have been increasingly used for gene expression profiling [131-133]. To date, microfluidics for single-cell gene expression have integrated functional components involving single cell isolation and lysis [134], RNA purification [135], and RT-PCR [136]. While demonstrating a modular and integrable platform, a highly integrated microfluidic tool requires complex device design and complicated off-chip control instrumentation. For example, microfluidic single-cell isolation that uses valve-controlled chambers [137] relies on multilayer soft lithography, increasing the complexity of fabrication and pneumatic control. Microfluidic droplet-processing single-cell analysis devices typically require complex control with heating modules, particularly with the integration of droplet

generation and droplet thermo cycling [138]. We have previously developed a bead-based approach for performing RT-qPCR at the single-cell level on a microfluidic device, which featured integrated cell trapping, cell lysis, RT and qPCR on chip with high sensitivity and efficiency of the RT-qPCR reaction compared to off-chip RT-qPCR [38, 139]. While this approach has demonstrated sensitivity and efficiency in single-cell gene expression analysis, one limitation is that the cell trapping unit uses a geometric constraint to capture one single cell out of a group of cells, which does not allow tracking the identity of an individual cell. Commercial options also exist for performing single-cell gene expression analysis, such as the C1/BioMark system (Fluidigm, inc). Unfortunately, the input cells are sorted randomly, which hinders the tracking of individual cells from the time of irradiation to analysis.

This chapter presents an approach that combines single-cell picking, lysing, reverse transcription (RT) and photocleavage to enable the isolation, tracking and gene expression analysis of individual cells. A single-cell capillary picker introduces single cells into a microfluidic device, termed the Preprocessing for Gene-Expression Measurement (PreGEM) chip, which performs gene-expression preprocessing. This approach permits the isolation and quick lysis of individual cells, while avoiding the complex microenvironment required for culturing cells on chip [140], thereby enabling the study of microbeam-irradiated single cells and bystander effects. The PreGEM chip enables synthesizing and delivering stable cDNA for downstream gene expression analysis. The chip tracks the identity of individual cells in a single microfluidic channel, which is readily scalable by parallelization. A bead-based protocol is used to achieve mRNA capture and

the RT reaction, greatly simplifying both the design and operation of the microchip. Furthermore, instead of applying thermal denaturation (95℃) to release single-stranded DNA (ssDNA), which tends to cause evaporation issues [141], a photocleavage approach has been used to release cDNA from the beads realized via a photocleavable link between the bead and cDNA. Finally, the approach maximizes the choice of platforms for downstream analysis, such as qPCR real-time gene expression analysis, QuantStudio digital PCR sensitive detection or NanoString multi-gene expression analysis. We demonstrate the preprocessing approach using QuantStudio digital PCR by measuring expression levels of the radiation responsive genes [142, 143] Cyclin-dependent kinase inhibitor 1a (*CDKN1A*) and Growth/differentiation factor 15 (*GDF15*) as well as of the Prostaglandin-endoperoxide synthase 2 (*PTGS2*) gene (both radiation and bystander responsive [144]) in individual control, microbeam-irradiated or bystander IMR90 human lung fibroblasts after 4-hour co-culture. The results confirm the ability of the preprocessing approach to enable accurate tracking of single cells and efficient analysis of single-cell responses, as well as allow the comparison of activation levels of different genes and signaling pathways within individual cells.

5.2 Material and Methods

Cells

Normal human diploid lung fibroblasts (IMR-90) were obtained from the American Type Culture Collection (ATCC® CCL-186; Manassas, VA, USA). Cells at passage 10-12 were grown in Eagle's Minimum Essential Medium (CellGro, Manassas, VA, USA) supplemented with 12.5%

heat-inactivated (56° C, 30 min) fetal calf serum, 400 mM L-alanyl-L-glutamine, 100 U/ml penicillin and 100 µg/ml streptomycin (Sigma-Aldrich Corp., St. Louis, MO, USA). The cells were maintained at 37° C in a humidified incubator with 5% CO2 in air.

Cell Irradiation

Microbeam irradiations were performed at the Radiological Research Accelerator Facility (RARAF) [130], Columbia University. Twenty-four hours before the experiment, cells were seeded in two 12.5 cm^2 flasks at 70-80% confluence. The day of the experiment, one flask was incubated for 30 minutes with 100 nM Hoechst 33342 and the other with 200 nM MitoTracker Green (Thermo Fisher Waltham, MA USA). Cells from both flasks were then trypsinized and plated 1:1 on custom-made microbeam dishes [126] and allowed to attach for at least 1 h (Figure 5.1). Immediately before irradiation, the culture medium was removed from the microbeam dish. The microbeam dish was positioned adjacent to the microbeam exit window and a moisture containment collar was placed over the objective lens to keep the cells from becoming dehydrated during the approximately 15 min irradiation time. The RARAF microbeam system has integrated image analysis, which was used to visualize the nuclei stained with Hoechst 33342. A computer automated nuclear irradiation protocol found the location of every stained nucleus on the dish. We used the RARAF 5 MV Singleton Accelerator to deliver five doubly charged helium particles (He^{2+}), simulating an alpha particle, with an energy of 6.0 MeV to the center of each stained nucleus. The ion beam was measured to have a width of $<5\mu$m for all irradiations, and based on

SRIM calculations (Stopping Range of Ions in Matter) [145] , each He^{2+} particle had an LET of approximately 100 keV/µm. Cells showing nuclear stain were microbeam-irradiated while the MitoTracker Green-stained cells were not targeted and therefore were designated as "bystander" (Figure 5-1). The particle fluorescence was measured by a gas proportional counter positioned above the cells. After every nuclear stained cell on the plate had been irradiated the dish was removed from the irradiation endstation, fresh medium was added to the dish, and the dish was placed in the incubator at 37° C until ready for cell picking at 4 hours post irradiation. All control cells were stained with Hoechst 33342 and sham irradiated.

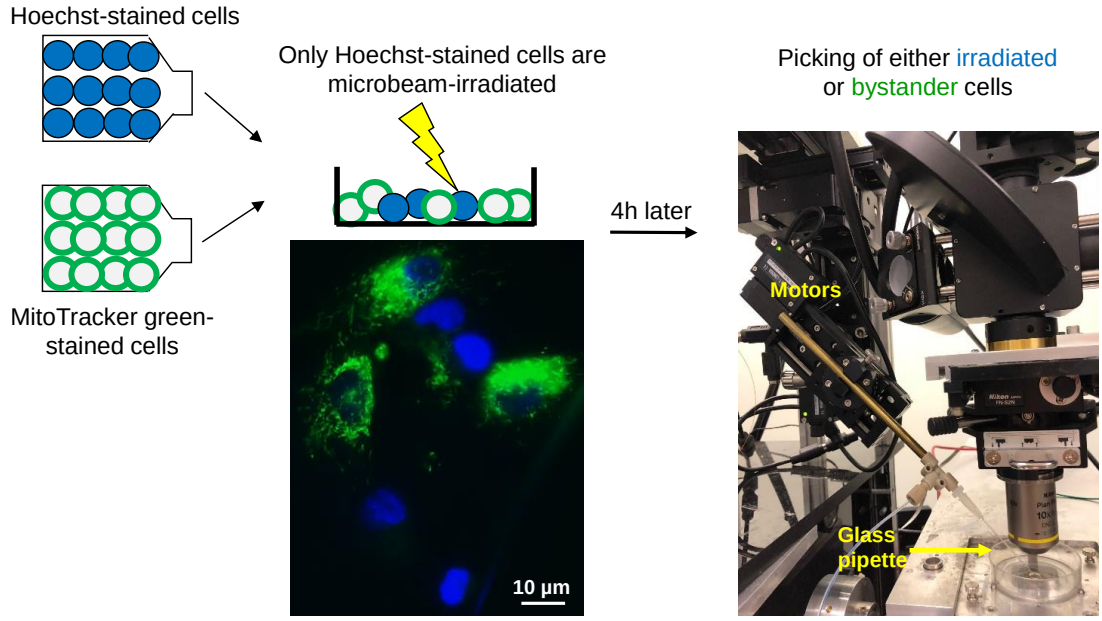

Figure 5–1: A co-culture of Hoechst-stained IMR-90 cells (blue) with MitoTracker green-stained IMR-90 cells (green) was established on microbeam dishes; at the endstation only Hoechst-stained cells were irradiated while the cytoplasmic-stained cells were designated as bystanders; single-cell picking was conducted 4 h after irradiation using a capillary micropipette with computer controlled positioning motors.

Cell Picking

Cells were viewed on a custom microscope using a 10x objective with live imaging (pco.edge 5.5, PCO, Kelheim, Lower Bavaria, Germany). Custom software allowed for imaging and lighting control as well as computer adjustment of the position of the pipette mounted on a 6 axis stage (X, Y, Z, azimuth, elevation and retraction; Zaber Technologies Inc., Vancouver, BC). 40 uL of 0.25% trypsin-EDTA was added to the microbeam dish prior to picking to aid in cell release. To pick a cell, the pipette was positioned directly adjacent to a cell of interest on the microbeam dish. Multi-color illumination, with the use of a Lumencor Aura Light Engine (Lumencor, Beaverton, OR), a light source (Morrell Instruments, Mellville, NY) and a camera (PCO-Tech Inc, Romulus, MI), allowed for simultaneous imaging of both the nuclear stain and cytoplasmic stain, thus permitting determination of the cell as "irradiated" or "bystander", respectively. Single cells were aspirated into the micropipette along with 1-3 µL of 0.25% trypsin-EDTA. After picking a cell, the micropipette was moved out of the microbeam dish and positioned within the input well of a PreGEM chip, where the picked cell was ejected directly into lysis buffer (Thermo Fisher, Waltham, MA).

Fabrication of Microfluidic PreGEM Chip

The chip (Figure 5-2a) is fabricated using standard soft lithography microfabrication techniques [146]. SU-8 photoresist (MicroChem Corp., Newton, MA) was spun-coated on a silicon

wafer and patterned with photolithography to define the liquid channel mold. Then, PDMS (Dow Corning) was poured over the mold and an additional vapor barrier [38] was embedded in the PDMS. Sheets bearing the microfluidic features were then peeled off the mold followed by inlet and outlet hole punching. The molded PDMS was sealed to a glass slide using oxygen plasma bonding.

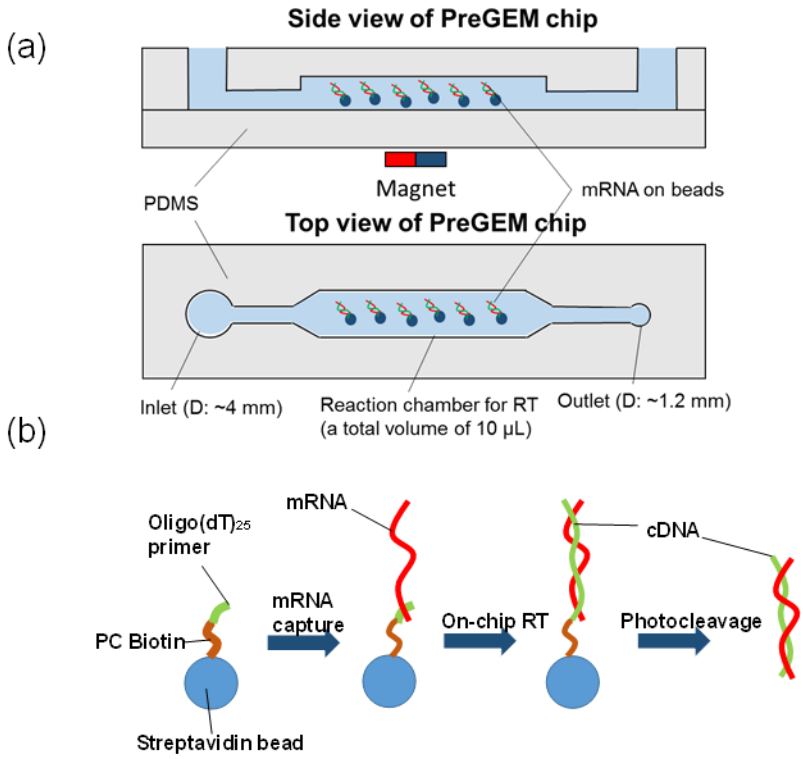

Figure 5–2: (a) Schematic of the side view of a PDMS PreGEM chip made by soft lithography. The microfluidic chip consists of an inlet for introduction of reagents, cell lysis and mRNA capture using magnetic beads as well as a reaction chamber for on-bead RT. (b) a bead-based process on the PreGEM chip: mRNA capture by Oligo(dT)$_{25}$ on beads, cDNA synthesis on beads during RT, and cDNA release by photocleaving the PC (photocleavable) Biotin linker on beads.

On-Chip RNA Capture

Different copy numbers of XenoRNA template (2×10^4, 5×10^4 and 10^5, Thermo Fisher Scientific Inc.) were introduced to the microchip, and were captured by 3.5×10^6 beads (Thermo Fisher Scientific Inc). Separating the magnetic beads from the remaining solution using a magnet, the effluent solution was transferred to micro tubes and mixed with another solution containing 3.5×10^6 beads, which was followed by off-chip RT. In the end, 40-cycle qPCRs were run to detect the amount of un-captured templates.

On-Chip RT Characterization

The efficiencies of the on-chip bead-based RT were investigated using various copy numbers of XenoRNA templates (2×10^4, 5×10^4 and 10^5, Thermo Fisher Scientific Inc.). The on-chip RTs were first conducted after mixing RT reagents, XenoRNA, biotinylated $Oligo(dT)_{25}$ primer (Integrated DNA Technologies Inc.) and 3.5×10^6 streptavidin magnetic beads. Subsequently, PCRs were performed with the products of RT using the qPCR system. In comparison for the on-chip efficiency, in-tube RTs were performed using a thermocycler followed by qPCR characterization. Additionally, to characterize the effects of beads on reaction efficiency, bead-based PCRs were subsequently performed with the products of in-tube RT by mixing and binding biotinylated cDNA to streptavidin beads, comparing the bead-based approach with the standard bench-top solution-based approach.

Single-Cell Processing on the PreGEM Chip

The input well of the PreGEM chip was pre-filled with the lysis buffer, so as to immediately lyse the input cell after it was picked and placed within the input well. Next, mRNA templates in the cell lysate were collected by photocleavable 5'-PC Biotin-$(dT)_{25}$-3' bead tether, which was made by incubating magnetic streptavidin beads (Thermo Fisher Scientific Inc.) with photocleavable biotinylated Oligo$(dT)_{25}$ (Integrated DNA Technologies Inc.). The principle of mRNA capture relies on base pairing between the polyA tails of the mRNA and Oligo$(dT)_{25}$ immobilized on the surface of the beads. In the reaction of reverse transcription (RT), the bead-bound Oligo$(dT)_{25}$ functions as a primer for synthesis of cDNA. Extracted mRNA were moved from inlet well to reaction chamber using a magnet, followed by the introduction of reverse transcription mix (dNTP, RT buffer, $MgCl_2$ solution, Reverse Transcriptase, RNase inhibitor). After RT (10 min at 25° C and 50 min at 42° C), the microchip was exposed under a UVA lamp (Sylvania Inc) photocleaving the PC linker, which released the cDNA from the beads.

In-Tube RT, qPCR and Digital PCR (dPCR)

In-tube RTs were run using a thermocycler (Eppendorf) with a standard protocol (10 min at 25° C and 50 min at 42° C). qPCRs were performed using 96-well reaction plates run on the 7900HT Fast Real-Time PCR (Applied Biosystems). 5 μL RT products, 6.25 μL nuclease-free water, 1.25 μL Taqman gene expression assay (Hs99999905_m1, Thermo Fisher Scientific Inc.) and 12.5 μL Taqman gene expression master mix were loaded on the plates, which were run for 45 cycles. The QuantStudio 3D digital PCR system (Thermo Fisher Scientific Inc.) was used to

conduct digital PCRs. Starting samples in a final volume of 15 μL that consisted of bead-excluded RT product, Taqman gene expression master mix (Thermo Fisher Scientific Inc.), Taqman gene expression assay (Hs99999142_m1, Hs00153133_m1, Hs00171132_m1, Thermo Fisher Scientific Inc.) and nuclease-free water were loaded onto Digital PCR Chips (Applied Biosystems) via the QuantStudio 3D Digital Chip Loader (Applied Biosystems). The chips were immersed in oil to avoid evaporation and sealed with UV sealant (Applied Biosystems). This was followed by running 40 cycles of dPCR using GeneAmp® PCR system 9700 Thermocycler, which is adapted for digital PCR reactions. The chips were then loaded onto the QuantStudio™ 3D Digital PCR Instrument, and the end-point fluorescence of each well on the chips was measured using QuantStudio™ 3D Digital PCR software v3.0. The fluorescence data were read and analyzed using QuantStudio 3D Analysis Suite Cloud Software.

Statistical Analysis

Statistical differences between two groups of cells were determined using unpaired two-sample t-test or one-way ANOVA followed by post-hoc Tukey test, where necessary. Pearson correlation coefficient (*r* value) was used to measure the linear relationship between expression levels of two genes. Defined as the covariance of two variables divided by the product of their standard deviations and calculated as follows: $r = \frac{\sum_{i=1}^{n}(x_i - \bar{x})(y_i - \bar{y})}{\sqrt{\sum_{i=1}^{n}(x_i - \bar{x})^2 \sum_{i=1}^{n}(y_i - \bar{y})^2}}$, where *x* and *y* represent variables and n is the number of experiments. The Kolmogorov-Smirnov test was used to test the normality of the samples and to decide whether the distribution functions of two samples are

significantly different. R (version 3.1.1) was used to perform statistical analysis.

5.3 Results

In the experiments, we first performed on-chip RNA capture validation, then characterized on-chip RT efficiency and bead-based reaction efficiency, as well as quantifying the releasing efficiency of cDNA from beads. We then demonstrated single-cell analysis with the integrated system from microbeam irradiation, cell picking, and on-chip reactions, all the way through QuantStudio dPCR. The integration of the system allows the exploration of cell-to-cell variability in response to microbeam irradiation and in bystander cells.

Validation of RNA Capture on the Pre-GEM Microchip

Before characterizing efficiencies of downstream reactions, the on-chip capture of mRNA via 5'-PC-Biotin-$(dT)_{25}$-3' Streptavidin magnetic beads was validated using XenoRNA template. The value of ΔR_n, indicating the magnitude of the fluorescent signal and, therefore, amplification generated by PCR, was 3.7 for the positive control (10^5 XenoRNA with 3.5×10^6 beads) after 40 cycles of bead-based PCR. Referring to the method section, the remaining solutions after bead capture were mixed with bead-based solution, and RT-PCRs were performed to quantify remaining templates in the solution after the first capture. It was found that the ΔR_n values remained below the threshold (Figure 5-3). Thus, we can conclude that 3.5×10^6 beads were sufficient to capture essentially all of the polyAdenylated templates, and an undetectable amount of free RNA templates were residual in the binding waste.

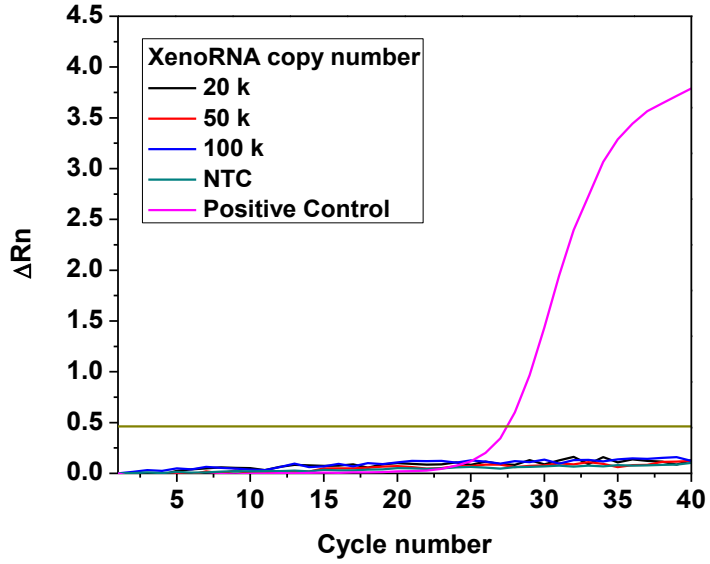

Figure 5–3: Quantified detection of RNA trapping efficiency using 3.5×10^6 beads. There was no detectable residual XenoRNA template in the binding waste.

On-Chip RT Characterization and Interference of Beads with Reaction Efficiency

Starting with 20k, 50k and 100k copies of XenoRNA, the on-chip bead-based RTs followed by off-chip bead-based qPCRs were conducted to test repeatability and characterize reaction efficiency (Figure 5-4a). We found that under the given experimental conditions, the PCR efficiency defined by $(10^{-1/k}-1)\times 100\%$, where k is the slope of the C_t as a function of the logarithm of the template copy number, for our bead-based approach was 90.5%. To characterize the on-chip RT efficiency, we conducted the bead-based PCR testing following in-tube RT. The PCR efficiency E_b for the bead-based PCR with in-tube RT was 83.2%, meaning the bead-based on-chip RT has a 1.08-fold increase in efficiency compared with that of in-tube RT. This improved efficiency for on-chip reaction likely resulted from more efficient molecular interactions in the microscale

environment [131, 147]. Meanwhile, we ran a solution-based PCR without introducing beads following in-tube RT. Some bead interference was observed, affecting the reaction efficiency, as the presence of beads during the PCR reaction yielded higher *Ct* values than the solution-based reactions. In terms of the reaction efficiency, it was found in Figure 5.4b that under the given experimental conditions, the PCR efficiency E_s for the solution-based PCR testing (86.3%) was higher than the PCR efficiency E_b for the bead-based PCR (83.2%), which was likely attributable to enhanced molecular interactions in the absence of the beads. The reaction efficiency was not dependent on template copy number, however. Based on these results, we calculated a correction factor that can be used to estimate the corrected threshold cycle of the bead-based approach in order to offset the influence of beads on the reaction. The corrected threshold cycle can be evaluated by $Ct_s=Ct_b\times\log(1+E_b)/\log(1+E_s)$, where Ct_b, Ct_s, E_s, and E_b denote threshold cycle of the bead-based positive controls, threshold cycle of the corrected positive controls, solution-based PCR efficiency, and bead-based PCR efficiency, respectively.

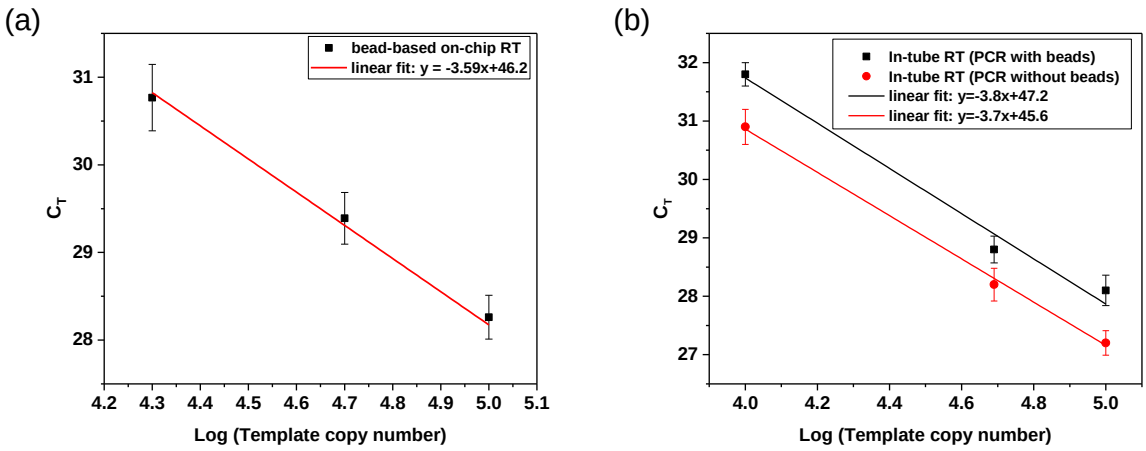

Figure 5–4: (a) Mean and standard deviation of on-chip bead-based RT followed by offchip bead-based qPCR. (b) Mean and standard deviation of in-tube RT followed by bead-based offchip qPCR and solution-based offchip qPCR, respectively.

Characterization of the Releasing Efficiency of cDNA from the Beads via On-Chip Photocleavage

It is also important to know the releasing efficiency of cDNA from the beads via on-chip photocleavage. Therefore, an experiment was designed to characterize the release efficiency (Figure 5-5). The first arm of the experiment used on-chip cell lysis, mRNA capture, and RT processing of a small number (10) of IMR-90 cells obtained by dilution. Without photocleavage, the RT products (cDNA on beads) were collected and analyzed by qPCR. We next performed on-chip lysis of 10 cells, mRNA capture and RT, followed by on-chip photocleavage via UV irradiation (peak wavelength: 365nm). The beads were separated from the cleaved RT product (cDNA), and qPCR analyses were performed separately using the cDNA cleaved from the beads and the remaining beads. Looking at the amplification curves for the housekeeping gene GAPDH, there is negligible amplification of the cleaved beads, indicating the cDNA has been effectively

removed from the beads by the UV irradiation. We have also noticed that the threshold cycle Ct_b of cDNA-on-beads amplification (Positive Control: A1, A2 and A3) are higher than the *Ct* of cDNA in solution (C1, C2 and C3), which would be expected, given that we have already shown that the bead-based approach has a lower PCR efficiency than solution-based reactions (Figure 5-5b). Evaluating the releasing efficiency of cDNA from the beads requires the corrected threshold cycle Ct_s, which has been defined as previously defined. Thus, the releasing efficiency defined as $(1+E_s)^{-Ct}/(1+E_s)^{-Cts}$ is estimated to be (mean ± s.d.) 95.6% ± 3.5% using experimentally determined cycle threshold (Ct_b and *Ct*) and PCR efficiency (E_s and E_b).

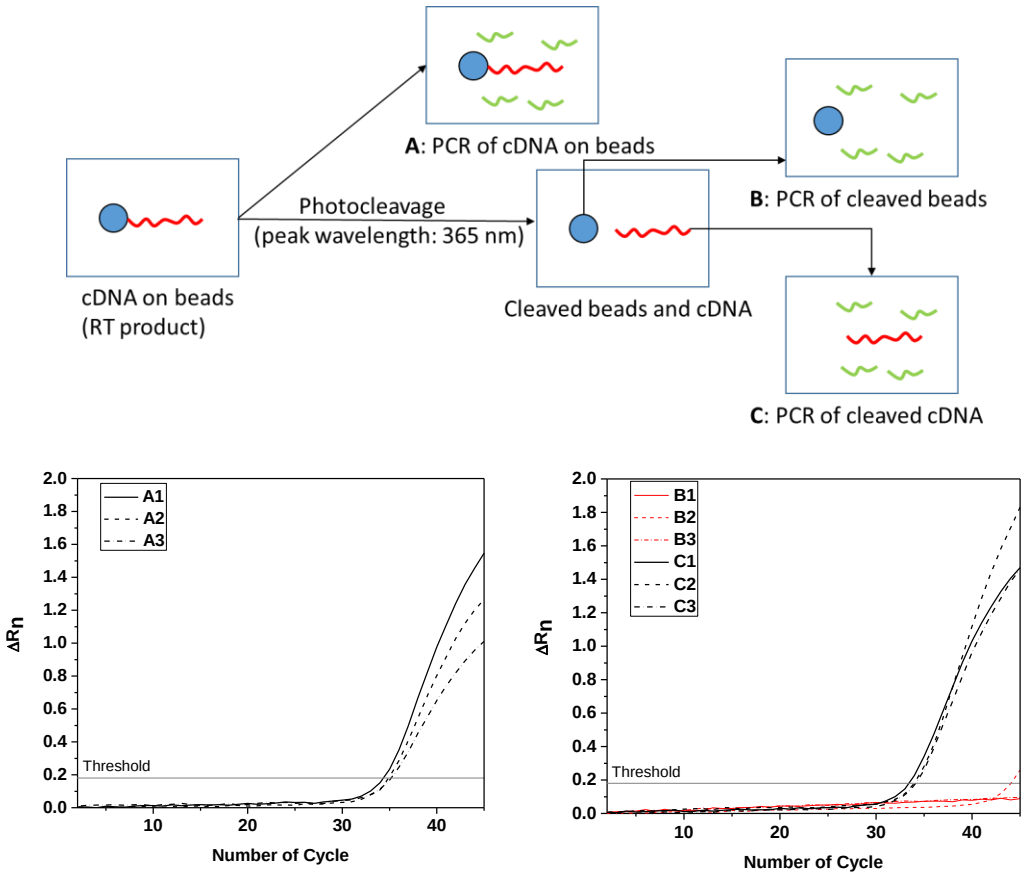

Figure 5–5: Schematic of experiment flow and qPCR following on-chip cDNA synthesis using magnetic beads, A: perform PCR with cDNA on beads, B: photocleave beads and run PCR with beads only, C: use

the photocleaved cDNA product from B to run PCR. Solid, dashed and dash-dot curves represent independent experiments per experiment group.

Microbeam-Irradiated and Bystander Single Cells

Having characterized the bead-based process on chip, we were ready to integrate the PreGEM chip with the cell picker and study the single-cell response to microbeam irradiation as well as the bystander effect. 30 Individual control, 30 microbeam-irradiated and 30 bystander single cells were one by one picked from microbeam dishes via the cell picker and transferred to the microchips and processed for cell lysis, mRNA capture, RT and photocleavage. The recovered cDNAs from the on-chip reaction were then used to run digital PCR reactions with analysis on the QuantStudio platform. The QuantStudio uses limiting dilution of the reaction mix to count individual molecules, providing absolute quantification of gene expression levels using Poisson statistics. Figure 5-6 presents the distribution of individual control cells, bystander cells and irradiated cells based on the quantities of *PTGS2*, *CDKN1A* and *GDF15* in each cell. One interesting observation is the elevated variability in expression levels in both bystander cells and irradiated cells compared to controls. For example, the expression levels of *CDKN1A* among irradiated cells distribute in a range of 15 to 165 counts while bystander cells have a narrower range of 0 to 45 counts, compared to that the control cells fall within a range of 0 to 25 counts. Also, it was found that the expression levels of both *CDKN1A* and *GDF15* in irradiated cells are significantly higher than the expression levels for both genes in bystander cells ($p < 0.001$). The average fold-changes for *CDKN1A* and *GDF15* in irradiated cells are 7.56 and 7.37, respectively, while the average fold-changes for these

two genes in bystander cells are 2.54 and 2.19, with respect to the mean value of the two genes in control cells. While for *PTGS2*, the average fold-changes are 6.77 and 5.24 in irradiated cells and bystander cells, respectively.

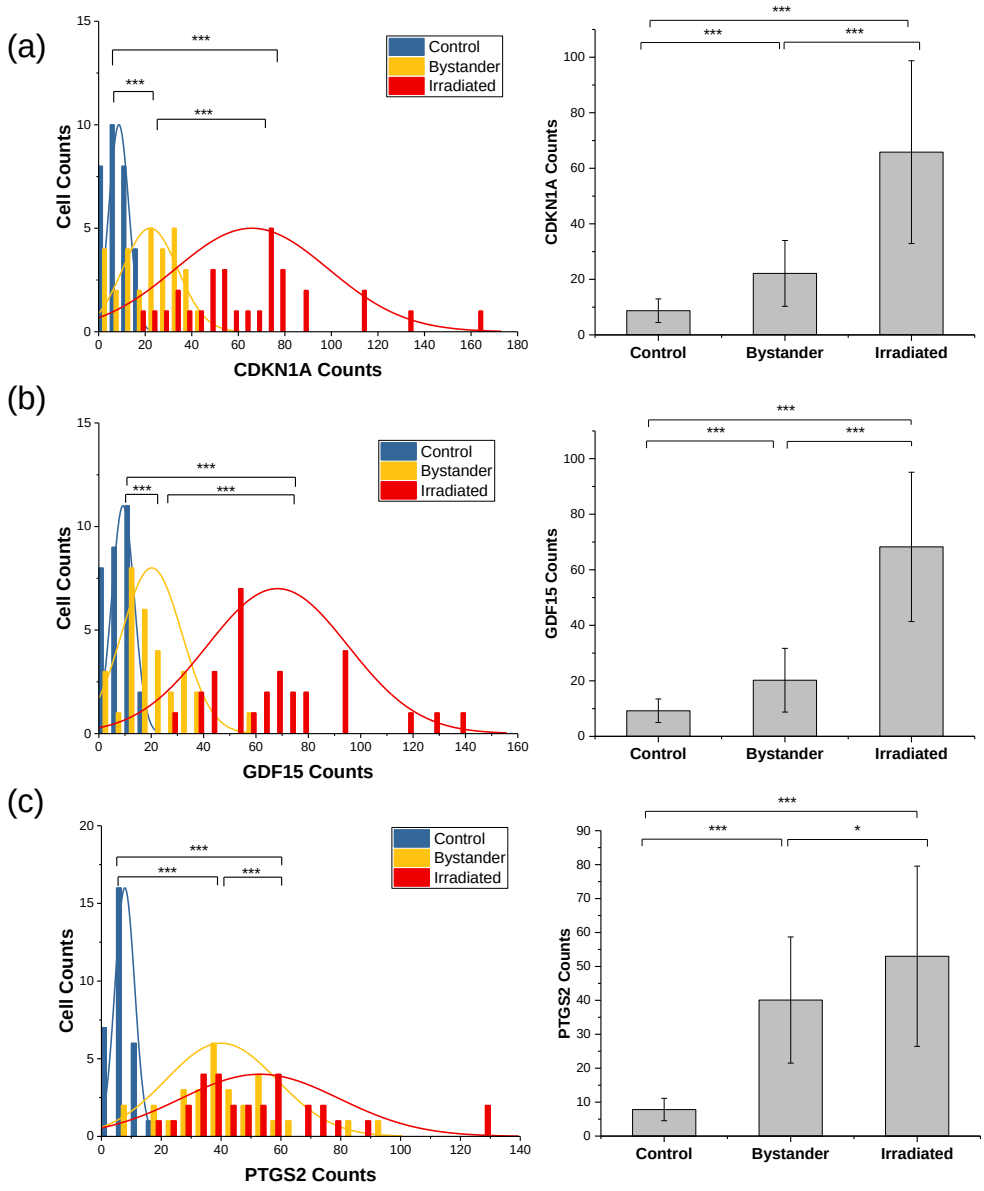

Figure 5–6: Left column: Significantly different distributions of transcript numbers of *CDKN1A*, *PTGS2* and *GDF15* as measured by digital PCR from individual control, bystander and microbeam-irradiated IMR90 cells. Right column: Comparisons of mean quantities of three gene products: *CDKN1A*, *PTGS2* and

GDF15 averaged over 30 individual control, bystander and microbeam-irradiated IMR90 cells. One asterisk (*) indicates $p < 0.05$ and three asterisks (***) indicate $p < 0.001$.

In order to compare the expression levels of the three genes within individual cells, regression analyses were applied to data points corresponding to expression levels of *CDKN1A* compared with those of *PTGS2* and *GDF15*. We found that a linear model was not significant to explain the relationship between the expression levels of *CDKN1A* and *PTGS2*, which represent two different signaling pathways, in individual control, bystander and irradiated cells (Figure 5-7a, c, e). Conversely, expression of the two p53-regulated genes, *GDF15* and *CDKN1A*, was significantly correlated within individual cells ($p < 0.05$). Additionally, the *r* values were calculated in terms of the expression levels of *CDKN1A* and *GDF15* for sets of control, bystander and irradiated cells. A strong linear relationship was found for *CDKN1A* against *GDF15* among irradiated cells ($r = 0.80$), while the correlation decreased between these genes in bystander cells due to elevated variance ($r = 0.65$).

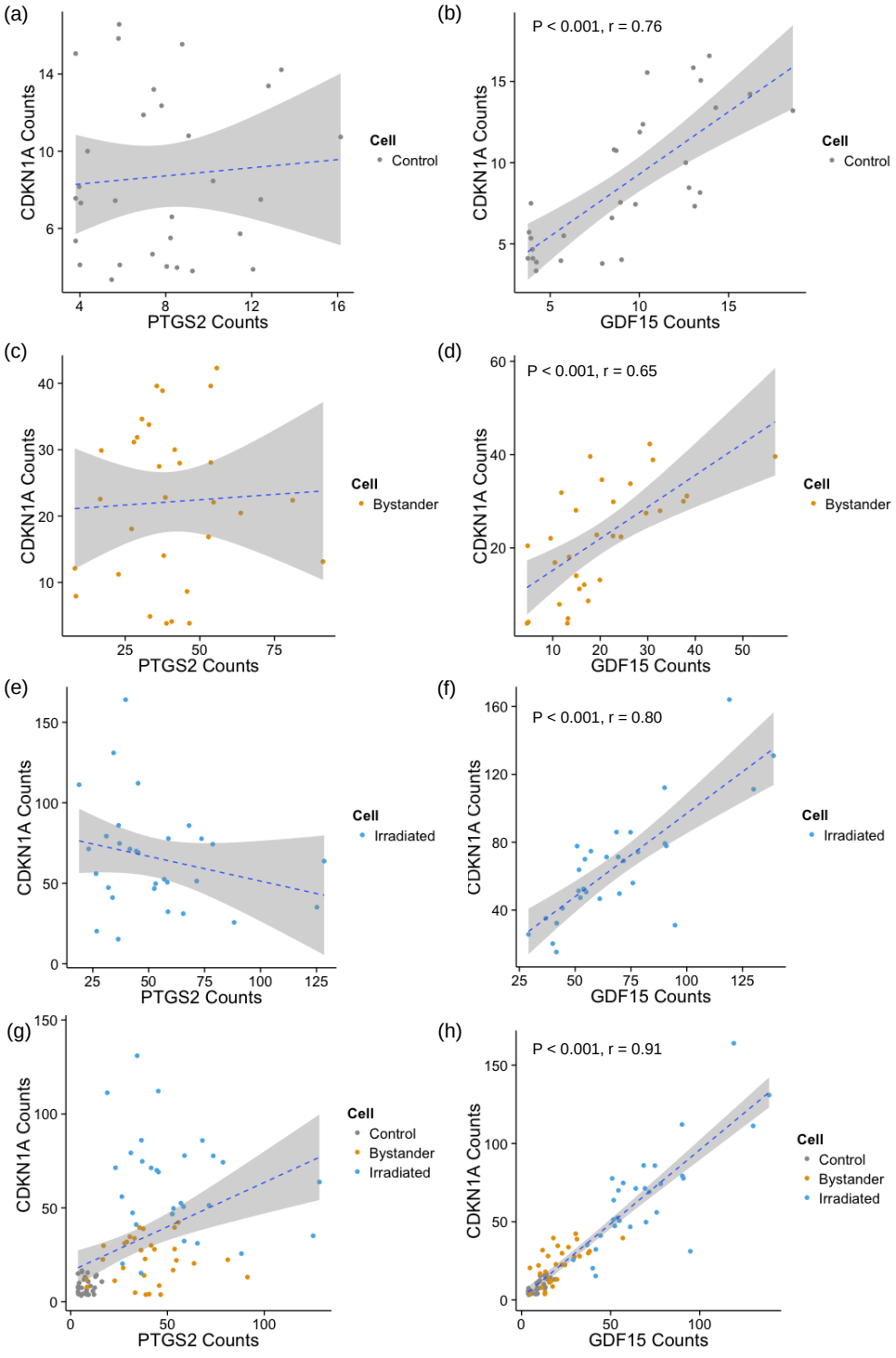

Figure 5–7: Scatter plots of expression levels of *CDKN1A* against *PTGS2* (a) (c) (e) (g) and *CDKN1A* against *GDF15* (b) (d) (f) (h). Grey shading represent 95% confidence level interval for predictions from a linear model (blue dashed line).

5.4 Discussion

To support our microbeam studies of the radiation bystander effect, we have developed a system to perform single-cell gene expression measurements following irradiation with the microbeam. This system empowers our single-cell irradiation studies, allowing individual microbeam-irradiated cells or non-hit bystander cells to be tracked, lysed, and prepared for analysis. Our approach could also be applied to studies of rare cells in many other contexts. Gene expression variability in rare cells is of great interest for applications including cancer diagnosis [148], cancer drug development [149] and prenatal diagnosis [150]. While much can be learned through studying gene expression response in bulk cell populations, such analysis of gene expression dilutes the contribution of these rare cells to the pattern of the population. Information that covers the diversity and complexity of the cells as well as their unique molecular signatures is thereby lost.

The utility of the integrated preprocessing system was demonstrated by interfacing with QuantStudio digital PCR. The end-to-end analyses from microbeam irradiation to digital PCR gene expression measurements indicate cell-to-cell variability among individual control, microbeam-irradiated as well as bystander cells. It is critical to know that such variability is mainly due to the cell-to-cell differences in gene expression rather than being introduced by measurement noise. As can be seen from Figure 5.6, the mean quantities of each gene in irradiated and bystander cells are greater than the mean of the gene in individual control cells. While the measurement noise would be expected to decrease with elevated abundance of transcripts, the variance in irradiated and bystander cells is larger than the variance in controls. This would indicate that there is minimal

effect on dispersion from measurements and the variance of the single-cell data reflects actual cell-to-cell differences.

The response of lung fibroblast cells to radiation has been extensively studied by microarray and qRT-PCR [117][151][152][153]. For example, global gene expression four hours after bystander and direct alpha particle exposure of lung fibroblast cells was measured, revealing disparate roles of two major radiation response pathways, p53 and NFκB, in the bystander response. Activation of the p53 response pathway was found to be minimal in bystander cells, in contrast with the NFκB pathway, which appeared to respond identically in bystander and irradiated cells [144]. Additionally, lung fibroblasts were exposed to alpha-particle radiation at a dose range of 0-1.5 Gy, after which the *GDF15* gene, regarded as a marker for lung injury, was assessed at the protein level and 3-fold higher expression levels were found in exposed cell culture media 24 hours after exposure [154]. The single-cell data presented in Figure 5.6 are consistent with these studies, which could be explained by the previous observation that p53-regulated genes like *CDKN1A* and *GDF15* were expressed at elevated levels in directly irradiated cultures, while showing little or no change in bystanders [144]. In contrast, the response pattern of NFκB regulated genes such as *PTGS2* was found to be virtually identical in bystander and irradiated cells.

What was missed in the above studies was the heterogeneity of responses within bystander and irradiated populations. While studies in populations gave an averaged cellular response, it is clear that the presented genes were not uniformly expressed across even a small population of cells (n = 30) within each treatment set. Within irradiated cells, expression levels for any particular gene

may not be uniformly elevated among the cells, in addition to inherent cell-to-cell differences revealed in the controls (Figure 5.6). Signaling and response mechanisms in bystander cells are complex, involving both direct contact and gap junctions between bystanders and irradiated cells [155, 156] as well as communication through extra-cellular signals in the culture media [157, 158]. Thus, it is possible that the distance between an irradiated cell and a non-hit bystander, the concentration gradient of signaling molecules in the media, and the movement of the media could contribute to the observed differences in gene expression across bystander cells.

Within the same signaling pathway, *CDKN1A* and *GDF15* both are p53-induced genes [159], and it is clear from Figure 5.7h that they are significantly correlated in microbeam-irradiated cells, and to a lesser extent in control and bystander cells. It is known that *GDF15*, which contains two p53 binding sites in its promoter region, is a direct target gene of p53 [160]. Radiation-induced DNA damage can induce *GDF15* expression in a p53-dependent manner. It has also been found that *GDF15* holds a moderate but significant association with p53 after DNA damage [161], which would indirectly reveal the correlation of genes *CDKN1A* and *GDF15* within the p53 pathway.

Next consider the pair of *CDKN1A* and *PTGS2*, which represents activation of different pathways including p53 and NFκB. The former gene plays essential roles in the DNA damage response [162] and the latter counteracts p53 activity as well as inhibits DNA damage-induced apoptosis [163] [164]. As seen from Figure 5.7, the correlations between the two genes in controls and bystanders are weak and positive while the two genes were found to be negatively related in irradiated cells. The negative trend observed between *CDKN1A* and *PTGS2* in irradiated cells may

imply a transcriptional cross talk between NF-κB and p53, in which both pathways inhibit each other's ability to stimulate gene expression and this process is likely dependent on the relative levels of the two transcripts [165]. It has been suggested that stimulation of NF-κB promotes resistance to programmed cell death while the activation of p53 is associated with the induction of apoptosis or cell cycle arrest following DNA damage [166] [167]. If this is indeed the case, it is possible that NF-κB activation occurs simultaneously with the induction of p53 in a few individual cells shown in Figure 5.7e, which exhibited equally high levels of expression of both genes, but that activation of the two pathways is not tightly linked within the same cell.

5.5 Conclusions

In summary, the data presented in this chapter demonstrate the preprocessing approach for single-cell irradiation studies, and together with qPCR or digital PCR provide a powerful approach to investigate the variability of gene expressions in individual cells with microbeam irradiation, and many other applications where rare cells are of interest.

Chapter 6. Concluding Remarks

6.1 Summary of the Thesis

This thesis discusses mathematical modeling and experimental characterization for bioanalytical applications. The work presented in the thesis includes the modeling of a microplate-based viscometric glucose sensor, for prediction of frequency response of the sensor at a variety of glucose concentrations; the modeling of a microcantilever-based viscometric glucose sensor, for parametric study of the sensor's response when varying geometric and material properties; the capacitive measurements of a hydrogel-based glucose sensor, for enabling continuous glucose monitoring in a reversible manner; and an integrated preprocessing approach for gene expression measurement at single-cell level.

The work incorporated in this thesis can be divided into four chapters, each of which is summarized below.

The model of the diaphragm-based glucose sensor reveals the general trend in the experimentally observed sensor characteristics with nominal material properties by comparing the estimation of the model with experimental results. Besides, parametric studies with the model show that the deflection of the diaphragm at the resonance frequency is strongly dependent on the height of liquid chamber due to squeeze-film damping effects. Additionally, simulation results using the model suggest that the composition of polymer solution can be tuned to optimize the glucose sensing. Thus, the model enables efficient and accurate quantitative determination of dynamic characteristics of diaphragm-based viscometric glucose sensor, and can be extended to

other bioanalytical microdevices involving complex fluid structure interaction.

This thesis also develops a model of the microcantilever-based viscometric glucose sensor. The model couples the structural vibration of the cantilever with the flow via boundary conditions at the beam-liquid interface, and is capable of predicting the dynamic behavior of the vibrational glucose sensor while providing detailed insight into the sensors' characteristics. By considering the surface stress, this model is generalized to cases where the microcantilever-based sensors are used for biochemical sensing via surface binding. Additionally, the dynamic response of the cantilever under thermal excitation has been investigated. It is found that the thermal noise does not change monotonically with Reynolds number and the variation of the noise is strongly dependent on the intensity of viscous dissipation, which will be of significant practical value to precise measurements.

As an exploratory study on dielectric glucose sensor, this thesis introduces a hydrogel-based glucose sensor, detecting glucose via dielectric measurements. This microsensor eliminates the use of mechanical moving parts existing in viscometric glucose sensors that hinders miniaturization. The hydrogel is directly embedded on the transducer via in situ polymerization and will be stable over time, allowing the device to remove a semipermeable membrane that are otherwise required to hold the glucose-sensitive material, and potentially offer improved tolerance to biofouling during implanted operation. Experimental results demonstrate that in a glucose concentration range of 0–500 mg/dL and with a resolution of 0.35 mg/dL or better, the microsensor exhibits a repeatable and reversible response, and can potentially be useful for continuous glucose

monitoring in diabetes care.

This thesis has explored the integration of a capillary cell picker and a bead-based microfluidic platform for studying the variability in gene expressions among single cells, particularly with treatment of ionizing irradiation. Our current approach have enabled the study of irradiated single cells as well as bystander effect by incorporating a single-cell capillary picker to introduce single cells into a microfluidic gene-expression preprocessing chip. The approach has been demonstrated with QuantStudio digital PCR by measuring expression levels of the radiation responsive genes, Cyclin-dependent kinase inhibitor 1a (CDKN1A) and Growth/differentiation factor 15 (GDF15) as well as of the Prostaglandin-endoperoxide synthase 2 (PTGS2) gene (both radiation and bystander responsive) in individual control, microbeam-irradiated or bystander IMR90 human lung fibroblasts cells after 4-hour coculture. The results confirm accurate tracking of cell treatments through the system and efficient analysis of single cell responses, and also allow comparison of activation levels of different genes and signaling pathways within individual cells.

6.2 Directions for Future Work

In the research presented in this thesis, we have investigated device physics on vibrational glucose sensors, and have demonstrated an explorative development of a hydrogel-based dielectric glucose sensor. Surface-immobilized hydrogel has exhibited great potential in real-time monitoring of physiologically relevant glucose concentrations. Note that the microsensor is limited by a slow time response (~20 min), which can be attributed to use of a thick hydrogel layer (~250

μm) and an in vitro testing flow cell. Therefore, in the future work, we will immobilize a thinner layer of hydrogel by spinning coating the polymerization mixture and manufacture a new testing setup to reduce the convective-diffusive distance of transporting the glucose. To achieve the goal of subcutaneously implanted continuous glucose monitoring, in vivo study of the dielectric glucose sensor needs to be conducted in sedated rats to test the low-range measurement accuracy. The sensor's response to low glucose concentrations and the time delay of the sensor would be evaluated by comparing to the readings of the glucometer. Moreover, multiple sensors would be implanted in a group of rats for measurements to evaluate the clinical accuracy of the hydrogel-based sensors. In addition, an electrokinetic model would be built to correlate the hydrogel dielectric response to glucose concentration. Empirical data of the dielectric glucose sensor could be used to calibrate the prediction model.

The work presented in Chapter 5 has established a solid groundwork for the tracking of cell identity while conducting single-cell gene expression analysis. In our case, the preprocessing-gene-expression-analysis microchip can be readily scaled up to form a multi-channel chip on which multiple channels can be integrated with their reaction units to increase the throughput. Moreover, multiplex gene expression assays will be used to allow the multi-gene expression analysis. Further work is required for the development of such devices and optimization of assays. One prominent issue would be to handle the fluidic sample delivery and manipulation, especially when there are multiple inlets, and the application requires synchronized reagents input. The other challenge would be to integrate a pre-amplification module onto the microfluidic preprocessing

chip. Additionally, the multiplex gene expression assay will be optimized while interfacing the microfluidic chip with the NanoString nCounter, which is a multiplexed detection system with measurement of up to 800 genes in an individual cell [168].

Bibliography

[1] F. Lottspeich and J. W. Engels, *Bioanalytics: Analytical Methods and Concepts in Biochemistry and Molecular Biology*: Wiley, 2018.

[2] F. E. Lottspeich, J., "Bioanalytics: Analytical Methods and Concepts in Biochemistry and Molecular Biology," *Wiley*, 2018.

[3] M. Jemal and Y. Q. Xia, "The need for adequate chromatographic separation in the quantitative determination of drugs in biological samples by high performance liquid chromatography with tandem mass spectrometry," *Rapid Communications in Mass Spectrometry*, vol. 13, pp. 97-106, 1999.

[4] J. G. Moller, H. Stass, R. Heinig, and G. Blaschke, "Capillary electrophoresis with laser-induced fluorescence: a routine method to determine moxifloxacin in human body fluids in very small sample volumes," *Journal of Chromatography B*, vol. 716, pp. 325-334, Sep 25 1998.

[5] J. R. Yates, "Mass spectrometry - from genomics to proteomics," *Trends in Genetics*, vol. 16, pp. 5-8, Jan 2000.

[6] V. S. Y. Lin, K. Motesharei, K. P. S. Dancil, M. J. Sailor, and M. R. Ghadiri, "A porous silicon-based optical interferometric biosensor," *Science*, vol. 278, pp. 840-843, Oct 31 1997.

[7] H. J. Pandya, K. Park, W. J. Chen, L. A. Goodell, D. J. Foran, and J. P. Desai, "Toward a Portable Cancer Diagnostic Tool Using a Disposable MEMS-Based Biochip," *Ieee Transactions on Biomedical Engineering*, vol. 63, pp. 1347-1353, Jul 2016.

[8] F. N. Pirmoradi, A. V. Pattekar, F. Linn, M. I. Recht, A. R. Volkel, Q. Wang, *et al.*, "A microarray MEMS device for biolistic delivery of vaccine and drug powders," *Human Vaccines & Immunotherapeutics*, vol. 11, pp. 1936-1944, Aug 3 2015.

[9] S. Qiu, L. Liu, H. Y. Zhao, Z. L. Wang, and Y. M. Jiang, "MEMS Inertial Sensors Based Gait Analysis for Rehabilitation Assessment via Multi-Sensor Fusion," *Micromachines*, vol. 9, Sep 2018.

[10] Y. C. Song, D.; Zhao, Liang, "Microfluidics: Fundamentals, Devices, and Applications," *Wiley*, 2018.

[11] https://www.cdc.gov/diabetes/data/, 2015.

[12] G. Mancini, M. G. Berioli, E. Santi, F. Rogari, G. Toni, G. Tascini, *et al.*, "Flash Glucose Monitoring: A Review of the Literature with a Special Focus on Type 1 Diabetes," *Nutrients,* vol. 10, Aug 2018.

[13] A. Al Hayek, "Evaluation of Freestyle Libre Flash Glucose Monitoring System on Glycemic Control, Health-Related Quality of Life, and Fear of Hypoglycemia in Patients with Type 1 Diabetes," *Diabetes Technology & Therapeutics,* vol. 20, pp. A147-A147, Feb 2018.

[14] S. Vashist, "Continuous Glucose Monitoring Systems: A Review," *Diagnostics,* vol. 3, p. 385, 2013.

[15] T. Battelino, M. Phillip, N. Bratina, R. Nimri, P. Oskarsson, and J. Bolinder, "Effect of continuous glucose monitoring on hypoglycemia in type 1 diabetes," *Diabetes Care,* 2011.

[16] J. M. Lawrence, L. Laffel, T. Wysocki, D. Y. Xing, W. V. Tamborlane, and W. Comm, "Quality-of-life measures in children and adults with type 1 diabetes Juvenile Diabetes Research Foundation Continuous Glucose Monitoring randomized trial Diabetes Care (vol 33, pg 2175, 2010)," *Diabetes Care,* vol. 33, pp. 2725-2725, Dec 2010.

[17] D. A. Gough, L. S. Kumosa, T. L. Routh, J. T. Lin, and J. Y. Lucisano, "Function of an Implanted Tissue Glucose Sensor for More than 1 Year in Animals," *Science Translational Medicine,* vol. 2, Jul 28 2010.

[18] H. Kudo, T. Sawada, E. Kazawa, H. Yoshida, Y. Iwasaki, and K. Mitsubayashi, "A flexible and wearable glucose sensor based on functional polymers with Soft-MEMS techniques," *Biosensors & Bioelectronics,* vol. 22, pp. 558-562, Oct 15 2006.

[19] S. Xi, T. L. Shi, D. Liu, L. L. Xu, H. Long, W. X. Lai, *et al.*, "Integration of carbon nanotubes to three-dimensional C-MEMS for glucose sensors," *Sensors and Actuators a-Physical,* vol. 198, pp. 15-20, Aug 15 2013.

[20] M. Pan, X. S. Guo, Q. Cai, G. Li, and Y. Q. Chen, "A novel glucose sensor system with Au nanoparticles based on microdialysis and coenzymes for continuous glucose monitoring," *Sensors and Actuators a-Physical,* vol. 108, pp. 258-262, Nov 15 2003.

[21] B. U. Moon, M. G. de Vries, C. A. Cordeiro, B. H. C. Westerink, and E. Verpoorte, "Microdialysis-Coupled Enzymatic Microreactor for in Vivo Glucose Monitoring in Rats," *Analytical Chemistry,* vol. 85, pp. 10949-10955, Nov 19 2013.

[22] H. M. Heise, U. Damm, M. Bodenlenz, V. R. Kondepati, G. Kohler, and M. Ellmerer,

"Bedside monitoring of subcutaneous interstitial glucose in healthy individuals using microdialysis and infrared spectrometry," *Journal of Biomedical Optics,* vol. 12, Mar-Apr 2007.

[23] T. Tokuda, M. Takahashi, K. Uejima, K. Masuda, T. Kawamura, Y. Ohta, *et al.*, "CMOS image sensor-based implantable glucose sensor using glucose-responsive fluorescent hydrogel," *Biomedical Optics Express,* vol. 5, pp. 3859-3870, Nov 1 2014.

[24] S. Kuenzi, E. Meurville, E. Grandjean, S. Straessler, and P. Ryser, "Contactless rotational concentric microviscometer," *Sensors and Actuators a-Physical,* vol. 167, pp. 194-203, Jun 2011.

[25] C. J. Zhang, G. G. Cano, and P. V. Braun, "Linear and Fast Hydrogel Glucose Sensor Materials Enabled by Volume Resetting Agents," *Advanced Materials,* vol. 26, pp. 5678-+, Aug 27 2014.

[26] X. Huang, S. Q. Li, J. S. Schultz, Q. Wang, and Q. Lin, "A dielectric affinity microbiosensor," *Applied Physics Letters,* vol. 96, Jan 18 2010.

[27] X. Huang, S. Q. Li, J. S. Schultz, Q. Wang, and Q. Lin, "A MEMS affinity glucose sensor using a biocompatible glucose-responsive polymer," *Sensors and Actuators B-Chemical,* vol. 140, pp. 603-609, Jul 16 2009.

[28] X. Huang, C. Leduc, Y. Ravussin, S. Q. Li, E. Davis, B. Song, *et al.*, "A differential dielectric affinity glucose sensor," *Lab on a Chip,* vol. 14, pp. 294-301, 2014.

[29] X. Huang, S. Q. Li, E. Davis, C. Leduc, Y. Ravussin, H. G. Cai, *et al.*, "A MEMS differential viscometric sensor for affinity glucose detection in continuous glucose monitoring," *Journal of Micromechanics and Microengineering,* vol. 23, May 2013.

[30] Y. L. Song, T. Tian, Y. Z. Shi, W. L. Liu, Y. Zou, T. Khajvand, *et al.*, "Enrichment and single-cell analysis of circulating tumor cells," *Chemical Science,* vol. 8, pp. 1736-1751, Mar 1 2017.

[31] H. P. Zheng, Y. Pomyen, M. O. Hernandez, C. Y. Li, F. Livak, W. Tang, *et al.*, "Single-cell analysis reveals cancer stem cell heterogeneity in hepatocellular carcinoma," *Hepatology,* vol. 68, pp. 127-140, Jul 2018.

[32] P. Z. Hu, W; Xin, H; Deng, G, "Single Cell Isolation and Analysis," *Front Cell Dev Biol,* p. 116, 2016.

[33] M. Islam, H. Brink, S. Blanche, C. DiPrete, T. Bongiorno, N. Stone, *et al.*, "Microfluidic Sorting of Cells by Viability Based on Differences in Cell Stiffness," *Scientific Reports,* vol. 7, May 17 2017.

[34] H. Yun, K. Kim, and W. G. Lee, "Cell manipulation in microfluidics," *Biofabrication,* vol. 5, Jun 2013.

[35] J. Jeong, Y. Lee, Y. Yoo, and M. K. Lee, "Specific capture, recovery and culture of cancer cells using oriented antibody-modified polystyrene chips coated with agarose film," *Colloids and Surfaces B-Biointerfaces,* vol. 162, pp. 306-315, Feb 1 2018.

[36] F. Tian, L. L. Cai, J. Q. Chang, S. S. Li, C. Liu, T. J. Li, *et al.*, "Label-free isolation of rare tumor cells from untreated whole blood by interfacial viscoelastic microfluidics," *Lab on a Chip,* vol. 18, pp. 3436-3445, Nov 21 2018.

[37] C. M. Lin, Y. S. Lai, H. P. Liu, C. Y. Chen, and A. M. Wo, "Trapping of Bioparticles via Microvortices in a Microfluidic Device for Bioassay Applications," *Analytical Chemistry,* vol. 80, pp. 8937-8945, Dec 1 2008.

[38] H. Sun, T. Olsen, J. Zhu, J. G. Tao, B. Ponnaiya, S. A. Amundson, *et al.*, "A bead-based microfluidic approach to integrated single-cell gene expression analysis by quantitative RT-PCR," *Rsc Advances,* vol. 5, pp. 4886-4893, 2015.

[39] A. K. White, M. VanInsberghe, O. I. Petriv, M. Hamidi, D. Sikorski, M. A. Marra, *et al.*, "High-throughput microfluidic single-cell RT-qPCR," *Proceedings of the National Academy of Sciences of the United States of America,* vol. 108, pp. 13999-14004, Aug 23 2011.

[40] J. Zhu, T. Nguyen, R. J. Pei, M. Stojanovic, and Q. Lin, "Specific capture and temperature-mediated release of cells in an aptamer-based microfluidic device," *Lab on a Chip,* vol. 12, pp. 3504-3513, 2012.

[41] J. Zhu, J. Y. Shang, Y. Jia, R. J. Pei, M. Stojanovic, and Q. Lin, "Spatially selective release of aptamer-captured cells by temperature mediation," *Iet Nanobiotechnology,* vol. 8, pp. 2-9, Mar 2014.

[42] M. Souli, A. Ouahsine, and L. Lewin, "ALE formulation for fluid-structure interaction problems," *Computer Methods in Applied Mechanics and Engineering,* vol. 190, pp. 659-675, 2000.

[43] S. Basting, A. Quaini, S. Canic, and R. Glowinski, "Extended ALE Method for fluid-

structure interaction problems with large structural displacements," *Journal of Computational Physics,* vol. 331, pp. 312-336, Feb 15 2017.

[44] W. C. Chuang, H. L. Lee, P. Z. Chang, and Y. C. Hu, "Review on the Modeling of Electrostatic MEMS," *Sensors,* vol. 10, pp. 6149-6171, Jun 2010.

[45] X. Huang, S. Q. Li, J. Schultz, Q. Wang, and Q. Lin, "A Capacitive MEMS Viscometric Sensor for Affinity Detection of Glucose," *Journal of Microelectromechanical Systems,* vol. 18, pp. 1246-1254, Dec 2009.

[46] Y. J. Zhao, S. Q. Li, A. Davidson, B. Z. Yang, Q. Wang, and Q. Lin, "A MEMS viscometric sensor for continuous glucose monitoring," *Journal of Micromechanics and Microengineering,* vol. 17, pp. 2528-2537, Dec 2007.

[47] A. Nisar, N. AftuIpurkar, B. Mahaisavariya, and A. Tuantranont, "MEMS-based micropumps in drug delivery and biomedical applications," *Sensors and Actuators B-Chemical,* vol. 130, pp. 917-942, Mar 28 2008.

[48] H. D. Akaydin, N. Elvin, and Y. Andreopoulos, "Energy Harvesting from Highly Unsteady Fluid Flows using Piezoelectric Materials," *Journal of Intelligent Material Systems and Structures,* vol. 21, pp. 1263-1278, Sep 2010.

[49] A. K. Pandey and R. Pratap, "Effect of flexural modes on squeeze film damping in MEMS cantilever resonators," *Journal of Micromechanics and Microengineering,* vol. 17, pp. 2475-2484, Dec 2007.

[50] Y. G. Wang, W. H. Lin, X. M. Li, and Z. J. Feng, "Bending and vibration of an electrostatically actuated circular microplate in presence of Casimir force," *Applied Mathematical Modelling,* vol. 35, pp. 2348-2357, May 2011.

[51] V. C. Hayden and L. Y. Beaulieu, "Modeling Rectangular Cantilevers during Torsion and Deflection for Application to Frictional Force Microscopy," *Microscopy and Microanalysis,* vol. 15, pp. 259-264, Jun 2009.

[52] T. Manzaneque, V. Ruiz, J. Hernando-Garcia, A. Ababneh, H. Seidel, and J. L. Sanchez-Rojas, "Characterization and simulation of the first extensional mode of rectangular micro-plates in liquid media," *Applied Physics Letters,* vol. 101, Oct 8 2012.

[53] H. H. Hu, N. A. Patankar, and M. Y. Zhu, "Direct numerical simulations of fluid-solid systems using the arbitrary Lagrangian-Eulerian technique," *Journal of Computational Physics,* vol. 169, pp. 427-462, May 20 2001.

[54] R. van Loon, P. D. Anderson, F. N. van De Vosse, and S. J. Sherwin, "Comparison of various fluid-structure interaction methods for deformable bodies," *Computers & Structures,* vol. 85, pp. 833-843, Jun 2007.

[55] J. E. Sader, "Frequency response of cantilever beams immersed in viscous fluids with applications to the atomic force microscope," *Journal of Applied Physics,* vol. 84, pp. 64-76, Jul 1 1998.

[56] D. Abdollahi, S. Ahdiaghdam, K. Ivaz, and R. Shabani, "A theoretical study for the vibration of a cantilever microbeam as a free boundary problem," *Applied Mathematical Modelling,* vol. 40, pp. 1836-1849, Feb 1 2016.

[57] R. S. Lenk, *Polymer Rheology*: Applied Science Publishers, 1978.

[58] B. J. Hamrock, S. R. Schmid, and B. O. Jacobson, *Fundamentals of Fluid Film Lubrication*: Taylor & Francis, 2004.

[59] T. A. Harder, Y. Tze-Jung, H. Qing, S. Chi-Yuan, and T. Yu-Chong, "Residual stress in thin-film parylene-c," in *Technical Digest. MEMS 2002 IEEE International Conference. Fifteenth IEEE International Conference on Micro Electro Mechanical Systems (Cat. No.02CH37266)*, 2002, pp. 435-438.

[60] Q. Zhang, W. Z. Ruan, H. Wang, Y. Z. Zhou, Z. Y. Wang, and L. T. Liu, "A self-bended piezoresistive microcantilever flow sensor for low flow rate measurement," *Sensors and Actuators a-Physical,* vol. 158, pp. 273-279, Mar 2010.

[61] H. F. Ji, K. M. Hansen, Z. Hu, and T. Thundat, "Detection of pH variation using modified microcantilever sensors," *Sensors and Actuators B-Chemical,* vol. 72, pp. 233-238, Feb 10 2001.

[62] G. Shekhawat, S. H. Tark, and V. P. Dravid, "MOSFET-embedded microcantilevers for measuring deflection in biomolecular sensors," *Science,* vol. 311, pp. 1592-1595, Mar 17 2006.

[63] A. Alodhayb, S. M. S. Rahman, S. Rahman, P. E. Georghiou, and L. Y. Beaulieu, "A 16-microcantilever array sensing system for the rapid and simultaneous detection of analyte," *Sensors and Actuators B-Chemical,* vol. 237, pp. 459-469, Dec 2016.

[64] J. D. Adams, B. W. Erickson, J. Grossenbacher, J. Brugger, A. Nievergelt, and G. E. Fantner, "Harnessing the damping properties of materials for high-speed atomic force microscopy," *Nature Nanotechnology,* vol. 11, pp. 147-151, Feb 2016.

[65] L. D. Landau, E. M. Lifshitz, and J. B. Sykes, *Theory of Elasticity*: Pergamon Press, 1989.

[66] C. P. Green and J. E. Sader, "Torsional frequency response of cantilever beams immersed in viscous fluids with applications to the atomic force microscope," *Journal of Applied Physics,* vol. 92, pp. 6262-6274, Nov 15 2002.

[67] C. A. Van Eysden and J. E. Sader, "Resonant frequencies of a rectangular cantilever beam immersed in a fluid," *Journal of Applied Physics,* vol. 100, Dec 1 2006.

[68] M. R. Paul and M. C. Cross, "Stochastic dynamics of nanoscale mechanical oscillators immersed in a viscous fluid," *Physical Review Letters,* vol. 92, Jun 11 2004.

[69] C. P. Green and J. E. Sader, "Small amplitude oscillations of a thin beam immersed in a viscous fluid near a solid surface," *Physics of Fluids,* vol. 17, Jul 2005.

[70] Y. Zhang, Q. Ren, and Y. P. Zhao, "Modelling analysis of surface stress on a rectangular cantilever beam," *Journal of Physics D-Applied Physics,* vol. 37, pp. 2140-2145, Aug 7 2004.

[71] S. Q. Li, E. N. Davis, J. Anderson, Q. Lin, and Q. Wang, "Development of Boronic Acid Grafted Random Copolymer Sensing Fluid for Continuous Glucose Monitoring," *Biomacromolecules,* vol. 10, pp. 113-118, Jan 2009.

[72] F. Padovani, J. Duffy, and M. Hegner, "Microrheological Coagulation Assay Exploiting Micromechanical Resonators," *Analytical Chemistry,* vol. 89, pp. 751-758, Jan 3 2017.

[73] J. Dorignac, A. Kalinowski, S. Erramilli, and P. Mohanty, "Dynamical response of nanomechanical oscillators in immiscible viscous fluid for in vitro biomolecular recognition," *Physical Review Letters,* vol. 96, May 12 2006.

[74] J. W. Ndieyira, N. Kappeler, S. Logan, M. A. Cooper, C. Abell, R. A. McKendry, *et al.*, "Surface-stress sensors for rapid and ultrasensitive detection of active free drugs in human serum," *Nature Nanotechnology,* vol. 9, pp. 225-232, Mar 2014.

[75] A. W. McFarland, M. A. Poggi, M. J. Doyle, L. A. Bottomley, and J. S. Colton, "Influence of surface stress on the resonance behavior of microcantilevers," *Applied Physics Letters,* vol. 87, Aug 1 2005.

[76] H. J. Butt and M. Jaschke, "Calculation of Thermal Noise in Atomic-Force Microscopy," *Nanotechnology,* vol. 6, pp. 1-7, Jan 1995.

[77] A. Jana, A. Raman, B. Dhayal, S. L. Tripp, and R. G. Reifenberger, "Microcantilever mechanics in flowing viscous fluids," *Applied Physics Letters,* vol. 90, Mar 12 2007.

[78] F. Ricci, D. Moscone, C. S. Tuta, G. Palleschi, A. Amine, A. Poscia, *et al.*, "Novel planar glucose biosensors for continuous monitoring use," *Biosensors & Bioelectronics,* vol. 20, pp. 1993-2000, Apr 15 2005.

[79] H. Suzuki, T. Tokuda, T. Miyagishi, H. Yoshida, and N. Honda, "A disposable on-line microsystem for continuous sampling and monitoring of glucose," *Sensors and Actuators B-Chemical,* vol. 97, pp. 90-97, Jan 1 2004.

[80] H. Shibata, Y. J. Heo, T. Okitsu, Y. Matsunaga, T. Kawanishi, and S. Takeuchi, "Injectable hydrogel microbeads for fluorescence-based in vivo continuous glucose monitoring," *Proceedings of the National Academy of Sciences of the United States of America,* vol. 107, pp. 17894-17898, Oct 19 2010.

[81] J. Siegrist, T. Kazarian, C. Ensor, S. Joel, M. Madou, P. Wang, *et al.*, "Continuous glucose sensor using novel genetically engineered binding polypeptides towards in vivo applications," *Sensors and Actuators B-Chemical,* vol. 149, pp. 51-58, Aug 6 2010.

[82] R. A. Siegel, Y. D. Gu, M. Lei, A. Baldi, E. E. Nuxoll, and B. Ziaie, "Hard and soft micro- and nanofabrication: An integrated approach to hydrogel-based biosensing and drug delivery," *Journal of Controlled Release,* vol. 141, pp. 303-313, Feb 15 2010.

[83] M. Lei, A. Baldi, E. Nuxoll, R. A. Siegel, and B. Ziaie, "A hydrogel-based implantable micromachined transponder for wireless glucose measurement," *Diabetes Technology & Therapeutics,* vol. 8, pp. 112-122, Feb 2006.

[84] Y. J. Heo, H. Shibata, T. Okitsu, T. Kawanishi, and S. Takeuchi, "Long-term in vivo glucose monitoring using fluorescent hydrogel fibers," *Proceedings of the National Academy of Sciences of the United States of America,* vol. 108, pp. 13399-13403, Aug 16 2011.

[85] J. C. Pickup, F. Hussain, N. D. Evans, O. J. Rolinski, and D. J. S. Birch, "Fluorescence-based glucose sensors," *Biosensors & Bioelectronics,* vol. 20, pp. 2555-2565, Jun 15 2005.

[86] F. H. Arnold, W. G. Zheng, and A. S. Michaels, "A membrane-moderated, conductimetric sensor for the detection and measurement of specific organic solutes in aqueous solutions," *Journal of Membrane Science,* vol. 167, pp. 227-239, Mar 30 2000.

[87] Z. W. Zou, J. H. Kai, M. J. Rust, J. Han, and C. H. Ahn, "Functionalized nano interdigitated electrodes arrays on polymer with integrated microfluidics for direct bio-affinity sensing

using impedimetric measurement," *Sensors and Actuators a-Physical,* vol. 136, pp. 518-526, May 16 2007.

[88] P. Kara, A. de la Escosura-Muniz, M. Maltez-da Costa, M. Guix, M. Ozsoz, and A. Merkoci, "Aptamers based electrochemical biosensor for protein detection using carbon nanotubes platforms," *Biosensors & Bioelectronics,* vol. 26, pp. 1715-1718, Dec 15 2010.

[89] J. Kafka, O. Panke, B. Abendroth, and F. Lisdat, "A label-free DNA sensor based on impedance spectroscopy," *Electrochimica Acta,* vol. 53, pp. 7467-7474, Oct 30 2008.

[90] J. Baur, C. Gondran, M. Holzinger, E. Defrancq, H. Perrot, and S. Cosnier, "Label-Free Femtomolar Detection of Target DNA by Impedimetric DNA Sensor Based on Poly(pyrrole-nitrilotriacetic acid) Film," *Analytical Chemistry,* vol. 82, pp. 1066-1072, Feb 1 2010.

[91] M. Labib, A. S. Zamay, O. S. Koloyskaya, I. T. Reshetneva, G. S. Zamay, R. J. Kibbee, *et al.*, "Aptamer-Based Viability Impedimetric Sensor for Bacteria," *Analytical Chemistry,* vol. 84, pp. 8966-8969, Nov 6 2012.

[92] P. Qi, Y. Wan, and D. Zhang, "Impedimetric biosensor based on cell-mediated bioimprinted films for bacterial detection," *Biosensors & Bioelectronics,* vol. 39, pp. 282-288, Jan 15 2013.

[93] X. Huang, S. Li, J. S. Schultz, Q. Wang, and Q. Lin, "A dielectric affinity microbiosensor," *Applied Physics Letters,* vol. 96, p. 033701, 2010.

[94] X. Huang, S. Q. Li, E. Davis, D. C. Li, Q. Wang, and Q. Lin, "A MEMS Dielectric Affinity Glucose Biosensor," *Journal of Microelectromechanical Systems,* vol. 23, pp. 14-20, Feb 2014.

[95] S. Kuenzi, E. Meurville, and P. Ryser, "Automated characterization of dextran/concanavalin A mixtures—a study of sensitivity and temperature dependence at low viscosity as basis for an implantable glucose sensor," *Sensors and Actuators B: Chemical,* vol. 146, pp. 1-7, 2010.

[96] H. J. Woo, S. R. Majid, and A. K. Arof, "Dielectric properties and morphology of polymer electrolyte based on poly(epsilon-caprolactone) and ammonium thiocyanate," *Materials Chemistry and Physics,* vol. 134, pp. 755-761, Jun 15 2012.

[97] F. Kremer and A. Schönhals, "Broadband Dielectric Spectroscopy," *New York, NY, USA: Springer,* 2003.

[98] K. R. Foster and H. P. Schwan, "Dielectric-Properties of Tissues and Biological-Materials - a Critical-Review," *Critical Reviews in Biomedical Engineering,* vol. 17, pp. 25-104, 1989.

[99] Y. Feldman, E. Polygalov, I. Ermolina, Y. Polevaya, and B. Tsentsiper, "Electrode polarization correction in time domain dielectric spectroscopy," *Measurement Science & Technology,* vol. 12, pp. 1355-1364, Aug 2001.

[100] C. W. de Silva, *Sensors and Actuators: Control System Instrumentation*: Taylor & Francis, 2007.

[101] S. J. Updike, M. C. Shults, B. J. Gilligan, and R. K. Rhodes, "A subcutaneous glucose sensor with improved longevity, dynamic range, and stability of calibration," *Diabetes Care,* vol. 23, pp. 208-214, Feb 2000.

[102] I. DexCom, "DexCom™ G4 PLATINUM."

[103] M. MiniMed, "MiniMed Paradigm® REAL-time insulin pump and continuous glucose monitoring system."

[104] A. D. Care, "FreeStyle Navigator® continuous glucose monitoring system."

[105] M. Mesch, C. J. Zhang, P. V. Braun, and H. Giessen, "Functionalized Hydrogel on Plasmonic Nanoantennas for Noninvasive Glucose Sensing," *Acs Photonics,* vol. 2, pp. 475-480, Apr 2015.

[106] C. J. Zhang, M. D. Losego, and P. V. Braun, "Hydrogel-Based Glucose Sensors: Effects of Phenylboronic Acid Chemical Structure on Response," *Chemistry of Materials,* vol. 25, pp. 3239-3250, Aug 13 2013.

[107] S. Li, X. Huang, E. N. Davis, Q. Lin, and Q. Wang, "Development of novel glucose sensing fluids with potential application to microelectromechanical systems-based continuous glucose monitoring," *Journal of diabetes science and technology,* vol. 2, pp. 1066-1074, 2008.

[108] S. Li, E. N. Davis, J. Anderson, Q. Lin, and Q. Wang, "Development of boronic acid grafted random copolymer sensing fluid for continuous glucose monitoring," *Biomacromolecules,* vol. 10, pp. 113-118, 2008.

[109] X. Huang, S. Li, J. S. Schultz, Q. Wang, and Q. Lin, "A MEMS affinity glucose sensor using a biocompatible glucose-responsive polymer," *Sensors and Actuators B: Chemical,*

vol. 140, pp. 603-609, 2009.

[110] X. Huang, S. Li, J. Schultz, Q. Wang, and Q. Lin, "A capacitive MEMS viscometric sensor for affinity detection of glucose," *Microelectromechanical Systems, Journal of*, vol. 18, pp. 1246-1254, 2009.

[111] A. P. Patel, I. Tirosh, J. J. Trombetta, A. K. Shalek, S. M. Gillespie, H. Wakimoto, *et al.*, "Single-cell RNA-seq highlights intratumoral heterogeneity in primary glioblastoma," *Science*, vol. 344, pp. 1396-1401, Jun 20 2014.

[112] K. C. Schuster, E. Urlaub, and J. R. Gapes, "Single-cell analysis of bacteria by Raman microscopy: spectral information on the chemical composition of cells and on the heterogeneity in a culture," *Journal of Microbiological Methods*, vol. 42, pp. 29-38, Sep 2000.

[113] D. A. Lawson, N. R. Bhakta, K. Kessenbrock, K. D. Prummel, Y. Yu, K. Takai, *et al.*, "Single-cell analysis reveals a stem-cell program in human metastatic breast cancer cells," *Nature*, vol. 526, pp. 131-+, Oct 1 2015.

[114] M. Janiszewska, L. Liu, V. Almendro, Y. Kuang, C. Paweletz, R. A. Sakr, *et al.*, "In situ single-cell analysis identifies heterogeneity for PIK3CA mutation and HER2 amplification in HER2-positive breast cancer," *Nature Genetics*, vol. 47, pp. 1212-+, Oct 2015.

[115] X. J. Qiu, A. Hill, J. Packer, D. J. Lin, Y. A. Ma, and C. Trapnell, "Single-cell mRNA quantification and differential analysis with Census," *Nature Methods*, vol. 14, pp. 309-+, Mar 2017.

[116] C. Trapnell, D. Cacchiarelli, J. Grimsby, P. Pokharel, S. Q. Li, M. Morse, *et al.*, "The dynamics and regulators of cell fate decisions are revealed by pseudotemporal ordering of single cells," *Nature Biotechnology*, vol. 32, pp. 381-U251, Apr 2014.

[117] B. Ponnaiya, S. A. Amundson, S. A. Ghandhi, L. B. Smilenov, C. R. Geard, M. Buonanno, *et al.*, "Single-cell responses to ionizing radiation," *Radiation and Environmental Biophysics*, vol. 52, pp. 523-530, Nov 2013.

[118] L. Li, M. Story, and R. J. Legerski, "Cellular responses to ionizing radiation damage," *International Journal of Radiation Oncology Biology Physics*, vol. 49, pp. 1157-1162, Mar 15 2001.

[119] J. B. Little, "Cellular radiation effects and the bystander response," *Mutation Research-Fundamental and Molecular Mechanisms of Mutagenesis*, vol. 597, pp. 113-118, May 11

2006.

[120] A. Jazayeri, A. Balestrini, E. Garner, J. E. Haber, and V. Costanzo, "Mre11-Rad50-Nbs1-dependent processing of DNA breaks generates oligonucleotides that stimulate ATM activity," *Embo Journal,* vol. 27, pp. 1953-1962, Jul 23 2008.

[121] E. Mladenov, B. Anachkova, and I. Tsaneva, "Sub-nuclear localization of Rad51 in response to DNA damage," *Genes to Cells,* vol. 11, pp. 513-524, May 2006.

[122] Z. Goldberg, C. W. Schwietert, B. Lehnert, R. Stern, and I. Nami, "Effects of low-dose ionizing radiation on gene expression in human skin biopsies," *International Journal of Radiation Oncology Biology Physics,* vol. 58, pp. 567-574, Feb 1 2004.

[123] V. G. Tusher, R. Tibshirani, and G. Chu, "Significance analysis of microarrays applied to the ionizing radiation response (vol 98, pg 5116, 2001)," *Proceedings of the National Academy of Sciences of the United States of America,* vol. 98, pp. 10515-10515, Aug 28 2001.

[124] L. H. Ding, M. Shingyoji, F. Q. Chen, J. J. Hwang, S. Burma, C. Lee, *et al.*, "Gene expression profiles of normal human fibroblasts after exposure to ionizing radiation: A comparative study of low and high doses," *Radiation Research,* vol. 164, pp. 17-26, Jul 2005.

[125] A. D. Patterson, H. Li, G. S. Eichler, K. W. Krausz, J. N. Weinstein, A. J. Formace, *et al.*, "UPLC-ESI-TOFMS-based metabolomics and gene expression dynamics inspector self-organizing metabolomic maps as tools for understanding the cellular response to ionizing radiation," *Analytical Chemistry,* vol. 80, pp. 665-674, Feb 1 2008.

[126] B. Ponnaiya, G. Jenkins-Baker, G. Randers-Pherson, and C. R. Geard, "Quantifying a bystander response following microbearn irradiation using single-cell RT-PCR analyses," *Experimental Hematology,* vol. 35, pp. 64-68, Apr 2007.

[127] N. Hamada, H. Matsumoto, T. Hara, and Y. Kobayashi, "Intercellular and intracellular signaling pathways mediating ionizing radiation-induced bystander effects," *Journal of Radiation Research,* vol. 48, pp. 87-95, Mar 2007.

[128] O. V. Belyakov, A. M. Malcolmson, M. Folkard, K. M. Prise, and B. D. Michael, "Direct evidence for a bystander effect of ionizing radiation in primary human fibroblasts," *British Journal of Cancer,* vol. 84, pp. 674-679, Mar 2 2001.

[129] E. I. Azzam, S. M. de Toledo, A. L. Harris, V. Ivanov, H. Zhou, S. A. Amundson, *et al.*,

"The Ionizing Radiation-Induced Bystander Effect: Evidence, Mechanism, and Significance," in *Pathobiology of Cancer Regimen-Related Toxicities*, S. T. Sonis and D. M. Keefe, Eds., ed New York, NY: Springer New York, 2013, pp. 35-61.

[130] S. A. Marino, "50 Years of the Radiological Research Accelerator Facility (RARAF)," *Radiation Research,* vol. 187, pp. 413-423, Apr 2017.

[131] N. M. Toriello, E. S. Douglas, N. Thaitrong, S. C. Hsiao, M. B. Francis, C. R. Bertozzi, *et al.*, "Integrated microfluidic bioprocessor for single-cell gene expression analysis," *Proceedings of the National Academy of Sciences of the United States of America*, vol. 105, pp. 20173-20178, Dec 23 2008.

[132] C. J. Hayes, C. M. Dowling, S. Dwane, M. E. McCumiskey, S. M. Tormey, B. A. Merrigan, *et al.*, "Extracellular matrix gene expression profiling using microfluidics for colorectal carcinoma stratification," *Biomicrofluidics,* vol. 10, Sep 2016.

[133] J. F. Zhong, Y. Chen, J. S. Marcus, A. Scherer, S. R. Quake, C. R. Taylor, *et al.*, "A microfluidic processor for gene expression profiling of single human embryonic stem cells," *Lab on a Chip,* vol. 8, pp. 68-74, 2008.

[134] D. Di Carlo, N. Aghdam, and L. P. Lee, "Single-cell enzyme concentrations, kinetics, and inhibition analysis using high-density hydrodynamic cell isolation arrays," *Analytical Chemistry,* vol. 78, pp. 4925-4930, Jul 15 2006.

[135] J. S. Marcus, W. F. Anderson, and S. R. Quake, "Microfluidic single-cell mRNA isolation and analysis," *Analytical Chemistry,* vol. 78, pp. 3084-3089, May 1 2006.

[136] Y. T. Kim, Y. Chen, J. Y. Choi, W. J. Kim, H. M. Dae, J. Jung, *et al.*, "Integrated microdevice of reverse transcription-polymerase chain reaction with colorimetric immunochromatographic detection for rapid gene expression analysis of influenza A H1N1 virus," *Biosensors & Bioelectronics,* vol. 33, pp. 88-94, Mar 15 2012.

[137] M. A. Unger, H. P. Chou, T. Thorsen, A. Scherer, and S. R. Quake, "Monolithic microfabricated valves and pumps by multilayer soft lithography," *Science*, vol. 288, pp. 113-116, Apr 7 2000.

[138] T. Schneider, J. Kreutz, and D. T. Chiu, "The Potential Impact of Droplet Microfluidics in Biology," *Analytical Chemistry,* vol. 85, pp. 3476-3482, Apr 2 2013.

[139] H. Sun, T. Olsen, J. Zhu, J. G. Tao, B. Ponnaiya, S. A. Amundson, *et al.*, "A microfluidic approach to parallelized transcriptional profiling of single cells," *Microfluidics and*

Nanofluidics, vol. 19, pp. 1429-1440, Dec 2015.

[140] M. Mehling and S. Tay, "Microfluidic cell culture," *Current Opinion in Biotechnology,* vol. 25, pp. 95-102, Feb 2014.

[141] A. Polini, E. Mele, A. G. Sciancalepore, S. Girardo, A. Biasco, A. Camposeo, *et al.*, "Reduction of water evaporation in polymerase chain reaction microfluidic devices based on oscillating-flow," *Biomicrofluidics,* vol. 4, Sep 2010.

[142] S. A. Amundson, "Functional genomics in radiation biology: a gateway to cellular systems-level studies," *Radiation and Environmental Biophysics,* vol. 47, pp. 25-31, Feb 2008.

[143] N. Sandor, B. Schilling-Toth, E. Kis, A. Benedek, K. Lumniczky, G. Safrany, *et al.*, "Growth Differentiation Factor-15 (GDF-15) is a potential marker of radiation response and radiation sensitivity," *Mutation Research-Genetic Toxicology and Environmental Mutagenesis,* vol. 793, pp. 142-149, Nov 2015.

[144] S. A. Ghandhi, B. Yaghoubian, and S. A. Amundson, "Global gene expression analyses of bystander and alpha particle irradiated normal human lung fibroblasts: Synchronous and differential responses," *Bmc Medical Genomics,* vol. 1, Dec 24 2008.

[145] J. F. Ziegler, M. D. Ziegler, and J. P. Biersack, "SRIM – The stopping and range of ions in matter (2010)," *Nuclear Instruments and Methods in Physics Research Section B: Beam Interactions with Materials and Atoms,* vol. 268, pp. 1818-1823, 2010/06/01/ 2010.

[146] G. M. Whitesides, E. Ostuni, S. Takayama, X. Y. Jiang, and D. E. Ingber, "Soft lithography in biology and biochemistry," *Annual Review of Biomedical Engineering,* vol. 3, pp. 335-373, 2001.

[147] S. K. Arya, K. C. Lee, D. Bin Dah'alan, Daniel, and A. R. A. Rahman, "Breast tumor cell detection at single cell resolution using an electrochemical impedance technique," *Lab on a Chip,* vol. 12, pp. 2362-2368, 2012.

[148] J. F. Chen, Y. Z. Zhu, Y. T. Lu, E. Hodara, S. Hou, V. G. Agopian, *et al.*, "Clinical Applications of NanoVelcro Rare-Cell Assays for Detection and Characterization of Circulating Tumor Cells," *Theranostics,* vol. 6, pp. 1425-1439, 2016.

[149] S. M. Shaffer, M. C. Dunagin, S. R. Torborg, E. A. Torre, B. Emert, C. Krepler, *et al.*, "Rare cell variability and drug- induced reprogramming as a mode of cancer drug resistance," *Nature,* vol. 546, pp. 431-+, Jun 15 2017.

[150] C. W. Shields, C. D. Reyes, and G. P. Lopez, "Microfluidic cell sorting: a review of the advances in the separation of cells from debulking to rare cell isolation," *Lab on a Chip,* vol. 15, pp. 1230-1249, 2015.

[151] S. A. Ghandhi, L. Ming, V. N. Ivanov, T. K. Hei, and S. A. Amundson, "Regulation of early signaling and gene expression in the alpha-particle and bystander response of IMR-90 human fibroblasts," *Bmc Medical Genomics,* vol. 3, Jul 29 2010.

[152] L. Li, Y. Yan, H. X. Xu, T. Qu, and B. X. Wang, "Selection of reference genes for gene expression studies in ultraviolet B-irradiated human skin fibroblasts using quantitative real-time PCR," *Bmc Molecular Biology,* vol. 12, Feb 17 2011.

[153] S. A. Ghandhi, A. Sinha, M. Markatou, and S. A. Amundson, "Time-series clustering of gene expression in irradiated and bystander fibroblasts: an application of FBPA clustering," *Bmc Genomics,* vol. 12, Jan 4 2011.

[154] V. Chauhan and M. Howland, "Gene expression responses in human lung fibroblasts exposed to alpha particle radiation," *Toxicology in Vitro,* vol. 28, pp. 1222-1229, Oct 2014.

[155] E. I. Azzam, S. M. de Toledo, and J. B. Little, "Direct evidence for the participation of gap junction-mediated intercellular communication in the transmission of damage signals from alpha-particle irradiated to nonirradiated cells," *Proceedings of the National Academy of Sciences of the United States of America,* vol. 98, pp. 473-478, Jan 16 2001.

[156] G. O. Edwards, S. W. Botchway, G. Hirst, C. W. Wharton, J. K. Chipman, and R. A. Meldrum, "Gap junction communication dynamics and bystander effects from ultrasoft X-rays," *British Journal of Cancer,* vol. 90, pp. 1450-1456, Apr 5 2004.

[157] C. Mothersill and C. B. Seymour, "Cell-cell contact during gamma irradiation is not required to induce a bystander effect in normal human keratinocytes: Evidence for release during irradiation of a signal controlling survival into the medium," *Radiation Research,* vol. 149, pp. 256-262, Mar 1998.

[158] R. S. Asur, R. A. Thomas, and J. D. Tucker, "Chemical induction of the bystander effect in normal human lymphoblastoid cells," *Mutation Research-Genetic Toxicology and Environmental Mutagenesis,* vol. 676, pp. 11-16, May 31 2009.

[159] M. Fischer, "Census and evaluation of p53 target genes," *Oncogene,* vol. 36, pp. 3943-3956, Jul 13 2017.

[160] J. A. Kelly, M. S. Lucia, and J. R. Lambert, "p53 controls prostate-derived

factor/macrophage inhibitory cytokine/NSAID-activated gene expression in response to cell density, DNA damage and hypoxia through diverse mechanisms," *Cancer Letters,* vol. 277, pp. 38-47, May 8 2009.

[161] J. Stewart-Ornstein and G. Lahav, "Dynamics of CDKN1A in Single Cells Defined by an Endogenous Fluorescent Tagging Toolkit," *Cell Reports,* vol. 14, pp. 1800-1811, Feb 23 2016.

[162] O. Cazzalini, A. I. Scovassi, M. Savio, L. A. Stivala, and E. Prosperi, "Multiple roles of the cell cycle inhibitor p21(CDKN1A) in the DNA damage response," *Mutation Research-Reviews in Mutation Research,* vol. 704, pp. 12-20, Apr-Jun 2010.

[163] J. A. Han, J. I. Kim, P. P. Ongusaha, D. H. Hwang, L. R. Ballou, A. Mahale, *et al.*, "p53-mediated induction of Cox-2 counteracts p53-or genotoxic stress-induced apoptosis," *Embo Journal,* vol. 21, pp. 5635-5644, Nov 1 2002.

[164] E. M. Choi, J. I. Heo, J. Y. Oh, Y. M. Kim, K. S. Ha, J. I. Kim, *et al.*, "COX-2 regulates p53 activity and inhibits DNA damage-induced apoptosis," *Biochemical and Biophysical Research Communications,* vol. 328, pp. 1107-1112, Mar 25 2005.

[165] G. A. Webster and N. D. Perkins, "Transcriptional cross talk between NF-kappa B and p53," *Molecular and Cellular Biology,* vol. 19, pp. 3485-3495, May 1999.

[166] P. A. Hall, D. Meek, and D. P. Lane, "p53 - Integrating the complexity," *Journal of Pathology,* vol. 180, pp. 1-5, Sep 1996.

[167] A. J. Levine, "p53, the cellular gatekeeper for growth and division," *Cell,* vol. 88, pp. 323-331, Feb 7 1997.

[168] C. D. Brumbaugh, H. J. Kim, M. Giovacchini, and N. Pourmand, "NanoStriDE: Normalization and Differential Expression Analysis of NanoString nCounter Data," *Bmc Bioinformatics,* vol. 12, Dec 16 2011.